institute of telecommunications

Dissertation

On the Occurrence of Two-Wave with Diffuse Power Fading in Millimeter Wave Communications

Erich Zöchmann

Vienna, March 13, 2019

Advisor: Univ. Prof. Markus Rupp
Institute of Telecommunications, TU Wien

“Pluralitas non est ponenda sine neccesitate.”

William of Ockham, 14th century

“Everything should be made as simple as possible, but not simpler.”

attributed to Albert Einstein, 20th century

Acknowledgements

First of all, I would like to thank Professor Markus Rupp, who has been an exemplary advisor to me. By giving me the necessary freedom, he allowed me to develop and to pursue my own ideas. I would also like to express my gratitude to the Christian Doppler Society, TU Brno, A1 Telekom Austria, and TU Wien for their financial support. Special thanks goes to my mentors Christoph Mecklenbräuker, and Sebastian Caban as well as to my colleagues Martin Lerch, Stefan Pratschner, Ronald Nissel, Herbert Groll, and Daniel Schützenhöfer, who shared the lab, their ideas, their workforce, and their lunchtime with me. Moreover, I would like to thank my friends for the nice hours away from research. Finally, I would like to express my deepest appreciation to Claudia, the love of my life. You spent years by my side and have always supported me during the times when there was no one to answer my queries.

Abstract

Mobile communications has become so successful today that conventional radio technologies, in traditional frequency bands below 6 GHz, are soon reaching their limits. To be able to develop massively deployed, ubiquitous, data-hungry, mobile applications, this study explores the use of higher frequency bands, or so-called millimeter waves in mobile communications. These radio bands above 30 GHz are mostly unoccupied and have dozens of gigahertz of bandwidth available. Moreover, advances in electronics have now made it possible to utilize these bands cost effectively.

This thesis studied the millimeter wave wireless channel through conducting the following experiments: (1) two indoor millimeter wave measurement campaigns with directive horn antennas on both link ends, (2) an outdoor vehicular millimeter wave measurement campaign employing a horn antenna and an omni directional antenna, and (3) a railway communications ray-tracing study with directive antennas on both sides.

In all the cases, the data obtained show that the millimeter wave wireless channel has very limited multipath propagation. The main reason for the absence of a rich multipath propagation is because the millimeter wave wireless channel requires high-gain directive antennas that compensate for the path loss. These directive antennas act as spatial filters, thereby effectively reducing the number of significant multipath components.

All the cases presented in this thesis are characterized by one or two dominant multipath components. Small-scale fading is hence adequately modeled with a model named two-wave with diffuse power (TWDP). This TWDP model captures the effect of interference of two non-fluctuating radio signals and of many smaller so-called diffuse signals.

A delay-Doppler analysis is also performed in this research based on the data obtained from the vehicular measurement campaign. The analysis reveals that the high maximum Doppler shift is not reflected in the Doppler spread values. Again, the effects of the Doppler shift in this setup are suppressed due to spatial filtering.

Lastly, this thesis briefly addresses the modeling of the TWDP model parameters for a simplified railway communications scenario, and demonstrates the implications of TWDP fading through numerical simulations.

Kurzfassung

Mobilkommunikation ist heute so erfolgreich, dass herkömmliche Funktechnologien in traditionellen Frequenzbändern bis 6 GHz bald an ihre Grenzen stoßen. Um die Vision der überall verfügbaren hohen Bandbreite zu realisieren, untersucht diese Studie die Verwendung höherer Frequenzbänder, der sogenannten Millimeterwellen, in der Mobilkommunikation. Diese Frequenzbänder über 30 GHz sind meistens unbelegt und schon einzelne Bänder verfügen über weit mehr Bandbreite als alle bisher genutzen Bänder. Darüber hinaus haben Fortschritte in der Elektronik nun ermöglicht, diese Bänder kostengünstig zu nutzen.

In dieser Arbeit wurde der Millimeterwellen-Funkkanal mittels folgender Experimente untersucht: (1) zweier Messkampagnen mit direktionalen Hornantennen in einer statischen Büroumgebung, (2) einer Millimeterwellen-Fahrzeugkommunikationsmesskampagne mit einer Hornantenne und einer omnidirektionalen Antenne, sowie (3) einer Eisenbahnkommunikation-Raytracing-Studie mit Richtantennen auf beiden Seiten.

In allen Fällen zeigen die erhaltenen Daten, dass der Millimeterwellen-Funkkanal eine sehr begrenzte Mehrwegeausbreitung hat. Der Hauptgrund für das Fehlen von vielen Mehrwegen liegt darin, dass für Millimeterwellenkommunikation Antennen mit hohem Gewinn eingesetzt werden müssen, um den hohen Pfadverlust zu kompensieren. Diese Richtantennen wirken als räumliche Filter, wodurch die Anzahl signifikanter Mehrwegekomponenten wirksam reduziert wird.

Alle in dieser Arbeit vorgestellten Fälle sind durch einen oder zwei dominante Mehrwege gekennzeichnet. Daher kann der Funkkanal mittels eines Modells namens “two-wave with diffuse power” (TWDP) angemessen modelliert werden. Dieses TWDP-Modell erfasst die Interferenz von zwei nicht fluktuierenden Funksignalen und von vielen kleineren sogenannten diffusen Signalen.

Bei dieser Untersuchung wird auch eine Verzögerungs-Doppler-Analyse durchgeführt, die auf den Daten der Fahrzeugmesskampagne basiert. Die Analyse zeigt, dass sich die hohe maximale Dopplerverschiebung nicht in der Dopplerspreizung widerspiegelt. Die Auswirkungen der Dopplerverschiebung sind aufgrund der räumlichen Filterung beschränkt.

In dieser Arbeit wird kurz auf die Modellierung der TWDP-Modellparameter für ein vereinfachtes Szenario der Eisenbahnkommunikation eingegangen. Ebenso werden Auswirkungen des TWDP-Schwunds durch numerische Simulationen demonstriert.

Contents

1 Introduction **1**

2 Methodology: Two-Wave with Diffuse Power Fading and Measurement Setups **7**
2.1 Two-Wave with Diffuse Power Fading . . . 7
2.1.1 Data Preprocessing . . . 10
2.1.2 Parameter Estimation and Model Selection . . . 10
2.1.3 The Transition of TWDP Fading to Rician Fading . . . 11
2.1.4 A Closer Look on the Transition Border . . . 13
2.1.5 Validation of the Chosen Model . . . 14
2.2 Measurement Setups . . . 15
2.2.1 Scalar-Valued Wideband Measurements . . . 15
2.2.2 Vector-Valued Measurements . . . 16
2.2.3 Triggered Vector-Valued Measurements . . . 18

3 Indoor Measurement Campaigns **21**
3.1 Scalar-Valued Wideband Measurements . . . 21
3.2 Vector-Valued Spatial Measurements . . . 24
3.2.1 Receive Power and Fading Distributions . . . 25
3.2.2 Efficient Computation of the Spatial Correlation . . . 29
3.2.3 Time-Gated Fading Results . . . 32

4 Outdoor Vehicular Measurement Campaign **35**
4.1 Receive Power Fluctuation during Overtaking . . . 37
4.2 Small-Scale Fading of the LOS Tap during Overtaking . . . 39
4.2.1 Statistical Analysis Based on AIC . . . 41
4.2.2 A Simplified Model for the Parameter Evolution . . . 43
4.3 Delay-Doppler Dispersion Evaluated via the Local Scattering Function . . . 46

5 Simulation Studies **51**
5.1 Railway Communications Ray-Tracing Study . . . 51
5.1.1 Time-Domain Description of the Two-Ray Model . . . 52
5.1.2 Frequency-Domain Description of the Two-Ray Model . . . 52
5.1.3 Simplistic Modeling of Directive Antennas . . . 53
5.1.4 Two-Wave with Diffuse Power Model Parametrization . . . 55
5.2 Link-Level Performance Study . . . 57
5.2.1 Uncoded BER . . . 57
5.2.2 Coded BER . . . 57
5.2.3 Throughput . . . 58

6 Conclusions and Possible Future Directions **61**

1 Introduction

Since the advent of commercial mobile communications, the telecommunications industry has mainly focused only on a small fraction of the radio spectrum. The current mobile communications standard, 4G-LTE, specifies frequency bands between $460\,\text{MHz}$ (E-UTRA operating band 31) and $5.9\,\text{GHz}$ (E-UTRA operating band 47) [1]. This frequency range is considered as the "sweet spot", as wavelengths are short enough to allow compact antennas while still being long enough to avoid large diffraction and penetration losses [2].

Researchers of the next-generation mobile communications standard 5G aim to achieve massive throughput by exploring higher frequency bands, the so-called millimeter waves (mmWaves) [3]. These radio bands above $30\,\text{GHz}$ are mostly unoccupied and have dozens of gigahertz of bandwidth available. These frequencies are so abundant primarily due to their oxygen and water vapor absorption lines (see Fig. 1.1). An extra attenuation of approximately $15\,\text{dB}/\text{km}$ at $60\,\text{GHz}$, in addition to the path loss, leads to prohibitive power requirements, which consequently leads to an atmospheric opacity of almost 100%. Hence, neither radar nor astronomy is performed at most mmWave bands. This is not a limiting factor in indoor mmWave communications, in mobile communications with cell radii of less than $200\,\text{m}$, or in communication between vehicles. As a matter of fact, as early as 1895, the first wireless communication experiments at $60\,\text{GHz}$ had already been conducted by Jagadish Chandra Bose [2]. Today, advances in electronics have made it possible to utilize these bands cost effectively [4].

Accurate modeling of wireless propagation effects is a fundamental prerequisite for a proper communication system design. After the double-directional radio channel model had been introduced to the field [5], wireless propagation research ($< 6\,\text{GHz}$) started to model the wireless channel agnostic to the antennas used. More than a decade later, propagation research is now focused on the abovementioned mmWave bands in order to unlock the large bandwidths available in this regime [6–9]. At mmWaves, an omnidirectional antenna has a small effective antenna area, which results in a high path loss [10–14]. As such, researchers have proposed to apply highly directive antennas on both link ends to overcome this high path loss [15–18].

Most researchers aim to achieve high directivity by using antenna arrays [19–24] while a few researchers have used dielectric lenses [25–27]. However, when the link quality depends so much on the achieved beam-forming gain, antennas must again be considered as part of the wireless channel. The antenna then influences small-scale fading. Figure 1.2 shows how the degrees of freedom of the antennas are used to form a narrow beam. To achieve such beams, a common signal is applied to all antennas with different time delays [28]. In case of narrowband systems, the time delays are approximated by phase changes. However, this approximation leads to performance drops as the bandwidth increases [29].

Many researchers have already addressed the issue of static mmWave channels [30–48]. In 1996, [30] showed that mmWave channels exhibit sparsity in the time domain, whereas [32, 33] have analyzed the use of millimeter waves for mobile communications as early as 2001. Nevertheless, much of the early work on this topic has focused on indoor WLAN [31, 34, 35]. A renaissance on mmWave propagation

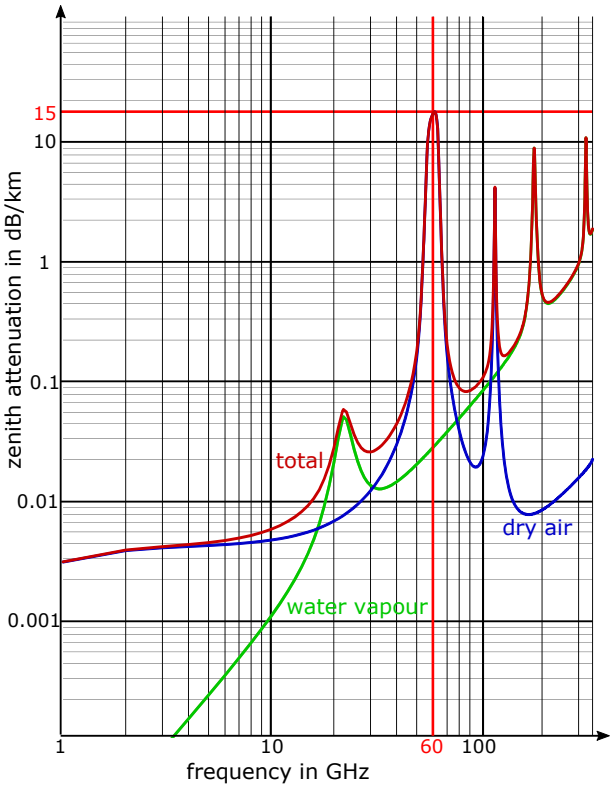

Figure 1.1: ***Total, dry, air and water-vapor zenith attenuation from sea level.*** Pressure $= 1013.25\,\text{hPa}$; Temperature $= 15°\,\text{C}$; Water Vapor Density $= 7.5\,\text{g/m}^3$. Reproduced from ITU-R P.676-11 recommendation with permission of ITU.

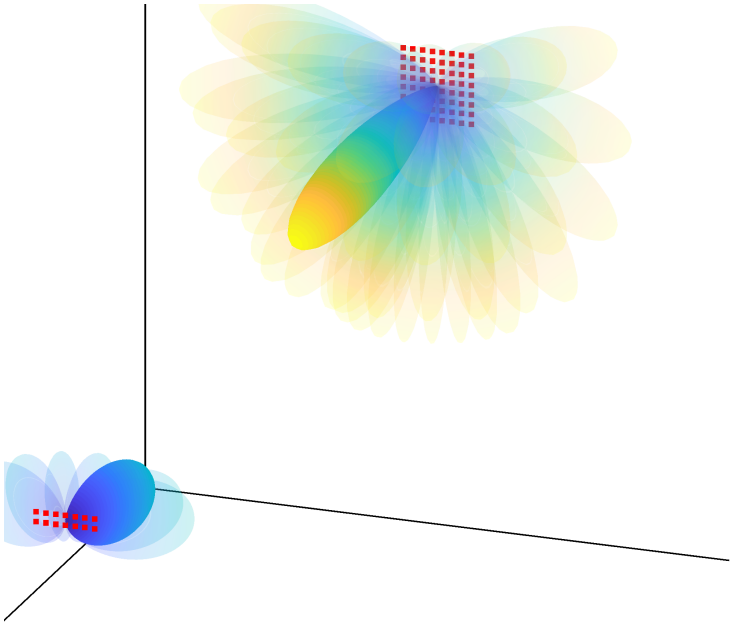

Figure 1.2: ***Directive communications through adaptive beamforming.*** mmWave arrays consisting of dozens of antennas are still very compact. A beam formed by the antenna array must be aligned to achieve sufficient link margin.

research has also appeared since 2013 [36, 49]; since then, research on mmWave propagation has been a very active field [37–48].

A research group from the TU Ilmenau carried out an indoor fading analysis. Likewise, this thesis has set up a similar experiment. The study of [50] investigated a simple wall scattering scenario and analyzed how fading scales with various antenna directivities and different bandwidths. Accordingly, increasing the directivity [50] as well as the bandwidth [50, 51], increases the Rician K-factor. Using the same measurement scenario, the study of [52] has shown that a sum-of-sinusoids fit achieves the lowest MSE for two sinusoids. In [52], they concluded that cluster fading behavior can be effectively modeled with two to six scattered multipath components (MPCs), without pointing towards two-wave with diffuse power (TWDP) fading.

A research group at New York University also analyzed mmWave fading using high-gain horn antennas on both link ends [53], and observed high Rician K-factors even at non-line-of-sight (NLOS). This effect is explained by spatial filtering of directive antennas, as they suppress many multipath components [50]. Outdoor measurements of the same group [54, 55], are then fitted with Rician fading.

Although the overwhelming majority of researchers favor Rician fading, Durgin argued against it in 2003 [56, p. 137]: "The use of directive antennas or arrays at a receiver, for example, amplifies several of the strongest multipath waves that arrive in one particular direction while attenuating the remaining waves. This effectively increases the ratio of specular to non-specular received power, turning a Rayleigh or Rician fading channel into a TWDP fading channel."

The TWDP fading that Durgin was referring to can characterize this spatial filtering effect by two non-fluctuating receive signals together with many smaller diffuse components. TWDP fading has already been successfully applied to describe 60 GHz near body shadowing [57]. An extension of the TWDP-fading model, the so-called fluctuating two-ray fading model, is described in [58–60]. This model brings in another degree of freedom and allows for common shadowing of both specular waves. The wireless channels in this present study are always unblocked; thus, this model is not considered here.

The theoretical work on TWDP fading is already at the advanced stages [58, 61–66]; however, experimental evidence on the field, especially at mmWaves, is still limited. For enclosed structures (with lower frequencies) such as aircraft cabins and buses, the applicability of the TWDP model has already been demonstrated by Frolik [67–71]. Likewise, the predicted TWDP fading has already been noted as early as 2003, albeit this has not yet been experimentally proven for mmWaves.

The research team of this study conducted two measurement campaigns [40, 72] to directionally analyze the receive power and small-scale fading parameters of mmWaves. *This thesis* shows that, through an information-theoretic criterion [73] and null hypothesis testing [74], the *TWDP hypothesis cannot be rejected for mmWave indoor communications*.

Aside from the indoor communication aspect, mmWaves are also foreseen for broadband connection of vehicles. The idea of automated cars represents a tremendous attraction to both the industry and the research community. Reliable mmWave communication systems that support vehicle-to-vehicle information exchange are anticipated to be among the key enablers for automated vehicles [75]. Due to the large available bandwidth of mmWave bands, even raw sensor data exchange between vehicles is possible [75]. Today, mmWave equipment is almost on board in any modern vehicles, as the first

mmWave automotive radars have already been commercialized 10 years ago [76]. Today, even joint vehicular communication and radar [77] systems are within reach.

Interestingly, mmWaves have already been candidates for vehicular communications for several decades now [78, 79]. mmWave train-to-infrastructure narrowband path loss has been measured in [78], whereas narrowband vehicle-to-vehicle (V2V) communication performance is studied in [79]. In [80] and [81], the focus was on inter-vehicle path loss results, whereas V2V channel measurements at 38 GHz and 60 GHz, using a channel sounder with 1 GHz bandwidth were conducted in [82]. The antennas in [82] were put into the bumpers, thereby the dominating MPCs were the line-of-sight (LOS) component, a road reflection, and a delayed component reflected on the guard rails. In [83], 73 GHz V2V large-scale fading and small-scale fading analysis were provided for approaching vehicles. The appearance of intra-vehicular Doppler spectra of vibrations while the vehicle operating have been shown in [84, 85]. The study of [86] investigated signal-to-noise ratio (SNR) fluctuations for 60 GHz transmissions with 5 MHz bandwidth in a vehicle-to-infrastructure scenario.

Meanwhile, time-varying receive power and time-varying small-scale fading for vehicular channels at 5.6 GHz were carefully addressed in [87]. However, mmWave vehicular communications has two main distinctive features as compared to sub-6-GHz vehicular communications: first, the use of directive antennas (at least on one link end) and second, the much higher maximum Doppler shift. This high maximum Doppler shift is directly proportional to the carrier frequency; thus, it is also viewed as a possible stumbling stone for vehicular mmWave communications. It was, however, shown theoretically in [88] and [89] that directional antennas, anticipated for mmWaves, act as spatial filters. Beamforming drastically decreases the Doppler effect, and hence the time-selectivity likewise decreases. Accordingly, *this is shown experimentally in this thesis*.

This study, contributes to the dynamic mmWave vehicle-to-vehicle channel research as it *analyzes the effect of an overtaking vehicle* on the mmWave V2V wideband (510 MHz) channel. It demonstrates that the size and the relative position of the overtaking vehicle greatly influence the large-scale and small-scale fading parameters. Again, the TWDP channel model is suitable for describing small-scale fading. Furthermore, Doppler dispersion is strongly suppressed by the transmit horn antenna. The data analyzed in this research consist of channel impulse responses while 30 different vehicles overtake. The statistical analysis in this study also differentiates the results between cars, sport utility vehicles, and trucks.

Another situation that is dominated by a limited multipath propagation occurs in mmWave railway communications. *This thesis* demonstrates that *railway communication scenarios employing directive antennas can be effectively modeled via a two-ray model*. The two-ray (ground reflection) model has been historically used to explain the multi-slope behavior of observed path loss. Accordingly, [90, 91] explained the multi-slope behavior of the observed path loss through a two-ray (ground reflection) model. The applicability of the two-ray model for the current dedicated short range communication standard around 5.9 GHz has been shown in [92–94]. Evidence for the two-ray model can also be found in [95], where the deviations from the two-ray model were explained by the road undulations. These road undulations (or in the train context, the heterogeneous ground and the hardly predictable reflection coefficient) motivated the author to transform the deterministic two-ray model into the statistical TWDP model. The study of [96] demonstrated on ray-tracing data that the two-ray model is a suitable deterministic small-scale fading model for line-of-sight (LOS) mmWave scenarios. Fading envelopes (depending on antenna alignments, geometry, and bandwidth) are derived in this study.

Next, it is argued that the two-ray model is a specific, deterministic variant of the TWDP model. The TWDP model is flexible enough to accommodate additionally smaller multipath components as the so-called diffuse components. Furthermore, through statistical modeling, uncertainties, for example, about reflection phases, road undulations, or path lengths, are automatically included. The derived quantities of the two-ray model will serve to parametrize the TWDP model.

The following paragraphs provide a short overview of the thesis structure. At the beginning of each chapter, the author's novel contributions and published papers (as first author) are explicitly stated.

Chapter 2 **Methodology: Two-Wave with Diffuse Power Fading and Measurement Setups:** This chapter introduces the TWDP model and its parameter estimation, and discusses the validation of measurement data. The chapter also details the smooth transistion from TWDP fading to Rician fading. The relatively small non-fluctuating wave can be absorbed into the diffuse components, and an acceptable fit with the simpler Rician fading model is then achieved. Accordingly, this makes the decision with regard to the occurrence of TWDP fading conservative. Lastly, Chapter 2 provides an overview of the built-up channel sounders, and shows the measurement setups together with brief discussions on their capabilities.

Chapter 3 **Indoor Measurement Campaigns:** This part describes the two measurement campaigns conducted in the laboratory and then discusses their outcomes. The first measurement campaign studies the TWDP fading of directional wireless communications in the frequency domain by using wideband scalar-valued data. TWDP fading is already observed; but due to the limited evaluation possibility with scalar measurement data, the setup is changed to a vectorial channel sounding concept with reduced measurement bandwidth. In the second measurement campaign, the mechanical beam steering is improved; with these improvements, TWDP fading is also analyzed in the space and time domain.

Chapter 4 **Outdoor Vehicular Measurement Campaign:** In this chapter, the dynamic millimeter-wave wireless channels are analyzed. The Doppler effect scales linearly with the carrier frequency, which is a challenge to channel sounding. Thus, the snapshot rate must be very high to capture properly the temporal evolution of the channel. The time-domain channel sounder, which is already used in the (second) vector-valued indoor measurement campaign, is capable of capturing the data sufficiently fast. This chapter then presents a scenario that emulates a communicating car platoon that is being overtaken. The scenario is carefully designed such that it allows different overtaking vehicle types to be measured repeatedly. Through statistical statements, this research is able to present a simplistic model of the small-scale fading during the overtaking process. The observed small-scale fading is again adequately modeled via TWDP fading. Additionally, the vehicular channel is studied within the delay-Doppler domain, which allows the author to make statements about the delay and the Doppler spread.

Chapter 5 **Simulation Studies:** In this chapter, the measurement data is no longer studied. Instead, data from an independent third source are used. The methodology presented in Chapter 2 is then applied to a ray-tracing data set. The published ray-tracing study dealt with railway communications, and beamforming was essentially limited to the elevation domain. As such, it is fairly easy to construct a model for this study that is solely based on the geometry and the antenna patterns. It is then presented in this chapter that the mobile channel can be described by using only a few propagation paths. The TWDP fit shows a good agreement with the observed ray-tracing data. Furthermore, this chapter provides link-level simulations that assesses the impact of TWDP fading on the link quality.

Chapter 6 **Conclusions and Possible Future Directions:** The summary of the results and their implications are presented in this chapter. As seen from the thesis title, this study seeks to point out the occasions when TWDP fading has been found; the results of which are thus discussed in this part of the thesis. Finally, this chapter provides the limitations of the research and discusses the recommended future actions. For example, the parameters of TWDP fading in this study are modeled very rudimentarily in some places. Thus, a large area of accurate channel modeling of TWDP fading is still open for discussion, which accordingly needs to be addressed in the future.

2 Methodology: Two-Wave with Diffuse Power Fading and Measurement Setups

The methodology introduced in Section 2.1 is first introduced in

- Erich Zöchmann et al. "Better than Rician: Modelling Millimetre Wave Channels as Two-Wave with Diffuse Power". In: *EURASIP Journal on Wireless Communications and Networking* 2019.1-17 (2019), p. 21

It is later slightly adapted for

- Erich Zöchmann et al. "Position-Specific Statistics of 60 GHz Vehicular Channels During Overtaking". In: *IEEE Access* 7 (2019), pp. 14216–14232
- Erich Zöchmann et al. "Parsimonious Channel Models for Millimeter Wave Railway Communications". In: *Proc. of IEEE Wireless Communications and Networking Conference*. 2019

The measurement setups discussed in Section 2.2 are first introduced in

- Erich Zöchmann et al. "Directional Evaluation of Receive Power, Rician K-factor and RMS Delay Spread Obtained from Power Measurements of 60 GHz Indoor Channels". In: *Proc. of IEEE-APS Topical Conf. on Antennas and Propagation in Wireless Communications (APWC)*. 2016
- Erich Zöchmann et al. "Associating Spatial Information to Directional Millimeter Wave Channel Measurements". In: *Proc. of IEEE 86th Vehicular Technology Conference (VTC-Fall)*. 2017
- Erich Zöchmann et al. "Measured Delay and Doppler Profiles of Overtaking Vehicles at 60 GHz". In: *Proc. of the 12th European Conference on Antennas and Propagation (EuCAP)*. 2018

2.1 Two-Wave with Diffuse Power Fading

TWDP fading captures the effect of interference of two non-fluctuating radio signals and many smaller so-called diffuse signals [101]. The TWDP distribution degenerates to the Rice distribution, if one of the two non-fluctuating radio signals vanishes. This condition is analogous to the well-known Rice degeneration to the Rayleigh distribution with decreasing K-factor. Hence, in a model selection framework, TWDP fading, Rician fading, and Rayleigh fading are nested hypotheses [73]. Accordingly, it is obvious that among these alternatives, TWDP fading would always allow the best possible fit of measurement data. Occam's razor [102] suggests that the hypothesis that makes the fewest possible assumptions should be selected among all the other competing hypothetical distributions (see the leading citations). Different distribution functions are often compared via a goodness-of-fit test [103]. Nevertheless, [104] argued that Akaike's information criterion (AIC) [73, 105–107] is a better suited method for choosing among fading distributions. Later on, AIC was also used in [108–112]. AIC can be seen as a form of Occam's razor as it penalizes the number of estimable parameters in the approximation model [73], and hence aims for parsimony.

An early form of TWDP was analyzed in [61], while the study of [101] introduced a random phase superposition formalism. Later, [64] achieved a major breakthrough, and found a description of TWDP fading that is the same as conditional Rician fading. For the benefit of the reader, this section briefly

repeats some important steps of [64]. The TWDP fading model in the complex-valued baseband is given as

$$r_{\text{complex}} = V_1 \mathrm{e}^{\mathrm{j}\phi_1} + V_2 \mathrm{e}^{\mathrm{j}\phi_2} + X + \mathrm{j}Y \; = V_1 \mathrm{e}^{\mathrm{j}\phi_1} + V_2 \mathrm{e}^{\mathrm{j}\phi_2} + V_3 \mathrm{e}^{\mathrm{j}\phi_3} = \sum_{i=1}^{3} V_i \mathrm{e}^{\mathrm{j}\phi_i}, \tag{2.1}$$

where $V_1 > 0$ and $V_2 \geq 0$ are the deterministic amplitudes of the non-fluctuating specular components. The phases ϕ_1, ϕ_2 and ϕ_3 are independent and uniformly distributed in $(0, 2\pi)$. The diffuse components are modeled via the law of large numbers as $X + \mathrm{j}Y$, where $X, Y \sim \mathcal{N}(0, \sigma^2)$. The amplitude V_3 is hence Rayleigh distributed. The formulation, as a superposition of three amplitudes, is very elegant but uncommon in the literature. The second moment of the envelope $r = |r_{\text{complex}}|$ of TWDP fading is given as

$$\mathbb{E}\{r^2\} = \Omega = V_1^2 + V_2^2 + 2\sigma^2 \; . \tag{2.2}$$

Expectation is denoted by $\mathbb{E}\{\cdot\}$. By enforcing

$$\Omega \equiv 1 \; , \tag{2.3}$$

all distributions are parametrized solely by the tuple (K, Δ), in which the K-factor is the power ratio of the specular components to the diffuse components

$$K = \frac{V_1^2 + V_2^2}{2\sigma^2} \; . \tag{2.4}$$

The parameter Δ describes the amplitude relationship among the specular (non-fluctuating) components

$$\Delta = \frac{2V_1V_2}{V_1^2 + V_2^2} \; . \tag{2.5}$$

The Δ-parameter is bounded between 0 and 1, and equals 1 if, and only if, both amplitudes are equal. By combining Eq. (2.2), (2.3), and (2.4) the second moment of the diffuse components equals to

$$\sigma^2 = \frac{1}{2\,(1+K)} \; . \tag{2.6}$$

Given the K and Δ parameter, the authors of [113] provide a formula for the amplitudes of both specular components, which is given as

$$V_{1,2} = \frac{1}{2}\sqrt{\frac{K}{K+1}}\left(\sqrt{1+\Delta} \pm \sqrt{1-\Delta}\right) . \tag{2.7}$$

The well-known Rice cumulative distribution function (CDF) is solely described by the Marcum Q-function $Q_1(\cdot,\cdot)$, and is expressed as

$$F_{\text{Rice}}(r; K) = 1 - Q_1\left(\sqrt{2K}, \frac{r}{\sigma}\right) \; . \tag{2.8}$$

It has been mentioned earlier that [64] found a description of the envelope of Eq. (2.1) as a conditional Rician distribution

$$F_{\text{TWDP}}(r; K, \Delta) = 1 - \frac{1}{2\pi}\int_0^{2\pi} Q_1\left(\sqrt{2K\,(1+\Delta\cos(\alpha))}, \frac{r}{\sigma}\right) \mathrm{d}\alpha \; , \tag{2.9}$$

where K of (2.8) is replaced by $K\left(1+\Delta\cos(\alpha)\right)$, and the auxiliary variable α is uniformily distributed in $(0, 2\pi)$. Fig. 2.1 shows a number of example distributions. Although it might sound tempting to have a second strong radio signal present, two waves can either superpose constructively or destructively,

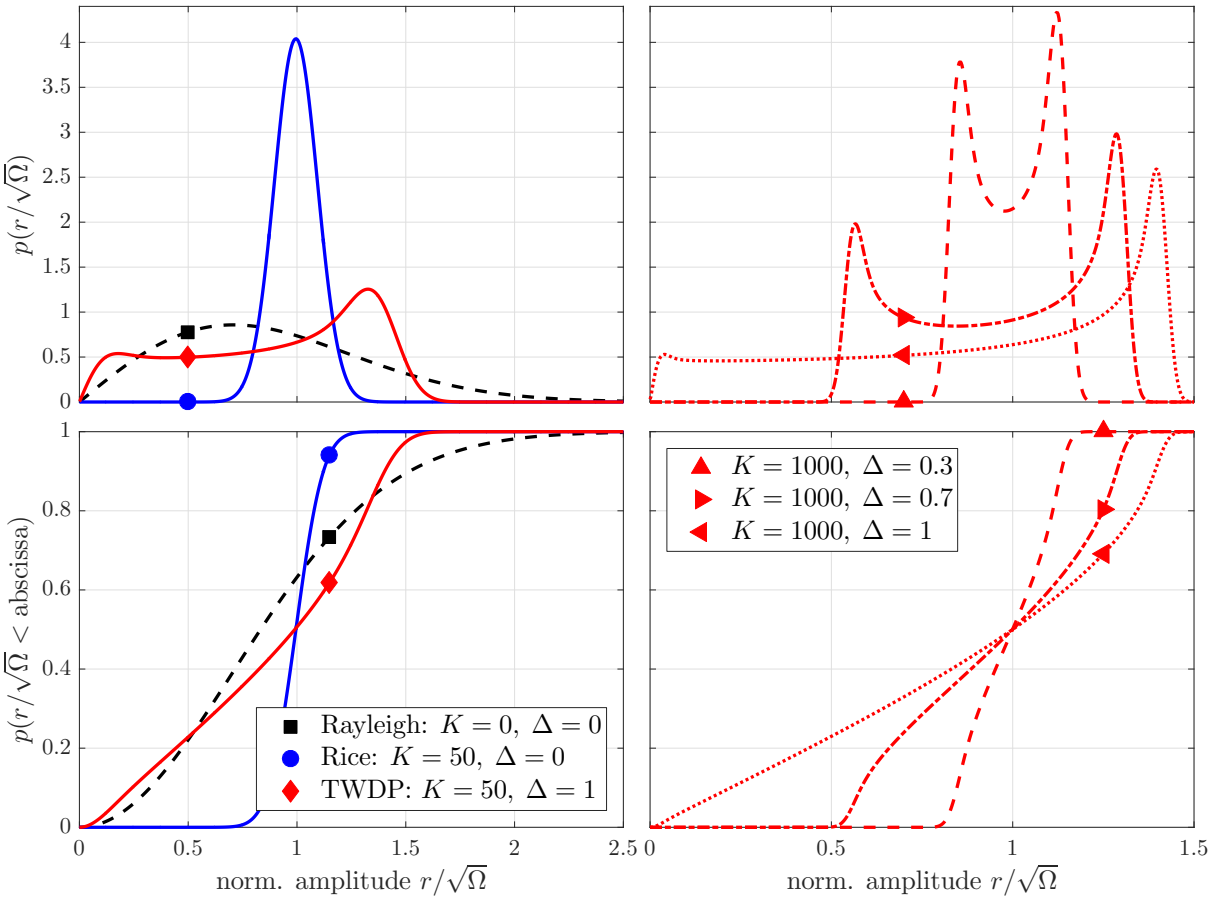

Figure 2.1: ***Comparison of Rayleigh, Rician, and TWDP fading.*** The top panels show PDFs while the bottom panels show CDFs. The probability of TWDP in deep fades is higher than that in a Rayleigh distribution. The right panels show distributions with higher K-factor.

which can eventually lead to fading that is more severe than Rayleigh [67–71]. The highest probability for deep fades occurs in TWDP fading (see again Fig. 2.1).

2.1.1 Data Preprocessing

Real-world measurement data do not follow Eq. (2.3), that is, they have $\Omega \neq 1$. To work with the equations introduced above, the measurement data is normalized by an estimate of $\hat{\Omega}$ obtained through the method of moments. The second moments Ω of Rician fading and TWDP fading are merely a scale factor [114, 115]. Notably, this research focuses more on the proper fit of K and Δ. Generally, estimation errors on Ω propagate in K and Δ estimates. However, [114] achieved an almost asymptotically efficient estimator with a moment-based estimation of Ω. The observed data is to accomplish the following three independent tasks:

(T1) Data normalization to $\Omega \equiv 1$,

(T2) Parameter estimation and model selection (Section 2.1.2), and

(T3) Model validation (Section 2.1.5)

Ideally, one would partition the data samples into three distinct sets, and each task is then performed within its own set. However, the observed data in this study are limited; thus, for (T2) and (T3) the same data is used in Chapter 3. Accordingly, the data is divided into only two sets. The first set $(r_1, \ldots, r_n, \ldots r_N)$ is taken for the parameter estimation of the tuple (K, Δ) described in Section 2.1.2, and for the hypothesis testing described in Section 2.1.5. The first set is carefully chosen to obtain envelope samples that are approximately independent and identically distributed. The second set $(r_1, \ldots, r_m, \ldots r_M)$ is the complement of the first set. The elements of the second set are used to estimate the second moment via

$$\hat{\Omega} = \frac{1}{M} \sum_{m=1}^{M} r[m]^2 \,, \tag{2.10}$$

where m is the sample index and M is the size of the second set. Partitioning is necessary to avoid the biases caused by the noise correlations $\hat{\Omega}$ and $(\hat{K}, \hat{\Delta})$ [116]. The estimated quantities are marked with $\hat{(\cdot)}$ in the sequel.

The data in Chapters 4 and 5 are very limited; thus, this study uses the suboptimal approach of moving average, similar to that applied by [87] to address the problem of data limitation. For data normalization, the window size L_f is bigger than that for parameter estimation. Thus, the data used in (T2) parameter estimation and model selection comes from a subset of the data used in (T1) normalization. The estimate of the time-varying second moment $\hat{\Omega}[m]$ is calculated as

$$\hat{\Omega}[m] = \mathrm{SA}\left(r[m], L_\mathrm{f}\right) = \frac{1}{I_\mathrm{U}[m] - I_\mathrm{L}[m] + 1} \sum_{m'=I_\mathrm{L}[m]}^{I_\mathrm{U}[m]} \left|r[m']\right|^2 \,, \tag{2.11}$$

where the lower and the upper sum index are

$$I_\mathrm{L}[m] = \max(0, \lceil m - {}^{L_\mathrm{f}}\!/_2 \rceil) \,, \tag{2.12}$$

$$I_\mathrm{U}[m] = \min(\lceil m + {}^{L_\mathrm{f}}\!/_2 \rceil, M-1) \,. \tag{2.13}$$

Due to limited data, physical arguments are used in Sections 4 and 5 instead of model validation.

2.1.2 Parameter Estimation and Model Selection

Note that the TWDP fading model in Eq. (2.1) does not contain noise; over the wide frequency range, the receive noise power spectral density of the measurement equipment is not equal. A valid statistical

noise description over the wide frequency range is frequency-dependent. Thus, to avoid the burden of frequency-dependent noise modeling, measurement samples that are weaker than ten times the noise power are discarded, and noise is ignored in the estimation.

Having the envelope measurement data set $(r_1, \ldots, r_n, \ldots r_N)$ at hand, a distribution in which the observed realization r_n is most likely to appear is needed. As such, the parameter tuple (K,Δ) is estimated via the maximum likelihood procedure

$$(\hat{K}, \hat{\Delta}) = \underset{K,\Delta}{\operatorname{argmax}} \sum_{n=1}^{N} \ln f_{\text{TWDP}}(r_n; K, \Delta) = \underset{K,\Delta}{\operatorname{argmax}} \sum_{n=1}^{N} \ln \frac{\partial F_{\text{TWDP}}(r_n; K, \Delta)}{\partial r} \,. \tag{2.14}$$

The symbol $f(\cdot)$ denotes probability density functions (PDFs) , n denotes the sample index, and N is the size of the set. To solve Eq. (2.14), K and Δ are discretized. Next, $\frac{\partial F_{\text{TWDP}}(r;K,\Delta)}{\partial r}$ is calculated for all parameters via numerical differentiation. Within this family of distributions, the parameter vector that maximizes the log-likelihood function in Eq. (2.14) is the ML estimate. Thus, the maximization is implemented as an exhaustive search in the (K, Δ) grid. To obtain the optimal Rice fit, the maximum log-likelihood value is investigated within the parameter slice ($K, \Delta \equiv 0$). Fig. 2.2 shows an exemplary fit of Rician and TWDP fading. As a reference, Rayleigh fading ($K \equiv 0, \Delta \equiv 0$) is shown as well.

Akaike's information criterion is used to be able to select between Rician fading and TWDP fading. AIC is a rigorous method for estimating the Kullback-Leibler divergence, that is, the relative entropy based on the maximum-likelihood estimate [73]. Given the maximum-likelihood fitted parameter tuple $(\hat{K}, \hat{\Delta})$ of TWDP fading and Rician fading, the sample size-corrected AIC [73, p. 66] is calculated for Rician fading (AIC_R) and TWDP fading (AIC_T). The expression is given as

$$\text{AIC} = -2 \sum_{n=1}^{N} \ln f_{\text{TWDP}}(r_n; \hat{K}, \hat{\Delta}) + 2U + \frac{2U(U+1)}{N-U-1} \,, \tag{2.15}$$

where U is the model order. For Rician fading the model order is $U = 1$, since just K is estimated. For TWDP fading $U = 2$, as Δ is estimated additionally. Due to the model order penalization in AIC, over-fitting is avoided. The second moment Ω (already estimated using a different data set before the parameter estimation) is not part of the ML estimation (Eq. 2.14), and is therefore not considered in the model order U. Accordingly, the lower AIC value decides between Rician fading and TWDP fading.

2.1.3 The Transition of TWDP Fading to Rician Fading

If, and only if, $\Delta = 0$, will TWDP fading degenerate mathematically to Rician fading. The actual transition from TWDP fading to Rician fading is smooth. If the second specular component becomes very small, then it can be absorbed equally well in the diffuse components. To study how the TWDP transitions to Rice distribution, the Δ-parameter, defined in Eq. (2.5) through amplitudes, is reexpressed as the power ratio

$$\delta P = \frac{V_2^2}{V_1^2} \,, \qquad V_2 \leq V_1 \quad \Rightarrow \quad \delta P \leq 1 \,. \tag{2.16}$$

As such, Eq. (2.5) now becomes

$$\Delta = \frac{2\sqrt{\delta P}}{1 + \delta P} \,. \tag{2.17}$$

The expression (2.17) is plotted in Fig. 2.3 (left-hand side) with δP expressed in decibels. At $\delta P < -20\,\text{dB}$, even an exponential power decrease would barely translate to different Δ values. At $\Delta \to 0$, depending on the K-factor, the second much weaker component might no longer be large enough to sufficiently change the distribution from the Rician distribution. Mathematically, this is expressed through the variance of the diffuse components. Remember, given that $\Omega \equiv 1$, σ solely depends on the K-factor, see

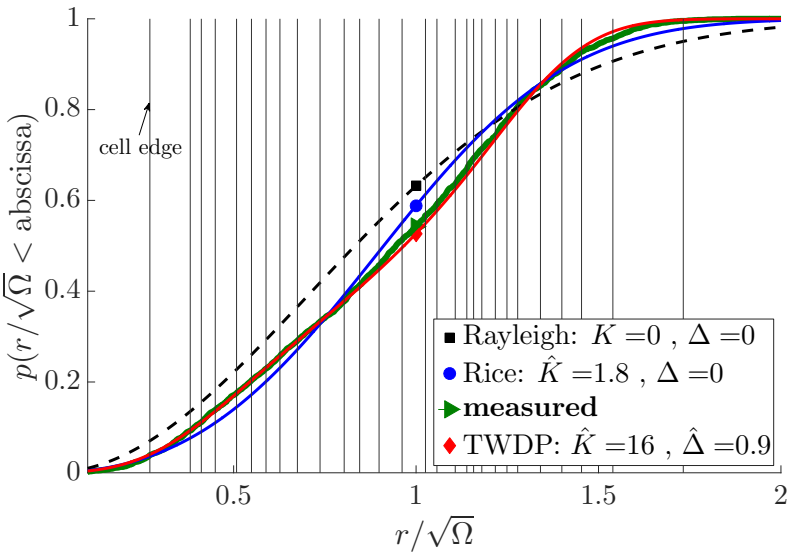

Figure 2.2: ***CDF: Distribution fitting for exemplary frequency domain measurement data.*** The figure illustrates the maximum likelihood fitted Rice distribution and the maximum likelihood fitted TWDP fading distribution. The Rician K-factor and the TWDP K-factor deviate significantly. Rayleigh fading is plotted as reference.

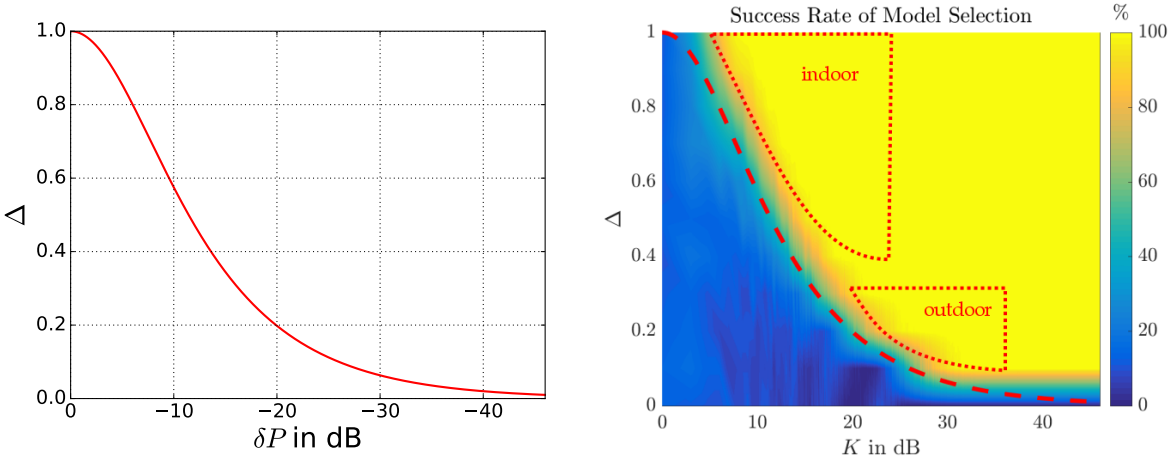

Figure 2.3: ***Transition to Rician Fading.*** (Left) The figure shows the Δ-parameter as a function of the power ratio δP of both specular non-fluctuating waves. (Right) This shows the success rate of selecting TWDP fading for all parameter tuples (K, Δ) of the grid search space. Whenever the second specular component is in the order of the diffuse components, the AIC model selection fails. The red dashed line replaces δP of Eq. (2.17) with $1/K$ to show this border. The marked regions show the found values in the following chapters.

Eq. (2.6). At $K \gg 0$, the power of the diffuse components (in decibels) is expressed as

$$10\log_{10}\sigma^2 \approx -10\log_{10}K - 3\,\text{dB}\,. \tag{2.18}$$

Hence, TWDP fading would only differ from Rician fading if $10\log_{10}\delta P \gg 10\log_{10}\sigma^2 \approx -10\log_{10}K - 3\,\text{dB}$. Otherwise, the second specular component would appear as strong as the diffuse components. This behavior directly translates to the model selection algorithm. To demonstrate this, in this study Monte Carlo simulations are run with synthetic data. In the test data, the K-factor is linearly spaced in $\{0, 1, \ldots, 100\}$ and logarithmically spaced with 150 points for each decade above, and the Δ-parameter is linearly spaced in $\{0, 0.1, \ldots, 1\}$. A total of 300 realizations of each pair (K, Δ) are generated; thereafter, the fitting and selection approach in Subsection 2.1.2 is performed. The simulation is considered successful whenever AIC decides correctly for the TWDP model. The success rate of TWDP selection is plotted in Fig. 2.3 (right-hand side).

On the right-hand side of Fig. 2.3, Eq. (2.17) is plotted on top as a red dashed line. From the considerations discussed above, it is already known that the K-factor must be at least above $3\,\text{dB}$. Observe that the transition region matches fairly well with those values, in which the power of the second specular component becomes as strong as that in the diffuse components. With increasing K-factor, the probability of selecting TWDP fading also increases rapidly. However, there is a minimum $\Delta \approx 0.1$, where TWDP fading selection fails even for $K \to \infty$. This value corresponds to a power difference of approximately $25\,\text{dB}$ in the LOS component and in the reflected component. With this proposed approach, it will not be possible to select the appropriate fading distribution, if the second specular component is much weaker.

This is a fundamental limitation; with small K-factor, there is a clear bias towards selecting Rician fading. Note that this approach is automatically *conservative in declaring that the observed data are considered TWDP fading*. Fig. 2.3 accordingly marks the regions where TWDP fading has been found in this thesis.

2.1.4 A Closer Look on the Transition Border

This subsection carefully distinguishes between the K-factor obtained as Rician fit (K_{Rice}) and the K-factor obtained as TWDP fit (K_{TWDP}). To study the transition boarder, Eq. (2.17) is first inverted to

$$\delta P = \frac{V_2^2}{V_1^2} = \frac{\left(1-\sqrt{1-\Delta^2}\right)^2}{\Delta^2}\,. \tag{2.19}$$

The K_{Rice}-factor is now calculated such that the power of the diffuse components exactly matches that of the second non-fluctuating amplitude, that is,

$$\frac{1}{K_{\text{Rice}}} = \frac{2\sigma^2}{V_1^2} \stackrel{!}{=} \frac{V_2^2}{V_1^2} = \frac{\left(1-\sqrt{1-\Delta^2}\right)^2}{\Delta^2}\,, \tag{2.20}$$

Hence, the maximum Rician K-factor, where a decision based on the AIC fails, is given as a function of Δ

$$K_{\text{Rice}}^{\max} = \frac{\Delta^2}{\left(1-\sqrt{1-\Delta^2}\right)^2} \approx \frac{4}{\Delta^2} \qquad \Rightarrow \qquad \Delta^{\max} \leq \frac{2}{\sqrt{K_{\text{Rice}}}}\,, \tag{2.21}$$

and the maximum possible Δ-parameter that could have been overlooked is thus also stated. Next, the strength of K_{Rice} as a function of the TWDP parameters needs to be addressed. To give better distinction, the TWDP K-factor is now denoted by

$$K_{\text{TWDP}} = \frac{V_1^2 + V_2^2}{2\sigma^2}\,. \tag{2.22}$$

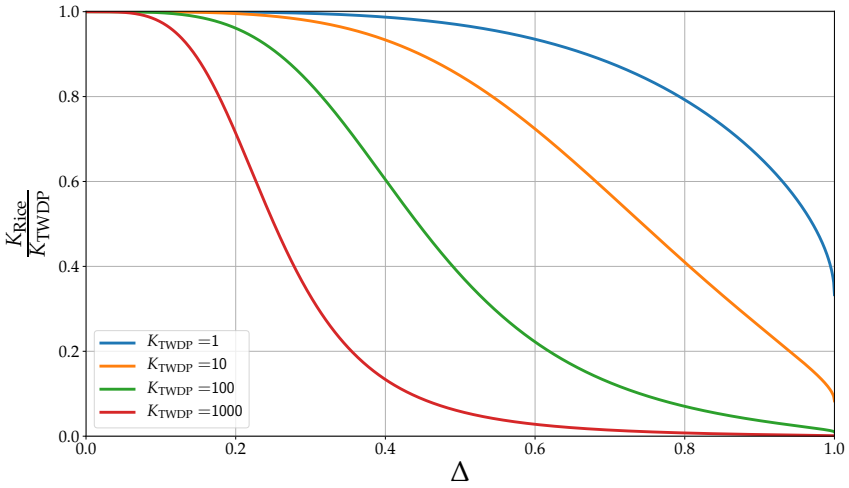

Figure 2.4: ***Relationship of the Rician and TWDP K-factor.*** The Rician fit and the TWDP fit will provide similar K-value estimates only at very small Δ values. Generally, a Rician fit underestimates the power of the specular components.

Note that V_2 is absorbed into the diffuse components in case of a Rician fit. At $\Omega \equiv 1$, the voltages V_1 and V_2 are given in Eq. (2.7) and σ^2 is given in (2.6). After some algebra, the following result is obtained

$$K_{\text{Rice}} = \frac{V_1^2}{V_2^2 + 2\sigma^2} = \frac{K_{\text{TWDP}} \left(\sqrt{1+\Delta^2} + \sqrt{1-\Delta^2}\right)^2}{K_{\text{TWDP}} \left(\sqrt{1+\Delta^2} - \sqrt{1-\Delta^2}\right)^2 + 2^2} \,. \tag{2.23}$$

There are obviously two extreme cases of Eq. (2.23). First, if $\Delta = 0$ and hence $V_2 \equiv 0$, then the Rician K-factor will be the same as the TWDP K-factor, that is, $K_{\text{Rice}} = K_{\text{TWDP}}$. Second, if $\Delta = 1$ and $V_2 \equiv V_1$, then the Rician K-factor is close to 1, since $K_{\text{Rice}} = \frac{K_{\text{TWDP}}}{K_{\text{TWDP}}+2} \overset{K_{\text{TWDP}} \gg 2}{\approx} 1$. This means that an ML estimate of TWDP data would almost provide a Rayleigh fit, thereby totally underestimating the power of the specular components (see Fig. 2.2 for an example). All points in between these extremes are shown in Fig. 2.4.

2.1.5 Validation of the Chosen Model

One of the two distributions (i.e., Rice or TWDP), will always yield a lower AIC value. To validate whether or not the chosen distributions explains the data, the following statistical hypothesis testing problem is stated:

$$\begin{aligned} \mathcal{H}_0 : &\begin{cases} F_{\text{Rice}}(r; \hat{K}), & \text{if } \text{AIC}_\text{R} \leq \text{AIC}_\text{T} \\ F_{\text{TWDP}}(r; \hat{K}, \hat{\Delta}), & \text{else} \end{cases} \\ \mathcal{H}_1 : &\begin{cases} \neg F_{\text{Rice}}(r; \hat{K}), & \text{if } \text{AIC}_\text{R} \leq \text{AIC}_\text{T} \\ \neg F_{\text{TWDP}}(r; \hat{K}, \hat{\Delta}), & \text{else} \end{cases} \end{aligned} \tag{2.24}$$

The Boolean negation is denoted by $\neg$. This study used the g-test as statistical tool [117, 118]. Meanwhile, the well-known chi-squared test approximates the g-test via a local linearization [119]. At a significance level α, a null hypothesis is rejected if

$$G = 2 \sum_{i=1}^{m} O_i \ln\left(\frac{O_i}{E_i}\right) \overset{?}{>} \chi^2_{(1-\alpha, m-e)} \,, \tag{2.25}$$

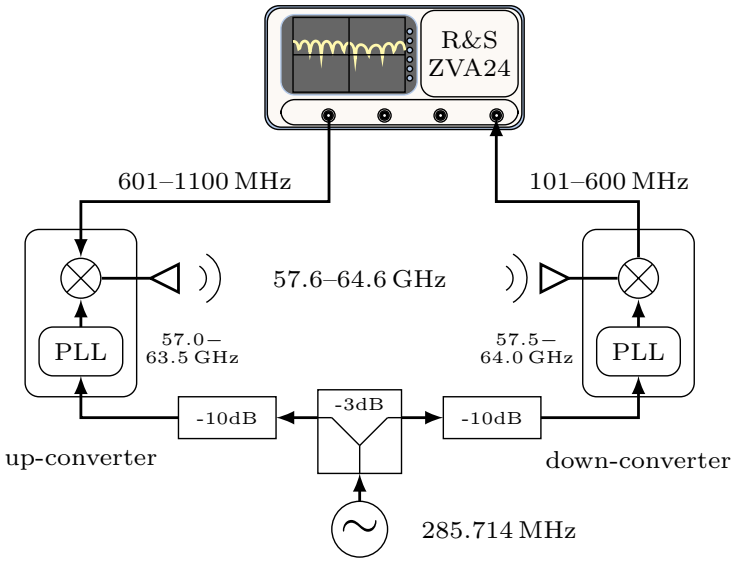

Figure 2.5: ***RF setup of the frequency-domain channel sounder.*** The combination of different PLL scaling factors allows for a measurement bandwidth of 7 GHz. The up-converter and the down-converter share a reference clock, and the power splitter has an isolation of 30 dB. To avoid possible leakage on the clock distribution network, attenuators are added to decouple both converters. The transfer function is then measured by applying the conversion gain (mixer) measurement option of the R&S ZVA24 VNA.

where O_i is the observed bin count in cell i, and E_i is the expected bin count in cell i under the null hypothesis $\mathcal{H}_0$. The cell edges are illustrated with vertical lines in Fig. 2.2. The cell edges are chosen, such that 10 observed bin counts fall into one cell. The estimated parameters of the model are denoted by e. For Rician fading $e = 2$ and for TWDP fading $e = 3$ (Ω, K, Δ). The $(1-\alpha)-$quantile of the chi-square distribution with $m - e$ degrees of freedom is denoted by $\chi^2_{(1-\alpha,m-e)}$. The prescribed confidence level is $1 - \alpha = 0.01$.

2.2 Measurement Setups

In this dissertation, three different channel sounders have been designed and then built. The first channel sounder is a frequency-domain channel sounder with high dynamic range and high bandwidth. The snapshot rate of this channel sounder is very slow; thus, it is only used for indoor measurements. Furthermore, this channel sounder only provides scalar measurement data.

On the other hand, the second (and third) channel sounder operate in the time-domain and provide vector-valued measurement data. The sounder was initially set up indoors to enable the author to cross-compare the results with those previously obtained and thereby expand the obtained knowledge. Afterward, vehicular channels were also measured using the time-domain channel sounder. Both channel sounder types were calibrated "back-to-back" to remove the influence of the measurement equipment.

2.2.1 Scalar-Valued Wideband Measurements

At the heart of the frequency-domain channel sounder is an R&S ZVA24 network analyzer. The vector network analyzer (VNA) directly measures up to 24 GHz. For mmWave up-conversion and down-conversion, modules from Pasternack [120] are employed. These modules are based on the radio frequency integrated circuits described in [121]. The up-converter module and the down-converter module operate built-in synthesizer phase-locked loops (PLLs), in which the local oscillator (LO) frequency

Table 2.1: Frequency-Domain Channel Sounder Parameters Used in Chapter 3

Parameter	Value
transmit antenna	20 dBi conical horn
transmit antenna heights	180 cm
receive antenna	20 dBi conical horn
receive antenna height	70 cm
dynamic range	58 dB
frequency sample spacing	$\Delta f = 2.5\,\text{MHz}$
bandwidth	$\text{BW} = 7\,\text{GHz}$
center frequency	$f_0 = 60\,\text{GHz}$

Table 2.2: Time-Domain Channel Sounder Parameters Used in Chapter 3

Parameter	Value
transmit antenna	20 dBi conical horn
transmit antenna height	170 cm
receive antenna	20 dBi conical horn
receive antenna height	90 cm
transmit power	$P_{\text{TX}} = 7\,\text{dBm}$
receiver sensitivity	$P_{\text{RX,min}} = -63\,\text{dBm}$
sub-carrier spacing	$\Delta f = 5\,\text{MHz}$
number of sub-carriers	$K = 401$
center frequency	$f_0 = 60\,\text{GHz}$
maximum alias free delay	$\tau_{\text{max}} = 100\,\text{ns}$
delay resolution	$\Delta\tau = 0.5\,\text{ns}$
recording time	$T_{\text{rec}} = 0.4\,\text{ms}$

is calculated as

$$f_{\text{LO}} = {}^{7}/_{4} \cdot s_{\text{PLL}} \cdot 285.714\,\text{MHz} \approx s_{\text{PLL}} \cdot 500\,\text{MHz}\,. \tag{2.26}$$

The scaling factor of the synthesizer PLL counters is denoted by s_{PLL}. For example, at $f_{\text{LO}} \approx 60\,\text{GHz}$, the scaling factor is $s_{\text{PLL}} = 120$. To achieve a measurement bandwidth of 7 GHz, the scaling factors of the PLL are swept over. This approach is similiar to the variable intermediate frequency (IF) concept proposed in [122]. The transfer function is then measured via the conversion gain (mixer) measurement option of the VNA to prevent cross talk, and the transmitter and receiver operate at different baseband frequencies, namely, 601 to 1100 MHz and 101 to 600 MHz. Note that changing the PLL scaling factors and sweeping the VNA over 500 MHz takes seconds. Hence, this setup is not suitable for dynamic measurements. However, this channel sounder is characterized by its high dynamic range of approximately 60 dB [40]. The setup is shown in Fig. 2.5.

An overview of the channel sounder parameters of the scalar-valued frequency domain setup is given in Table 2.1.

2.2.2 Vector-Valued Measurements

To avoid changing the PLL scaling factor, the bandwidth has to be limited up to the maximum bandwidth that the up-converter could support. As such, this limits the bandwidth to approximately 2 GHz [120,

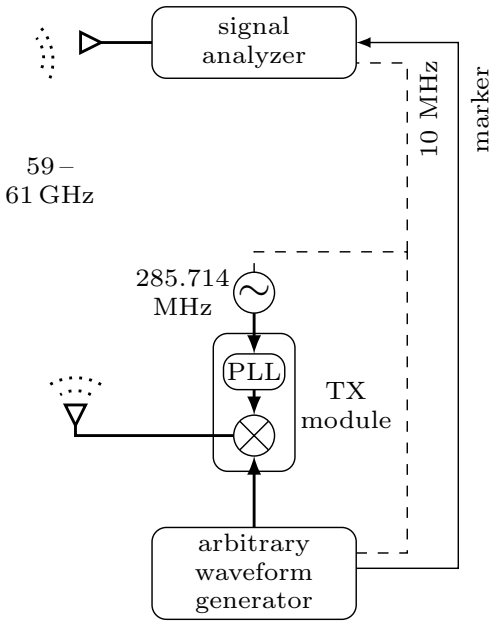

Figure 2.6: ***RF setup for the time-domain channel sounder.*** The VNA from Fig. 2.5 is replaced with an AWG and an SA. This setup allows to retrieve phase information as well. An option of the SA gives us direct access to the baseband IQ samples.

121]. Meanwhile, to avoid frequency sweeps, an arbitrary waveform generator (AWG) that operates at a sample rate of $30\,000$ MSamples/s is set up to be able to produce a 2 GHz wide waveform on the transmitter side. The transmitter (TX) sequence is repeated (for example, $2\,000$ times for the indoor measurements) to obtain a coherent processing gain of 33 dB for i.i.d. noise. The Pasternack up-converter (the same one previously used) shifts the baseband sequence to 60 GHz. A signal analyzer (SA) (R&S FSW67), with 2 GHz analysis bandwidth and with sensitivity $P_{\text{SA,min}} = -150$ dBm/Hz at 60 GHz, is used as a receiver. The received in-phase and quadrature-phase (IQ) baseband samples are obtained with an oversampling factor of 5. Hence, the receiver samples at a rate of $10\,000$ MSamples/s.

Meanwhile, the time-variant channel transfer function $H'[m', q]$ is calculated from the obtained IQ samples by using a discrete Fourier transform. This accordingly transforms the channel convolution into a multiplication within the frequency domain. Here, m' denotes the symbol time index, whereas $q = 0, \ldots, 400$ denotes the frequency index. After applying coherent averaging over $N = 2\,000$ baseband symbols, the resulting channel transfer function is then divided by the calibration function obtained from back-to-back measurements (this is done to equalize the frequency characteristics of the equipment). The obtained time-varying channel transfer function is accordingly denoted by $H[m, q]$.

Similar to the testbeds of [123–126], in which the authors analyzed LTE performance, proper triggering between the AWG and the SA ensures that the present setup has a stable phase between subsequent measurements. Frequency synchronization is achieved with a 10 MHz reference. The whole system is sketched in Fig. 2.6.

The excitation signal generated by the AWG is a multitone waveform. Using multitone waveforms has several advantages:

1. The frequency spectrum will be flat if all tone amplitudes are chosen equal. Hence, the SNR is constant across the bandwidth.

2. The individual tone phases offer design flexibility, and choosing them quadratically increasing reduces the peak-to-average power ratio [127–129]. This is necessary to maximize the average transmitted power while ensuring that all radio frequency (RF) components encountered by the

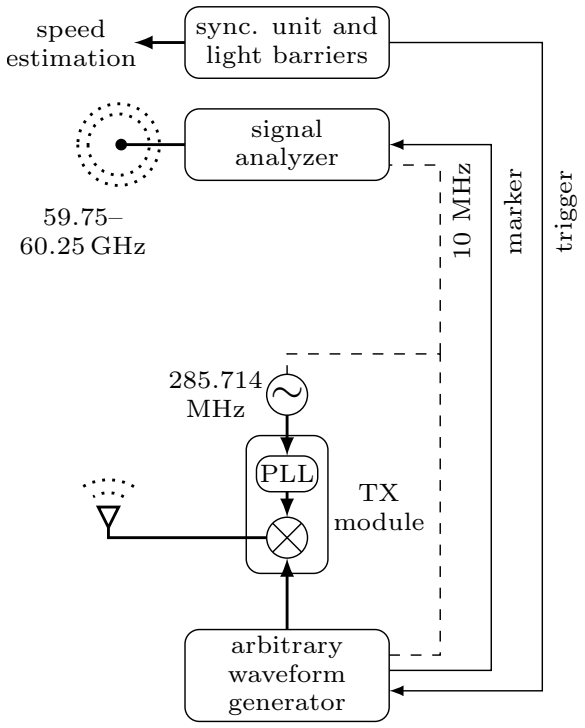

Figure 2.7: ***Extended time-domain channel sounder with synchronization unit.*** In addition to Fig. 2.6, a hardware trigger (a light barrier) triggers the AWG.

excitation signals operate in their linear regimes. Thus, the excitation signal reads

$$x[m] = \mathrm{Re}\left(\sum_{k=1}^{K/2} \mathrm{e}^{\mathrm{j}\pi \frac{k^2}{K}} \mathrm{e}^{-\mathrm{j}2\pi k \frac{m}{Q}} \right), \tag{2.27}$$

where $m = 0, \ldots, Q-1$ is the time index and $k = 1, \ldots, K/2$ is the tone index.

3. The tone spacing provides a trade-off between immunity against phase noise and aliasing in the delay domain. To make the symbols shorter and less susceptible to inter-carrier interference caused by phase noise and Doppler, the largest possible sub-carrier spacing Δf is chosen. Consequently, the chosen tone spacing is $5\,\mathrm{MHz}$; this large spacing assures that the phase noise does not limit the system [130]. However, the sampling theorem in the frequency domain needs to be obeyed; thus, $\Delta f \leq \frac{1}{(2\tau_{\max})} = 5\,\mathrm{MHz}$ must be fulfilled, where $\tau_{\max}$ is the maximum excess delay. The maximum excess delay is then $100\,\mathrm{ns}$.

4. Using multitone waveforms allows the setup to be flexible such that the bandwidth can be adapted via the number of "active" tones. For example, the system in the indoor measurement campaign operates with 401 tones. On the other hand, a reduced bandwidth is achieved in the vehicular outdoor measurements by using $K = 103$ tones. The receiver sensitivity can be adjusted as $P_{\mathrm{RX,min}} = P_{\mathrm{SA,min}} + 10\log_{10}(\Delta f) + 10\log_{10} K$.

Table 2.2 gives an overview of the channel sounder parameters for the time-domain channel sounding.

2.2.3 Triggered Vector-Valued Measurements

For this setup, a synchronization unit and light barriers extend the abovementioned time-domain channel sounder in order to capture dynamic events such as vehicle-to-everything communications. When a vehicle passes the first light barrier, the synchronization unit triggers the AWG that then plays back the

Table 2.3: Time-Domain Channel Sounder Parameters Used in Chapter 4

Parameter	Value
transmit antenna	20 dBi conical horn
transmit antenna heights	$70, 110, 146, 156$ cm
receive antenna	$\lambda/4$ monopole
receive antenna height	156 cm
transmit power	$P_{\text{TX}} = 7$ dBm
receiver sensitivity	$P_{\text{RX,min}} = -63$ dBm
sub-carrier spacing	$\Delta f = 5$ MHz
number of sub-carriers	$K = 103$
center frequency	$f_0 = 60$ GHz
maximum alias free delay	$\tau_{\text{max}} = 100$ ns
delay resolution	$\Delta\tau = 2$ ns
recording time	$T_{\text{rec}} = 720$ ms
snapshot rate	$T_{\text{snap}} = \begin{cases} 129.1\,\mu\text{s}, & \text{if } N = 640 \\ 112.9\,\mu\text{s}, & \text{if } N = 560 \\ 96.8\,\mu\text{s}, & \text{if } N = 480 \end{cases}$
maximum car speed	$v_{\text{car}} = \begin{cases} 9.7\,\text{m/s}, & \text{if } N = 640 \\ 11.1\,\text{m/s}, & \text{if } N = 560 \\ 12.9\,\text{m/s}, & \text{if } N = 480 \end{cases}$
maximum recording distance	$d_{\text{max}} = 9.3$ m

baseband sequence and a sample synchronous marker signal. The marker signal then starts recording the receive samples at the SA. A second light barrier is used to estimate the average speed of the vehicle. This hardware setup is illustrated in Fig. 2.7.

The link budget is more critical for outdoor measurements; thus, the bandwidth has been reduced to 510 MHz. To save memory space (and thereby enabling the setup to record longer sequences) the IQ samples are accessed at a rate of 600 MSamples/s. The setup is designed for a propagation loss (including antenna gains) of up to $P_{\text{L}} = 85$ dB.

Next, an SNR of 10 dB is required at each subcarrier. These requirements directly translate to the necessary transmit power of $P_{\text{TX,min}} = P_{\text{RX,min}}\big|_{K=103} + P_{\text{L}} + \text{SNR} = 32$ dBm. The maximum power of the TX module is 7 dBm. Thus, an additional processing gain of 25 dB is needed. The processing gain is realized by coherently averaging over $N = \{480, 560, 640\}$ multitone symbols. The number of averaging symbols is selected such that the averaged channel is still aliasing free. The least processing gain for fast vehicles ($N = 480$) is then 27 dB. Remember, the multitone system has a subcarrier spacing of approximately $\Delta f = 5$ MHz and has a sounding sequence length of $\tau_{\text{sym}} = 1/\Delta f = 200$ ns. The overall pulse length (including 480 repetitions) then totals to $T_{\text{snap}} = 96\,\mu$s. As such, by applying the sampling theorem for the Doppler support, a maximum alias-free Doppler frequency of $\nu_{\text{max}} = 1/(2T_{\text{snap}}) = 5.2$ kHz is obtained. This consequently limits the speed of overtaking cars to $v_{\text{car}} = (\lambda\nu_{\text{max}})/2 = 12.9\,\text{m/s} = 46.5\,\text{km/h}$. This value is sufficient for the measurements in this study as the street where the measurements took place has a speed limit of $30\,\text{km/h}$.

The receiver is limited to a memory depth of approximately 420 MSamples. With a sampling rate of 600 MSamples/s, $T_{\text{rec}} = 720$ ms of the channel evolution are recorded. At $12.9\,\text{m/s}$, this equals to a driving distance of 9.29 m. Table 2.3 gives an overview of the channel sounder parameters for the dynamic setup.

3 Indoor Measurement Campaigns

The initial results of the scalar-valued wideband measurements are discussed in

- Erich Zöchmann et al. "Directional Evaluation of Receive Power, Rician K-factor and RMS Delay Spread Obtained from Power Measurements of 60 GHz Indoor Channels". In: *Proc. of IEEE-APS Topical Conf. on Antennas and Propagation in Wireless Communications (APWC)*. 2016

Likewise, the initial results of the vector-valued measurements are in

- Erich Zöchmann et al. "Associating Spatial Information to Directional Millimeter Wave Channel Measurements". In: *Proc. of IEEE 86th Vehicular Technology Conference (VTC-Fall)*. 2017

The evaluation results of both measurement campaigns using the methodology discussed in Chapter 2 are in

- Erich Zöchmann et al. "Better than Rician: Modelling Millimetre Wave Channels as Two-Wave with Diffuse Power". In: *EURASIP Journal on Wireless Communications and Networking* 2019.1-17 (2019), p. 21

In this thesis, two indoor measurement campaigns under the same conditions are conducted using two different channel sounding concepts. The measured environment is an office/laboratory with office desks in the middle of the room and laboratory desks located by the window (see Fig. 3.1). The main interacting objects in the channel are office desks, a metallic refrigerator, a wall, and the surface of the laboratory desk. These objects are all marked in Fig. 3.1. Both measurement campaigns use 20 dBi horn antennas at the transmitter and at the receiver. The first indoor measurement campaign samples the channel in azimuth (φ) and elevation (θ) at the antenna in the middle of the laboratory. The sweeping antenna's (apparent) phase center [131, pp. 799] is fixed at a specific (x, y) – coordinate. Another static horn antenna is mounted in a corner of the laboratory (see again Fig. 3.1). The mechanical setups are explained in Sections 3.1 and 3.2.

Initially, the channel was sounded in the frequency-domain using the scalar network analysis described in Section 2.2.1. These channel measurements span over 7 GHz of bandwidth, which enables the fading in the *frequency domain* to be analyzed.

The setup in the second indoor measurement campaign described in Section 3.2 had to be improved mechanically and RF-wise. Now, the antenna's phase center is constant in the (x, y, z) – coordinate regardless of the antenna's elevation. Furthermore, the sounding concept is changed to time domain channel sounding to be able to analyze the *time domain* and to demonstrate channel impulse responses in Section 3.2.3. Moreover, by adjusting $(x, y, z, \varphi, \theta)$, the channel is sampled in the *spatial domain* in all directions (φ, θ). In Section 3.2.2, spatial correlations are obtained from the spatial, directional samples. As such, this study is able to *demonstrate TWDP fading* for directional mmWave indoor channels in the *frequency-domain*, in the *spatial-domain*, and in the *time-domain*.

3.1 Scalar-Valued Wideband Measurements

Directional measurements have been carried out in this study using the traditional approach of mechanically steered directional antennas [132, 133]. As already mentioned, the directional antennas are composed of 20 dBi conical horn antennas with an 18° 3 dB opening angle. The polarization is determined

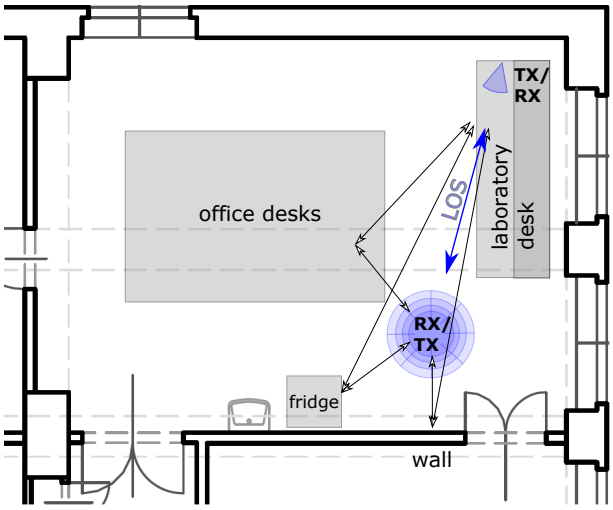

Figure 3.1: ***Floor plan of the measured environment.*** The floor plan indicates the multipath components that are visible in the measurement results. TX and RX switch roles in the second measurement. The TX/RX on the right upper corner of the room is always static. The RX/TX in the middle of the room is steerable, and is indicated by the spider's web.

by the LOS polarization. When TX and RX are facing each other at LOS, the polarization is co-polarized and the E-field is orthogonal to the floor. The essential mechanical adaptation in this study to the state-of-the-art directional channel sounding setup [39, 44] is that the elevation-over-azimuth positioner is mounted on an xy-positioning stage. Thus, the setup is capable of compensating for all the linear translations caused by the rotations and of keeping the phase center of the horn antenna always in the same (x, y) coordinate (see Fig. 3.2). The z coordinate is roughly $70\,\text{cm}$ above ground but varies $13\,\text{cm}$ for different elevation angles.

A wireless channel is said to be small-scale fading if the receiver (RX) cannot distinguish between the different MPCs. Depending on the positions of the TX, RX, and the interacting components, the MPCs can interfere either constructively or destructively [134, pp. 27]. The fading concept requires only a single frequency, in which its MPCs arrive at different phases to the RX. A statistical description of the fading process can then be found through spatial sampling. For now, the spatial (x, y) – coordinate (of TX and RX) is kept constant. Different phases of the impinging MPCs are realized by changing the TX frequency over a bandwidth of $7\,\text{GHz}$. Therefore, the parameter estimation relies on frequency translations. Fig. 3.3, shows the estimated received mean power of $7\,\text{GHz}$ bandwidth, normalized to the maximum RX power, that is

$$P_{\text{RX,norm.}}(\varphi, \theta) = \frac{\hat{\Omega}(\varphi, \theta)}{\max_{\varphi', \theta'}(\hat{\Omega}(\varphi', \theta'))} \,. \tag{3.1}$$

As already mentioned in Section 2.1.1, the frequency measurements are partitioned into two sets. The normalized receive power is calculated according to Eq. (2.10), with frequency samples spaced by $2.5\,\text{MHz}$. Every tenth sample is left out as these samples are used for fitting of (K, Δ) and for hypothesis testing. The directional results are then displayed via a stereographic projection from the south pole while using $\tan(\theta/2)$ as the azimuthal projection. All samplings points that lay at least $10\,\text{dB}$ above the noise level are the subjects of this study. They are displayed with red, white, or black markers in Fig. 3.3. The sampling points, where TWDP fading is determined by AIC following the procedure described in Section 2.1, are marked with red diamonds. The white circles mark the points where AIC favors Rician fading. Accordingly, four points are marked black. These points failed the null hypothesis test, and this study neither argues for Rician fading nor for TWDP fading. TWDP fading occurs whenever the LOS-link is not perfectly aligned or if the interacting object cannot be described by a single reflection. This is illustrated on the right-hand side in Fig. 3.3.

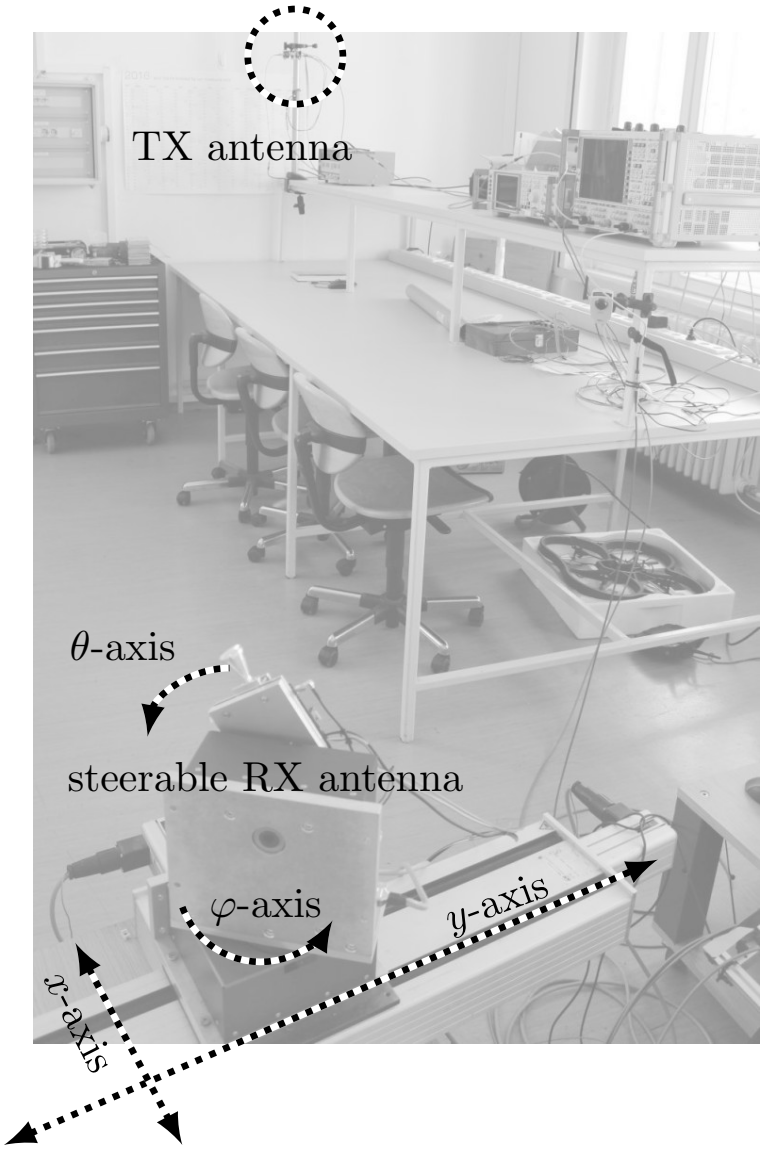

Figure 3.2: ***Photograph of the mechanical setup for the scalar-valued wideband measurements from the receiver's point of view.*** The receive antenna, a conical 20 dBi horn, is mounted on a multi-axis positioning and rotating system. The azimuthal and elevation angle are controlled to scan the whole upper hemisphere. The multi-axis system moves and rotates the horn antenna such that its phase center stays in the same (x, y) – coordinate during the directional scan.

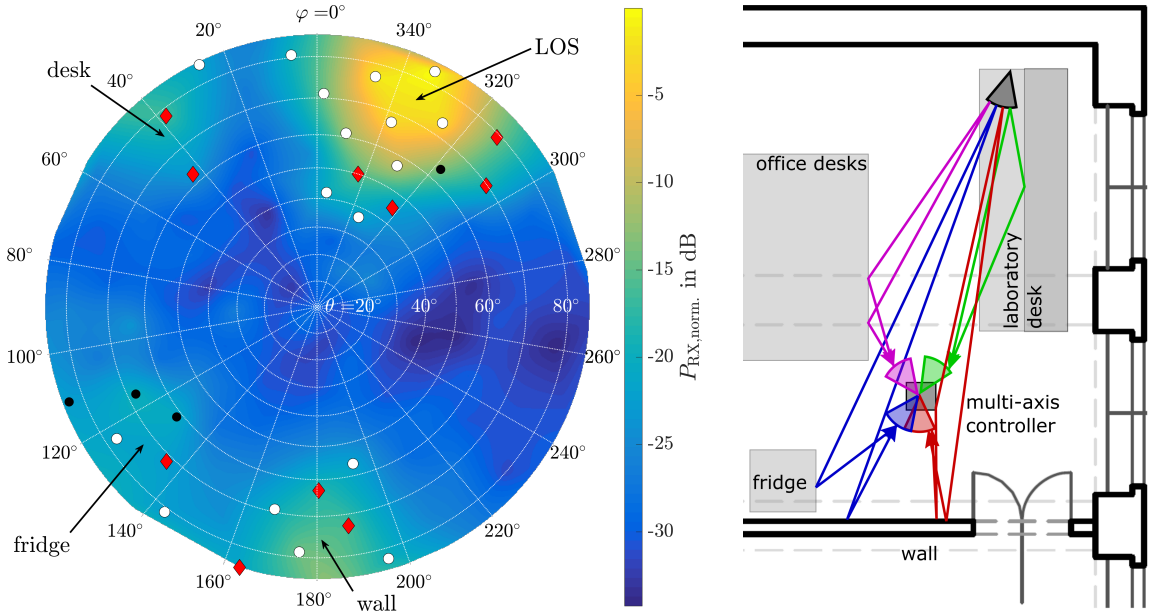

Figure 3.3: ***Estimated directional receive power of the scalar-valued wideband measurements.*** (Left) There are four main interacting objects leading to stronger receive power (marked in the figure). TWDP fading occurs whenever the LOS-link is not perfectly aligned or the reflecting structure is not perfectly plain. The red diamonds mark TWDP fading, while the white circles mark Rician fading. The black markers show the points where the hypothesis test rejects both distributions. Directions less than 10 dB above the noise level are not evaluated. (Right) This figure shows a simplified representation of the interfering waves that potentially lead to the TWDP model.

Fig. 3.4 illustrates the K-parameter of the selected hypothesis. It thereby shows either the Rician K-factor or the TWDP K-factor, depending on the selected hypothesis. Note that their definitions are fully equivalent. For Rician fading, the amplitude V_2 in (2.1) is zero by definition. Whenever the RX power is high, the K-factor is likewise high. Right of the K-estimate, the Δ estimate is shown. Here again, by definition, $\Delta \equiv 0$ whenever AIC decides for Rician fading. For interacting objects, the parameter Δ tends to be close to one. Note that decisions based on AIC choose TWDP fading mostly when Δ is relatively high (see the discussion in Section 2.1.3). Smaller Δ values do not sufficiently change the distribution function to justify a higher model order. Thus, the unsteady behavior in the model selection is explained. This is treated in more detail in the following section.

3.2 Vector-Valued Spatial Measurements

Another linear guide along the z-axis is added in the setup in order to compensate for all the introduced linear translations caused by the rotations. The phase center of the horn antenna is thereby lifted upwards by 1 m, and it is now fixed at a specific (x, y, z) coordinate in space. The whole mechanical setup and the fixed phase center are illustrated in Fig. 3.5. The 20 dBi conical horn antenna, together with the up-converter, is mounted on a five-axes positioner to be able to steer them directionally. Due to feasibility reasons, TX and RX now switch places. The RX in the form of the SA (see Section 2.2.2) is placed onto the laboratory desk. The RX 20 dBi conical horn antenna is directly mounted on the RF input of the SA; the RX antenna is not steered.

In contrast to the previous measurement campaign, this second setup no longer relies on frequency translations, and channel sampling is indeed done in space. Section 3.2.1 presents the fading results evaluated at a single frequency. Fading is hence exclusively determined by the obtained spatial samples.

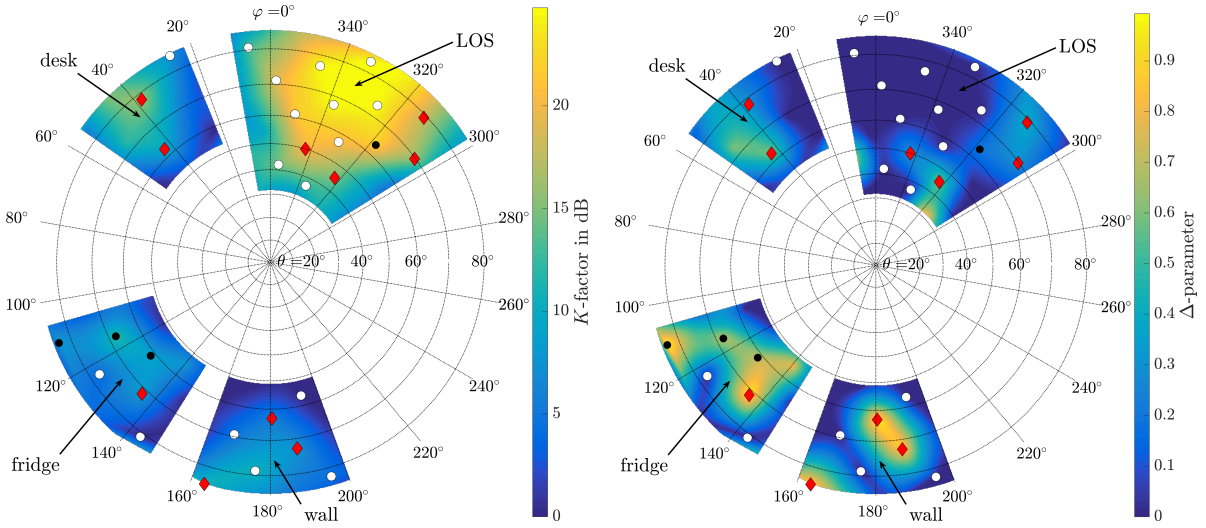

Figure 3.4: ***Estimated K-factor and Δ-parameter obtained through scalar wideband data.*** The K-factor estimate of the selected hypothesis is plotted. The K-factor behaves analogously to the RX power. At LOS, the K-factor is far above 20 dB. The desk reflection has a surprisingly high K-factor of about 15 dB. Other reflections have K-factors of approximately 10 dB. The Δ-parameter for reflections tends to be close to 1. The markers in this figure have the same meaning as those in Fig. 3.3.

3.2.1 Receive Power and Fading Distributions

To estimate the RX power, a sweep through the azimuth and elevation is performed at a single coordinate using the whole bandwidth of 2 GHz. The LOS and wall reflection from the scalar-valued wideband measurements are still visible in Fig. 3.6. Fading is then evaluated at a single frequency as discussed in the subsection below. Nevertheless, Fig. 3.6 already marks the fading distributions to help gain better orientation for the succeeding discussions.

The steerable horn antenna is above the office desks and above the refrigerator, thus, these interacting objects do not become apparent. In case the steerable TX does not accurately hit the RX at LOS, the desk surface acts as a reflector; a TWDP model then explains the data. For wall reflections, TWDP also best explains the data.

To obtain different spatial realizations, with the horn antenna pointing toward the same direction, the coordinate of the apparent phase center is moved to (x, y, z)−positions and is uniformly distributed within a cube of side length 2.8λ, see Fig. 3.7. The cube is regularly sampled by $9 \times 9 \times 9 = 729$ directional measurements, which consequently results in spacing between spatial samples of 0.35λ in every direction. Although $\lambda/2$ sampling is quite common [50, 53], the sampling frequency is co-prime with the wavelength to circumvent periodic effects [135]. Spatial samples are drawn only in those directions with strong reception levels as it would take more than three days to draw them in all directions.

The measurements are partitioned into two sets similar to that done in the previous section. The partitioning is made according to a 3D checkerboard pattern. The second moment $\hat{\Omega}$ is estimated from the first set and the parameter tuple (K, Δ) is estimated from the second.

The best-fitting K-factors in both regions with strong reception are illustrated on the left-hand side in Fig. 3.8, while the right-hand side illustrates the Δ-parameters. Similar to Fig. 3.4 the interaction with the wall has regions that are best modeled via TWDP fading. Remember, the RX in the form of an SA is now on the laboratory desk. In case the TX is not perfectly aligned, a reflection from the desk surface yields a fading statistic that is captured by the TWDP model. However, it seems akward that in the marked angle ("table surface"), TWDP fading occurs at $\Delta = 0.6$ and with a relatively high K-factor; but only at 10° shifted azimuth, Rician fading with weak K-factor takes place. Fig. 3.9 shows the emperical

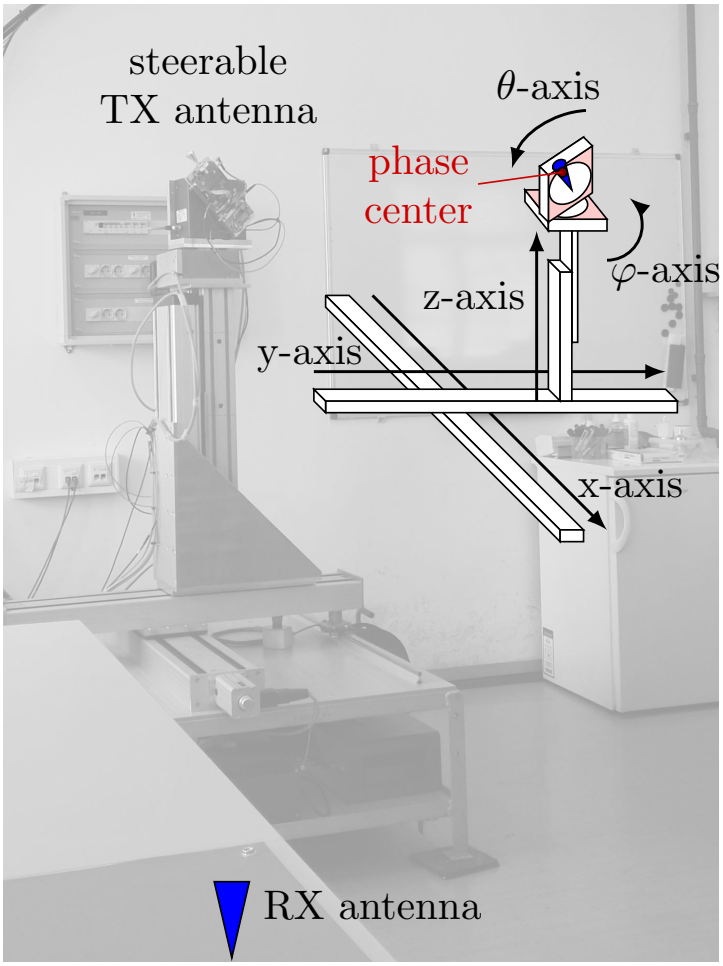

Figure 3.5: ***Photograph of the improved mechanical setup for the vector-valued measurements from the receiver's point of view.*** The mechanical setup now consists of five independent axes such that it is able to fully compensate for all the offsets introduced by the rotation. A schematic sketch is superimposed. All five axes are necessary to rotate the horn antenna around the phase center at a fixed (x, y, z) coordinate. Notice that TX and RX switch positions unlike in Fig. 3.2.

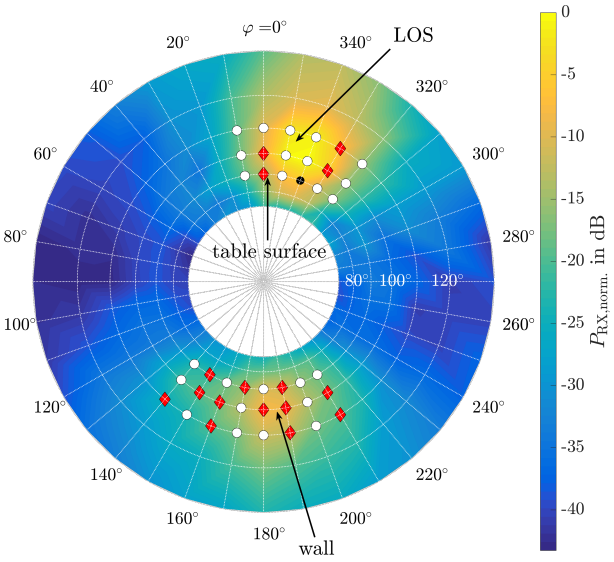

Figure 3.6: ***Estimated directional receive power of vector-valued measurements.*** Due to the elevated position of the steerable horn antenna, two interacting objects from Fig. 3.3 (i.e., the desk and the refrigerator) are no longer visible. LOS and the wall reflection are still present.These regions are the only ones that are spatially sampled. The markers have the same meaning as those in Fig. 3.3.

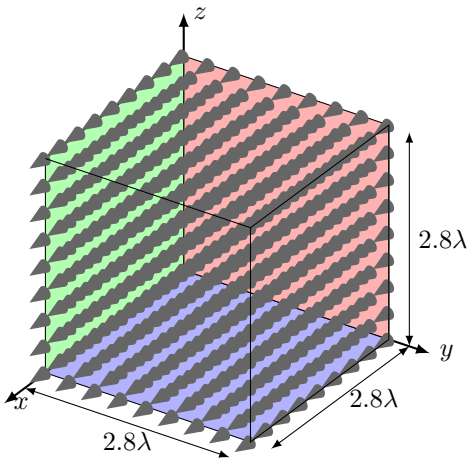

Figure 3.7: ***Spatial sampling grid.*** In one specific direction, $9 \times 9 \times 9 = 729$ samples are drawn uniformly from a cube of side length 2.8λ. The distance between samples is 0.35λ with a repeat accuracy of $\pm 0.004\lambda$. The orientation of the horn antenna is indicated via the cone shape in the sampling points.

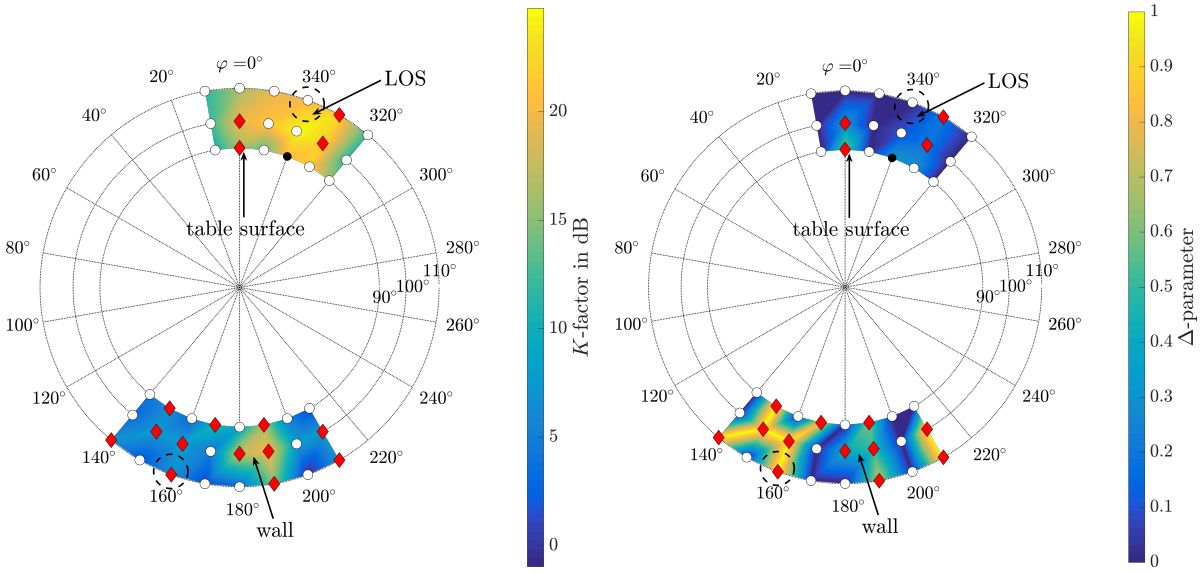

Figure 3.8: ***Estimated K-factor and Δ-parameter of the vector-valued measurements.*** Due to the elevated position, the K-factor of the wall reflection is higher than the previous measurements in Fig. 3.4 by 6 dB. If the beam is not perfectly aligned, then Rician fading turns again into TWDP fading. The wall reflections described by TWDP fading have a Δ-parameter close to one. The table surface reflection leads to a significantly smaller reflected component ($\Delta \ll 1$). The encircled sampling points are the subject of further study in Sections 3.2.2 and 3.2.3. The markers have the same meaning as those in Fig. 3.3.

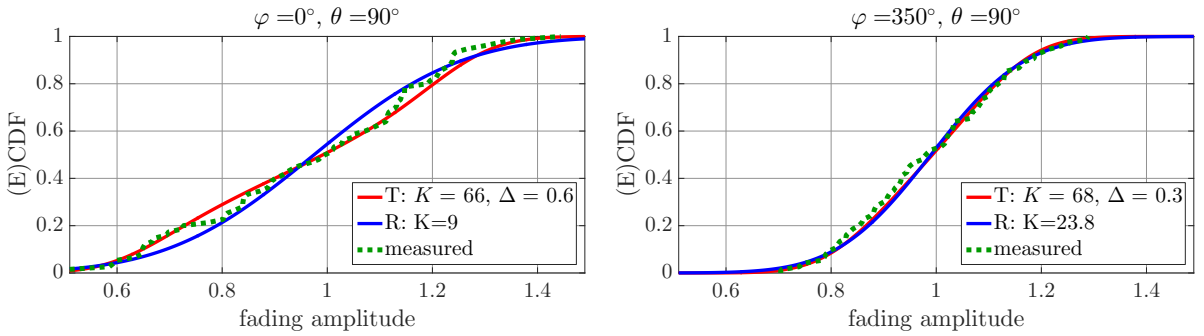

Figure 3.9: ***Laboratory desk surface reflection.*** (Left) At $\varphi = 0°$, the surface reflection is relatively strong, and the Δ parameter is large enough to let AIC decide in favor of TWDP fading. (Right) At $\varphi = -10° = 350°$, the relative strength of the surface reflection is not enough to decide in favor of TWDP fading.

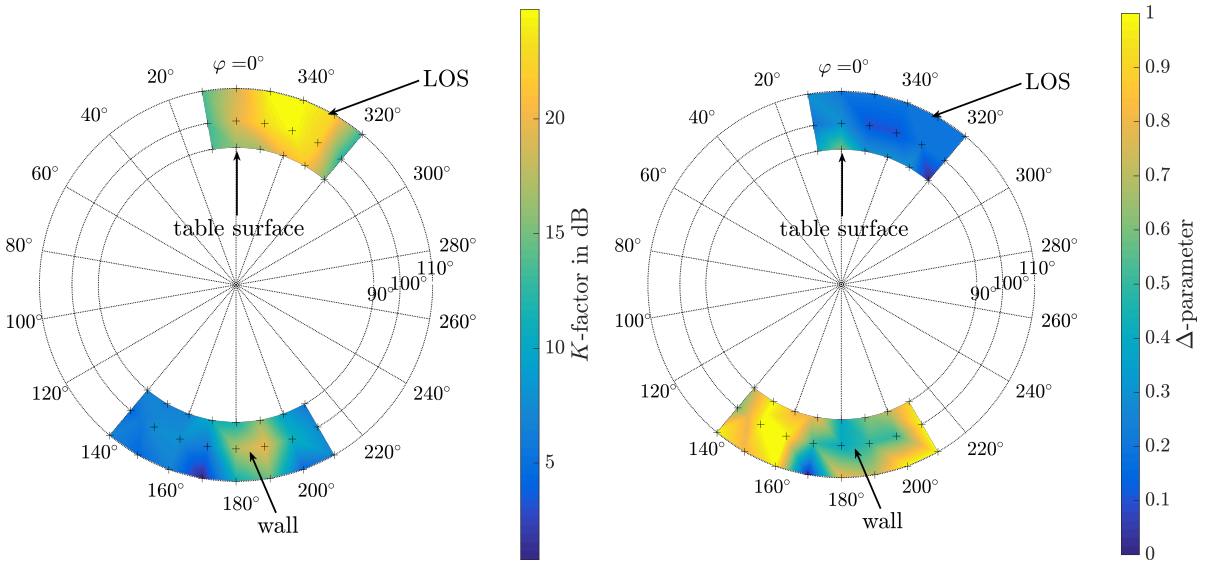

Figure 3.10: ***Estimated*** (K, Δ) ***parameter tuple of the TWDP fading model.*** The black crosses illustrate the marker position from Fig. 3.8. Taking only the TWDP model into account, the K and Δ values look much smoother, and clear regions are now visible.

(measurement) CDFs and the ML fits of the discussed angles. At an azimuth angle of $\varphi = 0°$ and an elevation angle of $\theta = 90°$, the surface reflection is stronger than the LOS component while the $\Delta = 0.6$ parameter is large enough to let the AIC decide in favor of TWDP fading with $K = 66$. In Fig. 2.3, one would read that $\Delta = 0.6$ would correspond to a power difference of approximately $10\,\text{dB}$ between the stronger LOS component and the surface reflection. At an azimuth angle of $\varphi = -10° = 350°$ and again at $\theta = 90°$, the estimated TWDP K-factor is close to the K-factor previously obtained, which is now $K = 68$. However, the Δ-parameter is reduced to $\Delta = 0.3$, which corresponds to a power difference between LOS and the surface reflection of approximately $16\,\text{dB}$. By turning the antenna by $10°$, the LOS component becomes better aligned and stronger than before. Furthermore, the table surface is now illuminated with a lower gain value. Fig. 3.10 now shows all parameter tuples (taking only TWDP fading into account) instead of just focusing on two neigboring points. The "jumpy" behavior between neighbors is now gone, and clear regions of high K-factors or high Δ-parameters are now visible.

3.2.2 Efficient Computation of the Spatial Correlation

This part further analyzes the wall reflection. In particular, the spatial correlations among the drawn samples are evaluated, and the three-dimensional cube sampling problem (see again Fig. 3.7) is now treated via two-dimensional slicing. The Wiener–Khintchine–Einstein theorem, which relates the autocorrelation function of a wide-sense-stationary random process to its power spectrum [136], is then applied to calculate the spatial (2D) autocorrelation function. In two dimensions, this theorem reads [137, 138]

$$\mathcal{F}_{2D}\left\{\boldsymbol{C}(x,y)\right\} = S(x',y')\,, \tag{3.2}$$

where $\boldsymbol{C}$ is the 2D-autocorrelation and S is the power spectral density of a 2D signal. The operator $\mathcal{F}_{2D}$ denotes the 2D Fourier transform. All 2D autocorrelation functions $\boldsymbol{C}^{(z,f)}$ of one $x-y$ slice are calculated at height z in a single frequency f through

$$\mathcal{F}_{2D}\left\{\boldsymbol{C}^{(z,f)}(x,y)\right\} = \mathcal{F}_{2D}\left\{\,\mathrm{Re}\left\{\boldsymbol{H}^{(z,f)}(x',y')\right\}\right\} \odot \mathrm{conj}\left\{\mathcal{F}_{2D}\left\{\,\mathrm{Re}\left\{\boldsymbol{H}^{(z,f)}(x',y')\right\}\right\}\right\}. \tag{3.3}$$

LOS:

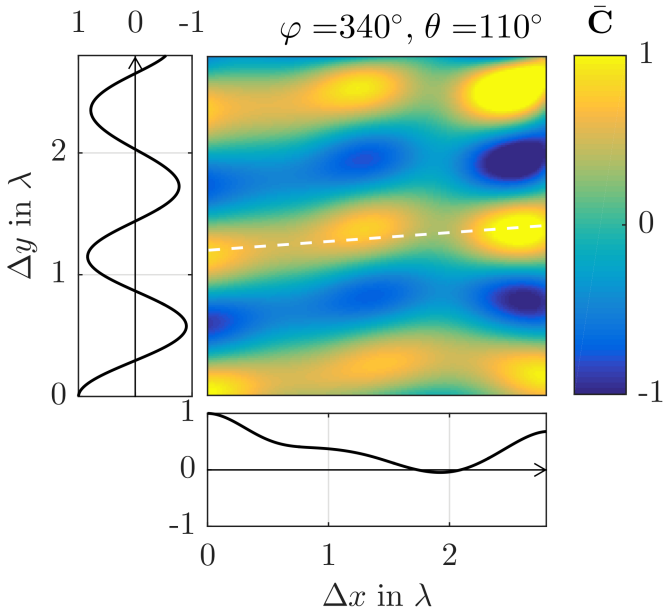

WALL:

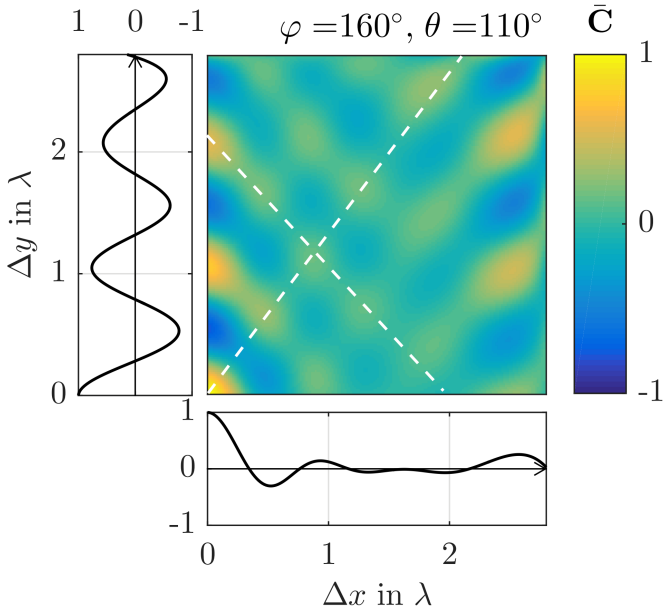

Figure 3.11: ***Spatial correlation plot at*** $\varphi = 160°, 340°$ ***and at*** $\theta = 110°$**.** For the wall reflection at $\varphi = 160°$, the pattern shows an interference of two plane waves, and thus supports the TWDP fading assumption. For LOS at $\varphi = 340°$, a spatial correlation pattern is observed to be dominated by one wave. The white dashed lines illustrate the plane wave phase fronts.

All channel samples are collected in the matrix $\boldsymbol{H}$. The symbol $\odot$ denotes the Hadamard multiplication while the operator $\mathrm{conj}\{\cdot\}$ denotes complex conjugation. To ensure a real-valued autocorrelation matrix (instead of a generally complex representation [138]) from the complex-valued channel samples, only the real parts $\mathrm{Re}\{\cdot\}$ are taken. The spatial autocorrelation of the imaginary parts are identical, and one could also analyze the magnitude and phase individually. Although the correlation of the magnitude stays almost at 1, the phase correlation patterns are similar to those of the real part, see [139] for the phase correlation pattern.

The 2D Fourier transform $\mathcal{F}_{2D}$ is realized via a 2D discrete Fourier transform (DFT), which is calculated by multiplying the DFT matrix $\boldsymbol{D}$ from the left and the right. To mimic a linear convolution using the DFT, zero padding is necessary. The studied matrix $\widetilde{\boldsymbol{H}}^{(z,f)}$ is hence given as

$$\widetilde{\boldsymbol{H}}^{(z,f)} = \begin{pmatrix} \mathrm{Re}\{\boldsymbol{H}^{(z,f)}\} & \boldsymbol{0} \\ \boldsymbol{0} & \boldsymbol{0} \end{pmatrix} . \tag{3.4}$$

Furthermore, the finite spatial extend of the samples acts as rectangular window, which consequently leads to a triangular envelope of the autocorrelation function. This windowed spatial correlation is denoted by

$$\boldsymbol{C}^{(z,f)}_{\text{windowed}} = \boldsymbol{D}^H \Big(\big(\boldsymbol{D} \widetilde{\boldsymbol{H}}^{(z,f)} \boldsymbol{D} \big) \odot \mathrm{conj} \left\{ \boldsymbol{D} \widetilde{\boldsymbol{H}}^{(z,f)} \boldsymbol{D} \right\} \Big) \boldsymbol{D}^H . \tag{3.5}$$

The spatial correlation of the rectangular window, which is constructed in accordance with Eq. (3.4), is then calculated to compensate for the windowing effect. This is expressed as

$$\boldsymbol{S} = \boldsymbol{D}^H \left(\left(\boldsymbol{D} \begin{pmatrix} \mathbb{1} & \boldsymbol{0} \\ \boldsymbol{0} & \boldsymbol{0} \end{pmatrix} \boldsymbol{D} \right) \odot \mathrm{conj} \left\{ \boldsymbol{D} \begin{pmatrix} \mathbb{1} & \boldsymbol{0} \\ \boldsymbol{0} & \boldsymbol{0} \end{pmatrix} \boldsymbol{D} \right\} \right) \boldsymbol{D}^H . \tag{3.6}$$

The matrix $\mathbb{1}$ denotes the all-ones matrix. Matrix $\boldsymbol{S}$ compensates the truncation effect of the autocorrelation through element-wise (Hadamard) division, which is denoted by $\oslash$. Finally, the efficient computation of the spatial correlation (3.3) reads as

$$\boldsymbol{C}^{(z,f)} = \boldsymbol{C}^{(z,f)}_{\text{windowed}} \oslash \boldsymbol{S} . \tag{3.7}$$

Eq. (3.7) is then applied to all (parallel) 2D slices and to all frequencies. All realizations in z and f are averaged as

$$\bar{\boldsymbol{C}} = \frac{1}{9} \frac{1}{401} \sum_{z=1}^{9} \sum_{f=1}^{401} \boldsymbol{C}^{(z,f)} . \tag{3.8}$$

At a distance of 0.35λ, the measurement data is still correlated[1], and thus the correlation results can be viewed on the finer, interpolated grid. The chosen interpolation factor is 20, which means that the spatial correlations are plotted on a grid of $0.35\lambda/20 = 0.0175\lambda$ distance. Additionally, the one-dimensional autocorrelation functions, evaluated along x and y, are plotted together with their two-dimensional representations. Fig. 3.11 illustrates the two spatial correlation plots, which are evaluated at an azimuth angle of $\varphi = 340°$ and $\varphi = 160°$. Both plots have an elevation angle of $\theta = 110°$. The top part of Fig. 3.11 shows a spatial correlation pattern that is dominated by a single wave. The spatial correlation below shows an interference pattern, which is intuitively explained by a superposition of two plane waves. The one-dimensional correlations, which are evaluated either on the x-axis or on the y-axis, also show this oscillatory behavior.

[1] More specifically, at 0.35λ one is left of the first zero of the autocorrelation function

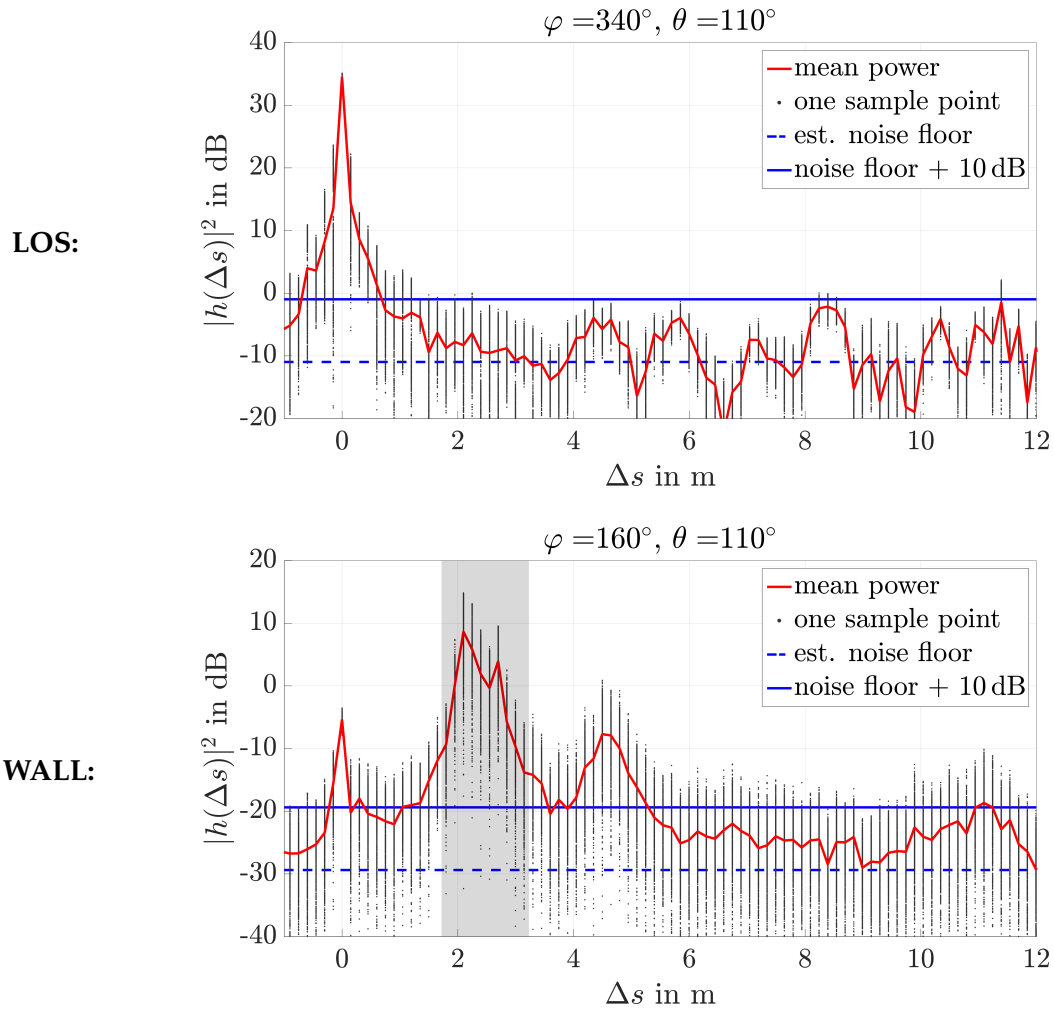

Figure 3.12: ***Scatter-plot of the CIRs.*** The CIRs are plotted as a function of spatial distance, where $\Delta s = 0$ corresponds to the LOS distance. The spatial resolution (a channel tap) is 15 cm. The spatial extend of the sampled cube (729 samples) is $2.8\lambda = 1.4$ cm, which is a magnitude smaller than the spatial resolution. The scatter-plot is evaluated at a wall reflection ($\varphi = 160°$) and at LOS ($\varphi = 340°$). The mean power is plotted with a continous red line. It can be observed that the arrival cluster centered at 2.5 m fades very deeply. The gray highlighted region around 2.5 m is further analyzed in Fig. 3.13.

3.2.3 Time-Gated Fading Results

It needs to be confirmed that the observations are not just mere artifacts of the measurement setup (e.g., back-lobes of the horn antenna); thus, the wireless channel is now studied in the time domain. The 2 GHz wide vector-valued measurements allow for a time resolution of approximately 0.5 ns, which corresponds to a spatial resolution of 15 cm. The channel impulse response (CIR) is plotted as a function of distance, namely, the LOS excess length Δs, that is

$$h(\Delta s) = h\big((\tau - \tau_{\text{LOS}})c_0\big)\,. \tag{3.9}$$

Figure 3.12 displays the scatter-plot (of all sample positions) of the LOS CIRs at $\varphi = 340°$ and the wall CIRs for $\varphi = 160°$. The steerable TX is positioned more than 1 m apart from the wall, which translates to an excess distance of approximately 2-3 m. At this excess distance, a cluster of multipath components is present. Note that if the horn antenna points toward the wall, the wave emitted by the back-lobe of the horn antenna is received at zero excess distance. Still, the receive power of the back-lobe is far below the

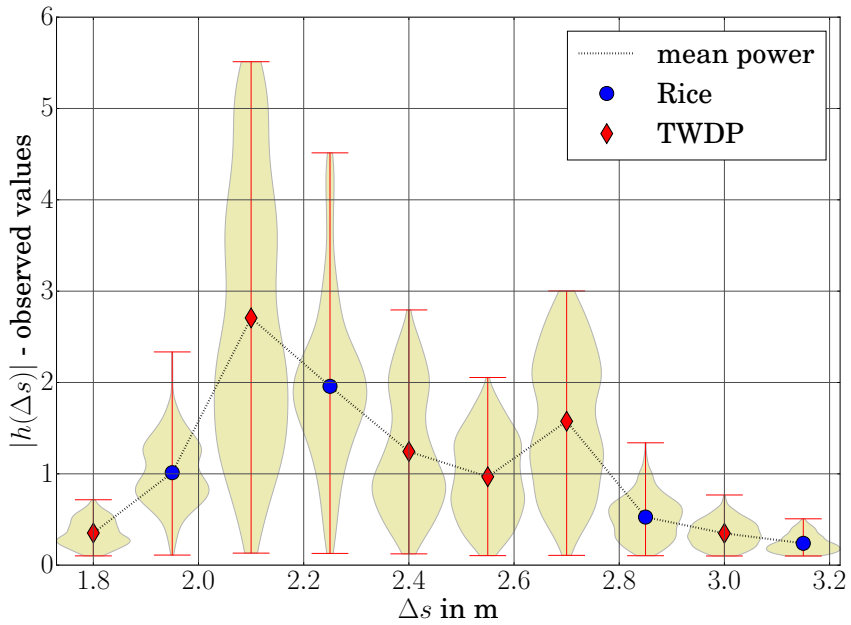

Figure 3.13: ***Violin-plot of the CIR time-gated for the wall reflection.*** This figure shows a zoom-in view of the gray highlighted region in Fig. 3.12. In contrast with Fig. 3.12, the y-axis is in linear scale; thus, the violin plot indicates the distribution at each tap. The marker shows the mean value. The marker style codes the best-fitting distribution.

components arriving from the wall reflection. Fading is hence determined by the wall scattering behavior. The gray highlighted region in Fig. 3.12 (bottom part) shows a reflection cluster that corresponds to the excess distance of the wall reflection. The distributions of each channel tap are represented by a violin plot in Fig. 3.13. A violin plot illustrates the distribution estimated via Gaussian kernels [140]. As such, Fig. 3.13 clearly demonstrates that the TWDP-decided distributions have multiple modes. The AIC decisions are plotted as markers at the mean power levels.

4 Outdoor Vehicular Measurement Campaign

The initial results of the outdoor measurement campaign have been presented at and subsequently published in

- Erich Zöchmann et al. "Measured Delay and Doppler Profiles of Overtaking Vehicles at 60 GHz". In: *Proc. of the 12th European Conference on Antennas and Propagation (EuCAP)*. 2018

The results of the preliminary evaluation based on the local scattering function (LSF) has been presented at and subsequently published in

- Erich Zöchmann et al. "Statistical Evaluation of Delay and Doppler Spread in 60 GHz Vehicle-to-Vehicle Channels During Overtaking". In: *Proc. of IEEE-APS Topical Conference on Antennas and Propagation in Wireless Communications (APWC)*. 2018

The simplified model of the parameter evolution has been submitted to

- Erich Zöchmann, Herbert Groll, and Stefan Pratschner. "A Small-Scale Fading Model for Overtaking Vehicles in a Millimeter Wave Communication Link". In: *Proc. of IEEE 20th International Workshop on Signal Processing Advances in Wireless Communications (SPAWC)*. submitted. 2019

An evaluation based on the proposed methodology in Chapter 2 is published in

- Erich Zöchmann et al. "Position-Specific Statistics of 60 GHz Vehicular Channels During Overtaking". In: *IEEE Access* 7 (2019), pp. 14216–14232

In this thesis, a set of $60\,\mathrm{GHz}$ V2V channel realizations have been measured to capture the effect of an overtaking vehicle. The scenario is as follows: two cars are driving along a road, with one behind the other. Both are keeping a constant distance, and are communicating with each other via a $60\,\mathrm{GHz}$ mmWave link. A third vehicle overtakes this communicating car platoon, and thus influences the wireless channel. The extent of the effect depends on the relative position of the overtaking car. Similar results will be obtained if the car platoon overtakes a vehicle. This experiment in a real-world street environment is designed to make the experiment as controllable as possible. The wireless link is always in LOS and unblocked. The vehicular channel data evaluated consists of 30 different measurement runs. The effect of overtaking cars is observed at excess speeds of up to $13\,\mathrm{m/s}$.

At the TX site, a horn antenna with an $18°$ half-power beam width is used and aligned toward the RX car. The directive horn antenna filters out reflected MPCs from the surrounding buildings. On the other hand, a custom-built omnidirectional $\lambda/4$ monopole antenna is used at the RX site. The RX antenna has an omnidirectional pattern; thus, the scattered waves from the passing vehicle are not filtered out. This situation occurs, for example, in directional neighbor discovery [143], in which only one link end applies beamforming. The RX equipment is put into a static (parked) car, with the RX antenna fixed on the left rear car window. The TX is approximately $15\,\mathrm{m}$ behind the RX car. Single reflections on the TX car do not occur because of the directivity of the horn antenna, while double reflections involving the TX car are below the receiver sensitivity. Hence, the TX car is omitted and replaced by a simple tripod mounting. The TX and RX placement is shown in Fig. 4.1 and Fig. 4.2.

To simplify the measurements, neither the TX nor the RX moves; both are instead kept static, and the overtaking car is emulated by urban street traffic passing by. As previously indicated, this approach is valid because the reflections of the houses and other static objects are negligible due to the directivity of the TX horn antenna. The relative velocity of the overtaking vehicle determines the Doppler shift. The studied case corresponds to a "moving frame of reference". Keeping the TX and RX static makes

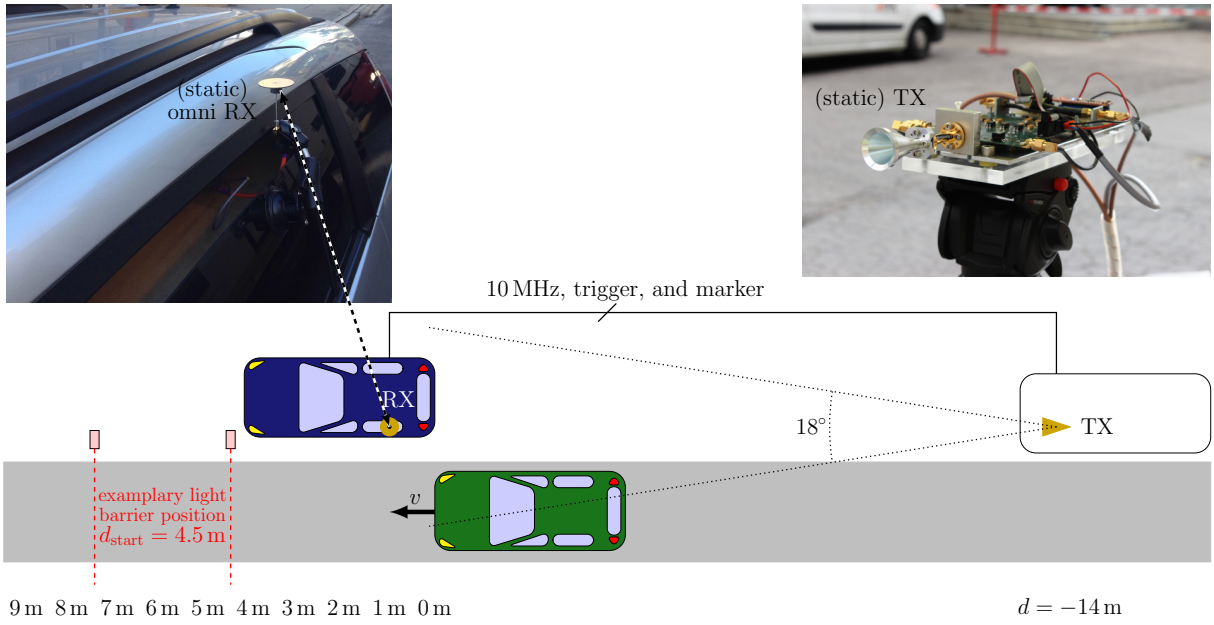

Figure 4.1: ***Bird's-eye view of the measurement site as scaled sketch.*** The TX and RX are static. The overtaking car (green car) is moving relative to the static vehicles at excess speed v. This models a moving car platoon being overtaken by a single vehicle. The overtaking vehicle is sketched at a bumper-to-bumper distance of $d = 0\,\text{m}$.

Figure 4.2: ***Measurement site.*** The TX and RX are static while urban street traffic is passing by. In this snapshot, the overtaking vehicle (white van) is at a bumper-to-bumper distance of approximately $d = 6\,\text{m}$.

the most accurate time and frequency synchronization possible, and it allows for the setup presented in Sec. 2.2.3 to work. Remember that the frequency synchronization is achieved via a 10 MHz reference signal distribution to all clocks. Time synchronization is achieved using a marker signal that triggers the receiver when the sounding signal is transmitted, and a measurement is then triggered once the overtaking vehicle drives through the first light barrier, which is positioned at d_{start}.

The results are then evaluated against the relative position of the overtaking car, short the "distance". The distance d_{start} is measured from the rear bumper of the parked receiver car. Meanwhile, the mean velocity of the overtaking vehicle is estimated through a second light barrier, which is positioned 3 m after the first one. The time Δt it took for the vehicle to arrive at the second light barrier is measured. By means of the mean velocity estimate $\hat{v}$ and the starting point d_{start}, the position of the overtaking vehicle can be estimated at all time points m to

$$\hat{d}[m] = \hat{v} \cdot m\, T_{\text{snap}} + d_{\text{start}} = \frac{3\,\text{m}}{\Delta t}\, m\, T_{\text{snap}} + d_{\text{start}}\ , \tag{4.1}$$

where T_{snap} is the snapshot rate provided in Sec. 2.2.3.

The front bumper of the overtaking vehicle and the rear bumper of the parked receiver car are hence the reference planes, whereas the distance d is referred to as the "bumper-to-bumper distance". The range of interest is marked via meter labels (see the bottom of Fig 4.1).

The memory space at the receiver limits the record time of the 510 MHz broad signal to 720 ms; as such, the recorded measurements do not necessarily cover all the distances of interest. To cover the distances shown in Fig. 4.1, the light barriers that trigger the measurements are placed in three different positions. In other words, d_{start} is varied. Fig. 4.1 illustrates an exemplary light barrier position for covering larger distances.

4.1 Receive Power Fluctuation during Overtaking

The channel sounder provides estimates of the time-variant transfer function $H[m, q]$. The time index is denoted by $m \in \{0, \ldots, S-1\}$ and the frequency index is denoted by $q \in \{0, \ldots, K-1\}$, where $K = 103$. One record of length $T_{\text{rec}} = 720$ ms consists of $S = 5\,579$ snapshots in time. The time-variant CIR $h[m, n]$ with delay index n is obtained via an inverse DFT. Window functions are not applied so that the temporal resolution will not degrade. This will be important for the data evaluation in Section 4.2.

The CIR h exhibits a sparse structure. Therefore, the median of all samples of h is used as the estimator of the noise floor [144]. All values of the CIR below a threshold that is 6 dB above this noise floor are set to zero.

Similar to the approach in [87], the large-scale fading is estimated by applying a moving average filter of length L_{f}. Likewise, it is assumed that the fading process is stationary for a length of $L_{\text{c}} \triangleq 50\,\lambda = 50 \cdot 5\,\text{mm} = 0.25\,\text{m}$. "Corresponds to" is symbolized with $\triangleq$. The filter length L_{f} depends on the velocity of the overtaking vehicles and is always chosen to cover L_{c} and to extend it to the earlier and later time point by $\Delta L = 10$ samples [87]. Hence, it calculates to

$$L_{\text{f}} = L_{\text{c}} + 2\,\Delta L = \left\lfloor \frac{50\lambda}{v \cdot T_{\text{snap}}} \right\rfloor + 2 \cdot 10\ . \tag{4.2}$$

The floor function is indicated via $\lfloor \cdot \rfloor$, and the scenario is dominated by the LOS component. As TX and RX separation is static, this component will always appear at the same delay tap called n_{LOS}. Through Eq. (2.11), the second moment of the LOS tap is estimated, which then enables the strength of the LOS delay tap to be analyzed relative to all taps. This is expressed as

$$\hat{\Omega}^{\text{LOS}}[m] = \text{SA}\left(h[n_{\text{LOS}}, m], L_{\text{f}}\right)\ . \tag{4.3}$$

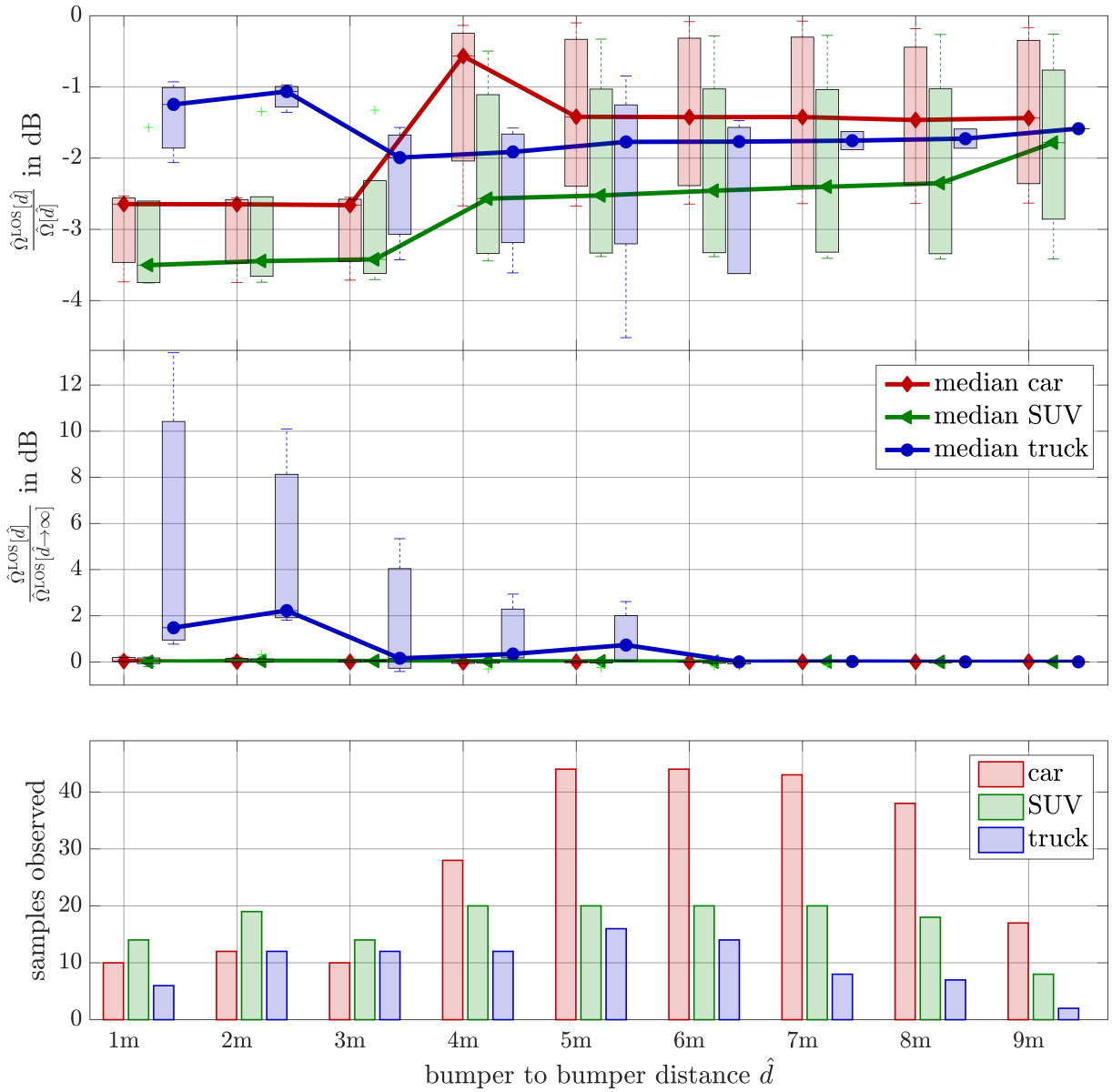

Figure 4.3: ***Statistical evaluation of the LOS power variations.*** (Top) The illustration shows the box plot of the LOS tap gain relative to the gain of all taps. When cars and SUVs are close to the RX antenna ($d = 1$ m), additional MPCs are created, thus decreasing the relative LOS gain. For trucks, the reverse is true because strong reflections add to the LOS tap. (Middle) The LOS tap gains increases when trucks overtake unlike in "no vehicle present". The side walls of the trucks strongly reflect the impinging waves. When cars and SUVs pass by, the LOS tap is hardly affected. (Bottom) This denotes the number of samples used for the evaluation above.

The delay index n_{LOS} is calculated based on the TX – RX distance. The estimate of the time-varying second moment $\hat{\Omega}[m]$ (of all channel taps) is likewise calculated as

$$\hat{\Omega}[m] = \sum_{n=0}^{K-1} \mathrm{SA}\left(h[n,m], L_{\mathrm{f}}\right) . \tag{4.4}$$

Both estimates $\hat{\Omega}^{\mathrm{LOS}}[m]$ and $\hat{\Omega}[m]$ are parametrized by the time index m. All time-dependent quantities are equally well parametrized by the relative position estimate (4.1). With an abuse of notation, for example, $\hat{\Omega}$ is denoted by

$$\hat{\Omega}[d] = \hat{\Omega}\left[\hat{d}^{-1}[d]\right] . \tag{4.5}$$

The experiment was conducted for 30 different vehicles, and the results of which became the basis for the ensemble statistics. The first quantity of interest is the position-specific relative LOS tap gain, that is $\hat{\Omega}^{\mathrm{LOS}}[\hat{d}]/\hat{\Omega}[\hat{d}]$. This quantity is evaluated as a box plot on the top panel of Fig. 4.3.

Remember that the evaluation is based on a window size of $50\,\lambda = 0.25\,\mathrm{m}$ length. For the sake of illustration, the graphs are plotted on a meter-based grid by rounding $\hat{d}$ to the nearest integer meter value. In all of the box plots, the bottom and top edges of the box indicate the 25^{th} and 75^{th} percentiles, while the whiskers show the 5^{th} and 95^{th} percentiles. All observations outside the whiskers are marked with crosses. The bottom panel of Fig. 4.3 shows the number of samples obtained for each meter bin.

Observe that the LOS tap captures most of the channel gain and never drops below $-4\,\mathrm{dB}$. Cars (in red) and sport utility vehicles (SUVs) (in green) in Fig. 4.3 show a similar trend. The relative gains of the LOS tap in both vehicle types increase when the overtaking car is at larger distances d. The additional MPC due to the overtaking vehicle fades out and the limiting value is reached after $d > 5\,\mathrm{m}$.

Trucks show a different trend. If a truck is close to the RX, then the relative gain of the LOS tap increases; but in larger distances, it approaches a lower limiting value. This is intuitively explained by strong MPCs that are generated on the side wall of trucks. Whenever a truck is "close enough", these MPCs are not resolved in the time domain and are binned in the LOS tap.

To further study the abovementioned sidewall reflection effect, the gain increase of the LOS tap against the distance needs to be analyzed. The gain increase relative to "no-vehicle presence" (indicated as $d \to \infty$) is plotted in the middle panel of Fig. 4.3. Cars and SUVs show no effect. In contrast, overtaking trucks can potentially boost the LOS gain by more than $10\,\mathrm{dB}$. The median result shows an increase of approximately $2\,\mathrm{dB}$.

4.2 Small-Scale Fading of the LOS Tap during Overtaking

The section above has discussed that the LOS tap is the dominating factor in the channel gain. Here, the small-scale fading behavior of the LOS tap is analyzed. To suppress large-scale fading effects, the channel is normalized by the square root of the estimated second moment, that is

$$\tilde{h}[m, n_{\mathrm{LOS}}] = \frac{h[m, n_{\mathrm{LOS}}]}{\sqrt{\hat{\Omega}^{\mathrm{LOS}}[m]}}. \tag{4.6}$$

CIRs and estimates of the second moment for an overtaking truck are provided; see Fig. 4.4 for a photograph of the truck and Fig. 4.5 for the LOS channel estimates. Before the small-scale fading statistics can be studied, note that an oscillation with evolving instantaneous frequency is visible in Fig. 4.5. These oscillations of the orange curve with time-varying beating frequency are explained by the change in the Doppler shift as d changes (see Fig. 4.5 for the spectrogram of $|\tilde{h}[m, n_{\mathrm{LOS}}]| - 1$). The Doppler effect of the LOS delay tap proves that this tap consists of at least two contributions, namely, the static unblocked link from TX to RX and at least one reflection from the moving, overtaking vehicle. In

Figure 4.4: ***Webcam snapshot of the exemplary overtaking truck.*** The truck is at approximately $d \approx 5\,\mathrm{m}$ at the time of the snapshot.

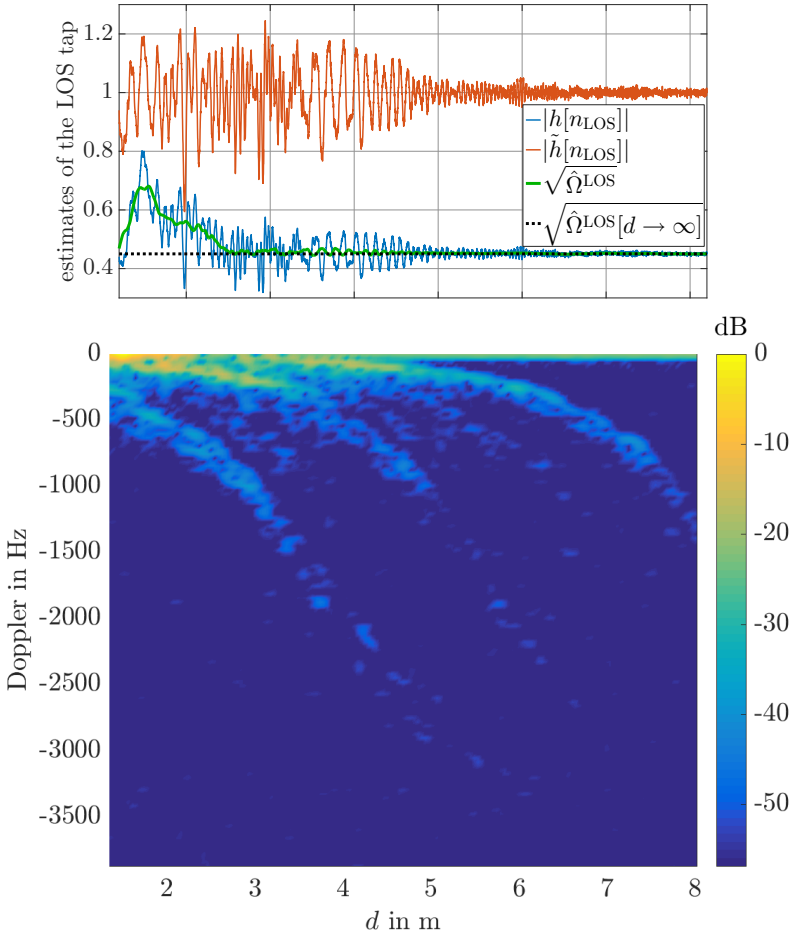

Figure 4.5: ***Result of the post-processing of the LOS tap for the exemplary truck shown in Fig. 4.4.*** (Top) The blue curve shows the LOS channel tap $h[n_{\mathrm{LOS}}]$ including large-scale fading. The green, smooth curve shows the estimated large-scale fading $\sqrt{\hat{\Omega}^{\mathrm{LOS}}}$. The black dashed line is the estimate of the channel gain without a vehicle present. The orange curve shows the normalized LOS channel tap $\tilde{h}[n_{\mathrm{LOS}}]$, that is, the small-scale fading only. The oscillatory behavior stops at approximately $5\,\mathrm{m}$. (Bottom) Spectrogram of the normalized LOS channel tap ($|\tilde{h}[n_{\mathrm{LOS}}]| - 1$). The oscillatory behavior is best explained by the two strong, yellow traces in the spectrogram.

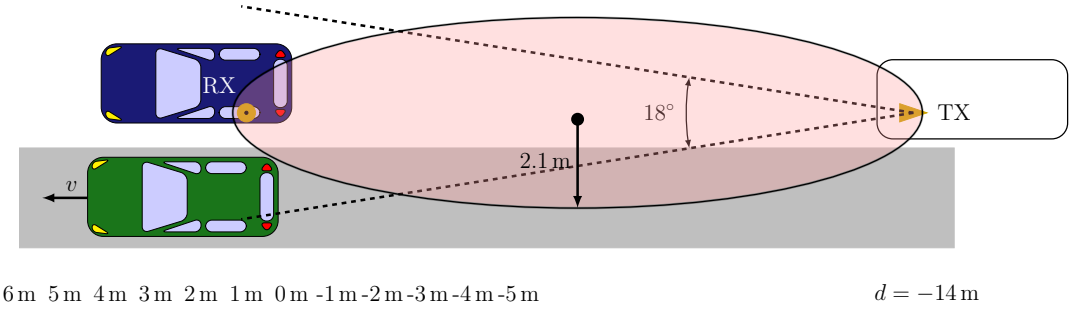

Figure 4.6: ***Scaled sketch of the bandwidth ellipse.*** The LOS tap fades if another object is within the pink-filled ellipse (semi-minor axis equals 2.1 m). The green car in this figure is sketched such that it just produces TWDP fading. If the car goes further on, then its reflection will be at the next channel tap.

the spectrogram, there are many other smaller traces visible in light blue. These traces are approximately 40 dB weaker than the dominiating MPCs. Based on the results in Sec. 2.1.3, these MPCs are considered as diffuse components. The spectrogram uses a Kaiser window with 256 samples length and shape parameter $\alpha = 5$. The Kaiser window approximates the discrete prolate spheroidal (DPS) sequence window [145, p. 232 ff.], which will be later extensively used for the Doppler analysis in Section 4.3.

Remember that the TWDP small-scale fading model assumes fading due to the interference of two strong radio signals and numerous smaller, so-called diffuse signals. In the studied case, the two strong radio signals are the unblocked LOS and the reflection from an overtaking vehicle, which arrive at the same delay tap. The measurement bandwidth of BW $= 510$ MHz allows resolving the MPCs that are separated by a delay of $\Delta\tau \approx 1/\mathrm{BW} \approx 2$ ns or a travel distance of $\Delta s \approx c_0/\mathrm{BW} \approx 60$ cm. Every MPC that is separated at less than these values is not resolved, and are thus interpreted as fading. The Fresnel ellipsoids for the MPCs arriving at the same time tap (bin) as the component corresponding to LOS is given by

$$|\tau_{\mathrm{LOS}} - \tau_{\mathrm{refl}}| \leq \frac{1}{\mathrm{BW}}. \tag{4.7}$$

In Fig. 4.6, this ellipse is shown in pink. The green car in Fig. 4.6 shows the maximum distance values (≈ 4.5 m) that an overtaking car produces TWDP fading. Figure 4.6 also shows the half-power beamwidth of the TX horn. This illustrates that the distance region $-4 \ldots 4$ m leads to a reflection that is not much weaker than the LOS component. Hence, two specular MPCs at the same order of magnitude are expected. In the region from, $-14 \ldots -5$ m the ellipsoid condition to experience TWDP fading is fulfilled, but spatial filtering by the horn antenna suppresses the reflected component. By inspecting Fig. 4.5 again, one can observe that the oscillatory behavior fades out after 5 m, as the overtaking truck is a rather short one.

4.2.1 Statistical Analysis Based on AIC

The approach presented in Sec. 2.1.2 is applied to the filtered envelope measurement data of the LOS delay, that is, $r[m] = \left|\tilde{h}[m, n_{\mathrm{LOS}}]\right|$. The maximum likelihood estimation (MLE) of the parameter tuple ($\hat{K}[m]$,$\hat{\Delta}[m]$) takes all samples within the assumed stationary length of $L_{\mathrm{c}} \triangleq 50\lambda$. MLE is also performed for the Rician K-factor ($\Delta \equiv 0$). Taking the data of the exemplary truck (Fig. 4.4 and Fig. 4.5), the estimated CDFs and their evolution is shown in Fig. 4.7.

The three smallest distances (in Fig. 4.7) show the CDFs where the truck is near the receive antenna. The fading that occurs is not well explained by a Rician fit, while the proposed TWDP fading model shows a superior fit. Only in the last example at a distance of 6 m does it clearly fade according to a Rice distribution. It has been mentioned earlier that TWDP fits must always be better than Rician fits since the Rician model is a special case of TWDP. However, the TWDP model introduces an additional parameter, which is generally not desirable. Thus, to select between Rician fading and TWDP fading,

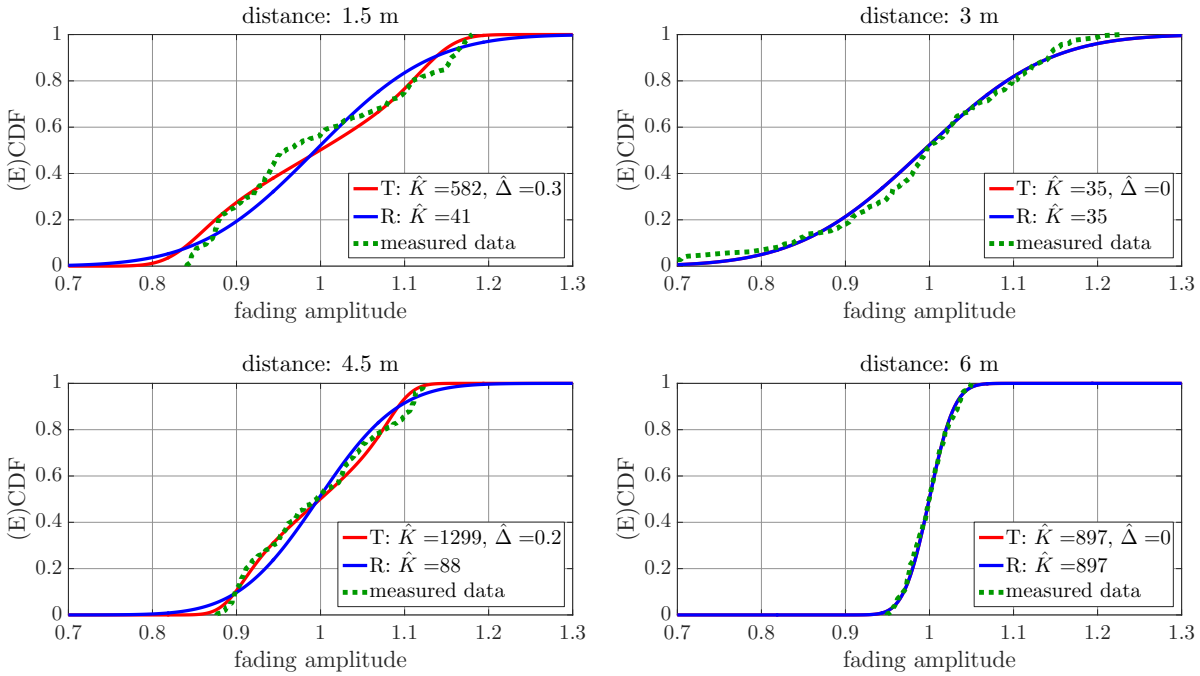

Figure 4.7: ***CDF evolution over distance.*** Again, the data used in this figure is from the example given in Fig. 4.4 and Fig. 4.5. For distances smaller than 5 m, TWDP fading leads to a superior fit. At first glance, the Rician model also seems to achieve a good fit, however, the K-factors of both models are not in the same order of magnitude. Rician fading underestimates the power in the specular components.

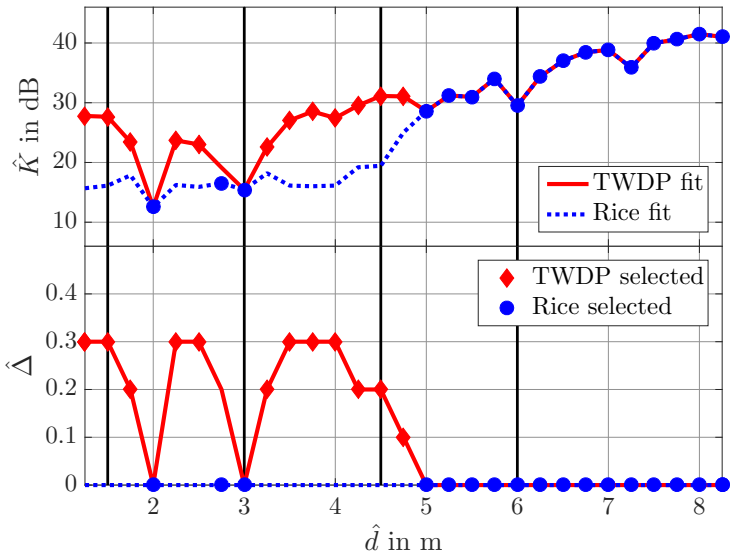

Figure 4.8: ***MLE fitted parameter tuple*** $(\hat{K}, \hat{D})$ ***for the exemplary truck channel from Fig. 4.5*** The Rician K-factor (blue dashed line) underestimates the power within the specular components. If the AIC selects TWDP fading, then a red diamond would mark the parameter tuple. If Rician fading is selected, then a blue circle would be used. The black vertical lines illustrate the positions evaluated in Fig. 4.7.

AIC is employed (see Sec. 2.1.2). For the exemplary truck, the fitted parameters and the selected model are shown in Fig. 4.8. Now, the ensemble statistics of small-scale fading is shown Fig. 4.9. Depending on the selected model, either the TWDP K-factor or the Rician K-factor is taken for the statistics. For Rician fits, Δ is set to zero ($\Delta \equiv 0$). However, note that meaningful results are obtained only when the model selection algorithm succeeds. In particular, at very small Δ-parameters, the AIC would very likely decide in favor of Rician fading, and hence would bias the resulting Δ-parameters toward smaller values as previously discussed in Sec. 2.1.3. The K-factor is smaller if the vehicle is closer to the RX antenna (closer to the rear bumper of the car). If the vehicle passes the static RX car, the K-factor saturates at higher values. This means that the LOS tap does not fade any longer. As mentioned above, the vehicle size is translated to the distance d. In case of longer vehicles such as trucks, it takes longer for the K-factor to start increasing. SUVs place in between cars and trucks. Next, the Δ-parameter is in focus. The length of the vehicle also affects this parameter. TWDP fading occurs, that is, $\Delta > 0$, whenever a part of the vehicle is still close to the RX antenna. The longer the vehicle, the longer this effect is visible. Remember that the median Δ value has a slightly negative bias; it is set to zero if the AIC decides in favor of Rician fading. This explains why the SUV median is zero at 2 m, although the Δ values are spread out; in case of SUVs, AIC decides for Rician fading more than half of the time.

The AIC model selection decisions are color-coded in the histogram in the bottom panel of Fig. 4.9. The histogram in lighter shades is identical to the histogram of Figure 4.3. The darker shades show the number of samples where AIC decided for TWDP fading. Again, looking at the maximum distances where TWDP fading occurs, the correlation with the vehicle length is visible.

4.2.2 A Simplified Model for the Parameter Evolution

The previous subsection has already established that the length of the vehicle affects the tuple parameters (K, Δ). In order to quantify this influence, and the show how the (K, Δ) tuple evolves, a simple model is now presented. First of all, note that the data consist only of the TWDP fits now, and model selection is not applied here. Furthermore, this subsection also uses data at negative distances. These were not considered initially because there are no data at these distances for trucks. However, the measured data show a symmetry around $d = 0$.

A passing vehicle has an effect such that the parameter tuple changes and saturates as the distance increases; and due to the spatial extend of the vehicle, a smooth transition can be expected. Analogous to the previous section, the K-factor that appears without a vehicle present is denoted as $K_{d\to\infty}$. This constant is chosen to be $K_{d\to\infty} = 46\,\text{dB}$ since these were the highest observed values. The K-factor change is modeled through the first-order linear differential equation

$$\frac{\partial K(d)}{\partial d} = \frac{\big(K_{d\to\infty} - K(d)\big)}{\delta}, \qquad K(0) = (1-\kappa)\, K_{d\to\infty}\,. \tag{4.8}$$

The parameter δ acts as effective length of the overtaking vehicle. The larger δ is, the slower the change of K would be. Furthermore, if there is a large deviation from $K_{d\to\infty}$, a vehicle is very close to the RX antenna and will be soon farther away. Hence, the K-factor should be able to change faster. The solution to incorporate symmetry around $d = 0$ is given by

$$K(d) = K_{d\to\infty}\left(1 - \kappa \exp\left(-\frac{|d|}{\delta}\right)\right). \tag{4.9}$$

The factor κ models the maximum reduction of the K-factor when a vehicle is present. Likewise, the Δ-parameter is modeled to fulfil

$$\frac{\partial \Delta(d)}{\partial d} = -\frac{\Delta(d)}{\delta}, \qquad \Delta(0) = \Delta_{\text{max}}\,. \tag{4.10}$$

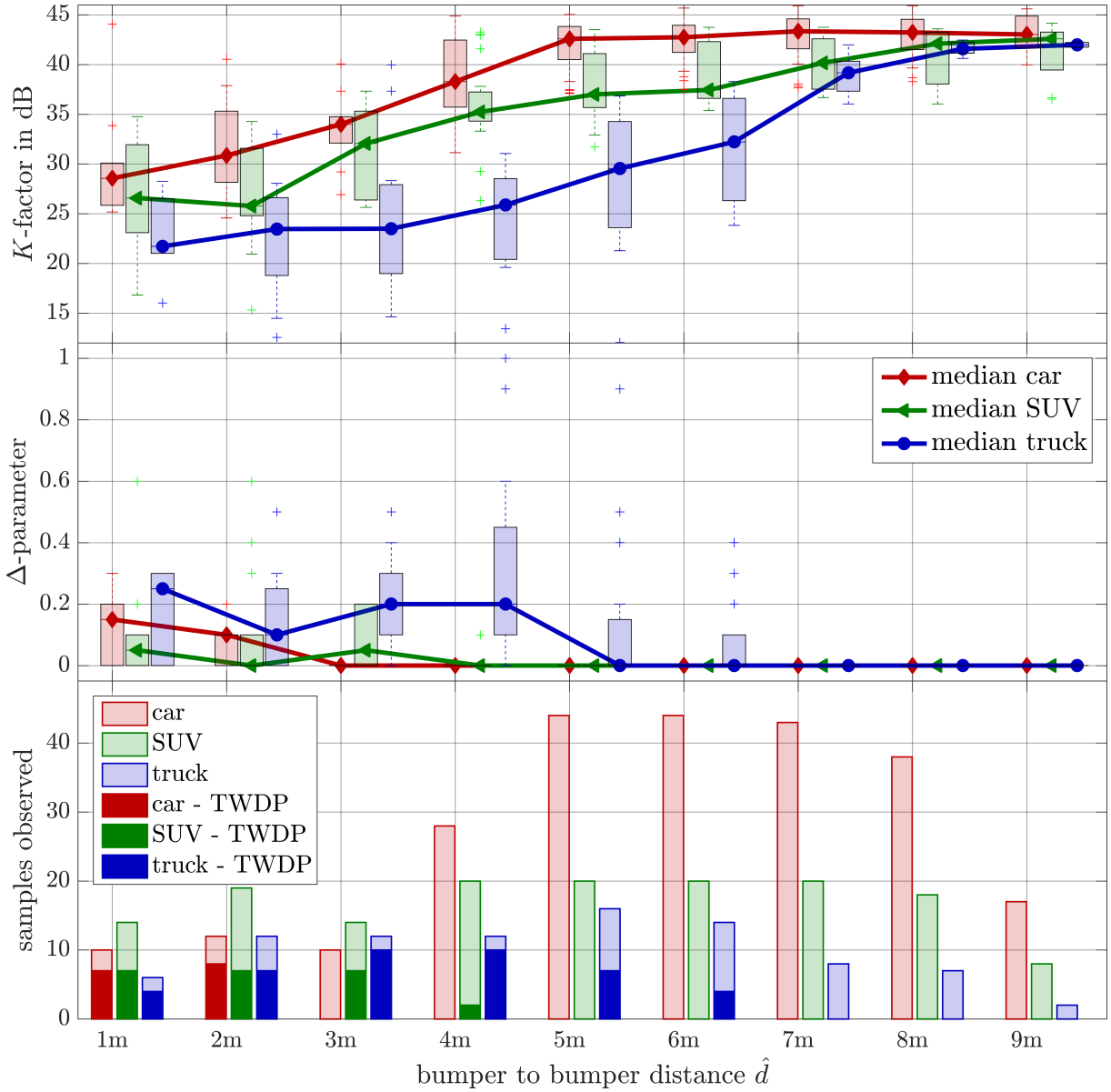

Figure 4.9: ***ML fitted*** (K, Δ) ***parameters and model statistic.*** (Top) This presents the box plots of the Rician fading and TWDP fading K-factor. The closer the vehicle to the RX and the larger the vehicle is, the stronger the diffuse components would be. (Middle) The panel shows the box plots of the Δ-parameter. The larger the vehicle is, the stronger the second specular component would be. For example, $\Delta = 0.2$ (for trucks) corresponds to a second specular component that is 20 dB smaller than the LOS component, see Fig. 2.3. (Bottom) This shows the histogram of all samples observed, and the TWDP selection ratio.

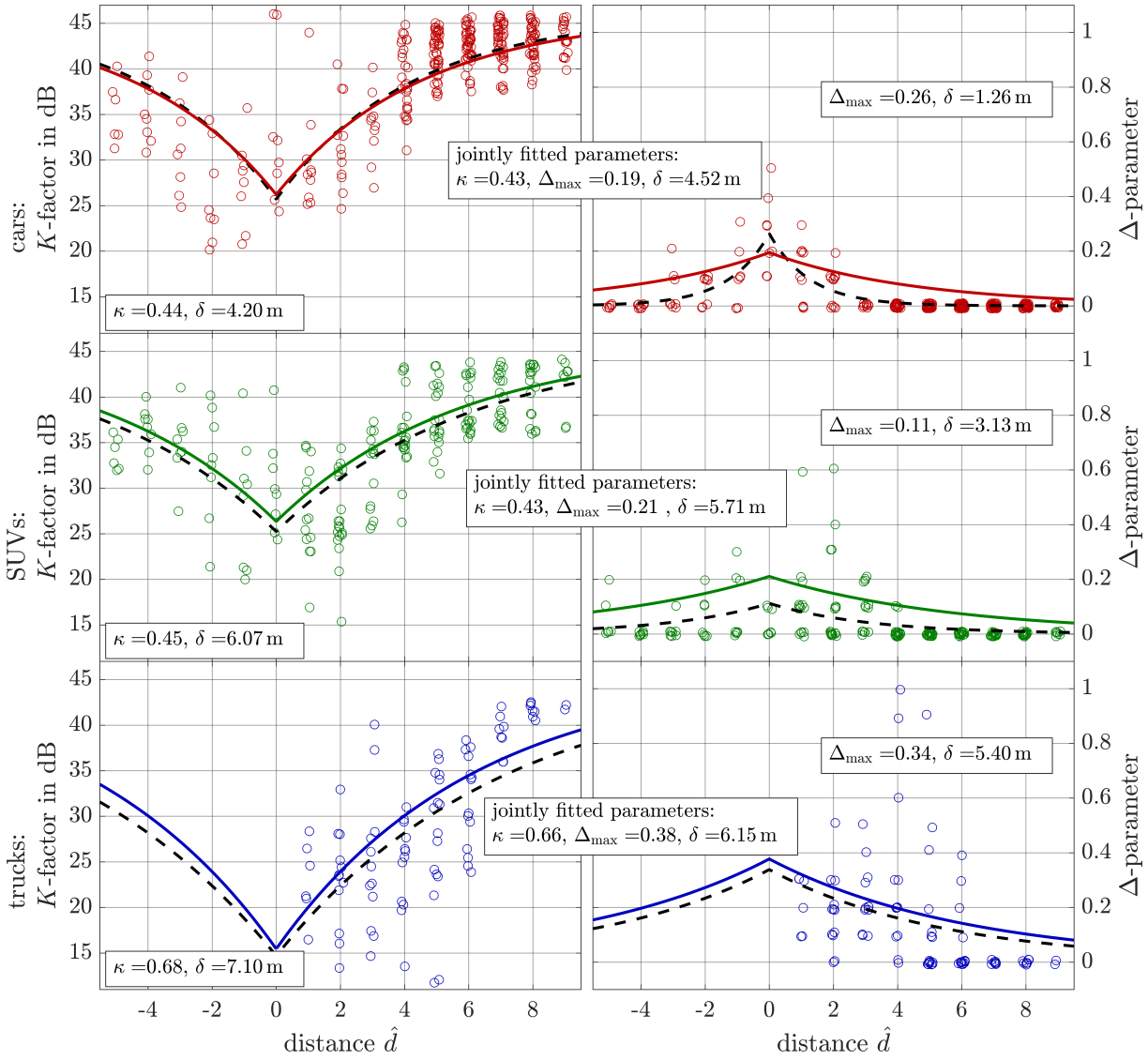

Figure 4.10: ***Effective vehicle length estimation through exponential modeling of the parameter tuple.*** (Left) The fitted K-factors for cars, SUVs, and trucks are shown from top to bottom. (Right) The fitted Δ-parameters for cars, SUVs, and trucks are also shown from top to bottom. The effective distances range from $\delta \in (1.26\,\text{m}, 7.1\,\text{m})$. The effective length δ scales with the vehicle length.

Again, the solution is a symmetric exponential function

$$\Delta(d) = \Delta_{\max} \exp\left(-\frac{|d|}{\delta}\right), \tag{4.11}$$

where $\Delta_{\max}$ models the strongest reflection from the overtaking vehicle. The δ-parameter has the same meaning as that for the K-factor, although it is allowed to deviate when Δ and K are fitted individually.

For the individual fit of the K-factor and the Δ-parameter models, MATLAB's nonlinear least-square fitting tool was utilized. The least squares fit of the parameters is plotted in Fig. 4.10 with black, dashed lines. The fitted parameter values are plotted in the corresponding panels as well. The individually fitted model parameters are annotated in the lower left corner of the K-factor panels and in the upper right corner of the Δ-parameter panels. In the case of the K-factor, the effective length is between $4.2\,\mathrm{m}$ and $7.1\,\mathrm{m}$. The values for the Δ-parameter are smaller and range from 1.3 to $5.4\,\mathrm{m}$. The maximum reduction of the K-factor is between 44% and 68% and the maximum Δ-parameters fall between 0.11 and 0.34.

For the joint fit of (K, Δ), we employ the following strategy. Firstly, we linearize the ansatz functions (4.8) and (4.11) via a natural logarithm transform. We thereby achieve the following equations

$$\begin{aligned} \log\left(1 - \frac{K(d)}{K_{d\to\infty}}\right) &= \log\kappa \quad - \frac{1}{\delta}|d| \\ \log\Delta(d) &= \log\Delta_{\max} \quad - \frac{1}{\delta}|d| \end{aligned}. \tag{4.12}$$

Through stacking all equations from the first distance d_1 until the last distance d_N, we achieve the following matrix-vector equation

$$\begin{bmatrix} \log\left(1 - \frac{K(d_1)}{K_{d\to\infty}}\right) \\ \vdots \\ \log\left(1 - \frac{K(d_N)}{K_{d\to\infty}}\right) \\ \hdashline \log\Delta(d_1) \\ \vdots \\ \log\Delta(d_N) \end{bmatrix} = \left[\begin{array}{ccc} 1 & 0 & -|d_1| \\ \vdots & \vdots & \vdots \\ 1 & 0 & -|d_N| \\ \hdashline 0 & 1 & -|d_1| \\ \vdots & \vdots & \vdots \\ 0 & 1 & -|d_N| \end{array}\right] \begin{bmatrix} \log\kappa \\ \log\Delta_{\max} \\ \frac{1}{\delta} \end{bmatrix}. \tag{4.13}$$

By applying the Moore-Penrose inverse to (4.13), the solution parameters are found.

The joint parameter fit avoids the ambiguous δ-parameter, as this parameter is common for the parameter tuple. This approach, however, comes with the disadvantage that some observations need to be withdrawn from the data set, as values close to 0 are problematic in the logarithm term of the left-hand side in (4.13). In this contribution, we skip those observations with the logarithm argument smaller than 0.1 . Thereby we withdraw almost all samples of Δ at larger distances. This leads to a inferior fit of Δ.

The joint least-squares fit of the parameters is plotted in Fig. 4.10 as solid lines. The fitted model parameters are plotted across the corresponding panels. The effective length is between $4.52\,\mathrm{m}$ and $6.15\,\mathrm{m}$, and hence matches fairly well the vehicle lengths.

4.3 Delay-Doppler Dispersion Evaluated via the Local Scattering Function

The channel is characterized in this section through the LSF in order to analyze the delay-Doppler dispersion of the measured vehicular channel [87, 146, 147]. Similar to the previous sections, the fading

process is assumed to be locally stationary within a region of M samples in time and within all samples in the frequency domain. The LSF is estimated for consecutive stationarity regions in time. The multitaper-based estimator averages multiple independent spectral estimates from the same measurement. The estimate of the LSF is then defined as [146]

$$\hat{\mathcal{C}}[k_t; n, p] = \frac{1}{IJ} \sum_{w=0}^{IJ-1} \left| \mathcal{H}^{(G_w)}[k_t; n, p] \right|^2 . \tag{4.14}$$

The Doppler index is denoted by $p \in \{-K/2, \ldots, K/2\}$, while the delay index is denote by $n \in \{0, \ldots, M-1\}$ as in the previous sections. The delay and Doppler shift resolutions are given by $\tau_s = 1/(K\Delta f)$ and $\nu_s = 1/(MT_{\text{snap}})$, whereas the time index of each stationarity region is $k_t \in \{0, \ldots, \lfloor S/M - 1 \rfloor\}$ and corresponds to the center of the stationarity regions. The windowed frequency response $\mathcal{H}^{(G_w)}$ is calculated by

$$\mathcal{H}^{(G_w)}[k_t; n, p] = \sum_{m=-M/2}^{M/2-1} \sum_{q=-K/2}^{K/2} H[m + Mk_t, q]\, G_w[m, q]\, \mathrm{e}^{-\mathrm{j}2\pi(pm-nq)} , \tag{4.15}$$

where the tapers $G_w[m, q]$ are the DPS sequences [148]. This is explained in more detail in [146]. The number of tapers in time domain is $I = 3$, while the number of tapers in the frequency domain is $J = 3$.

A number of $M = 233$ corresponds to a stationarity region of $30\,\text{ms}$ in time. The power delay profile (PDP) and the Doppler spectral density (DSD) are calculated as a summation (marginalization) of the LSF over the Doppler domain or delay domain [146],

$$\text{PDP}[k_t; n] = \sum_{p=-M/2}^{M/2-1} \hat{\mathcal{C}}[k_t; n, p] , \qquad \text{DSD}[k_t; p] = \sum_{n=0}^{K-1} \hat{\mathcal{C}}[k_t; n, p] . \tag{4.16}$$

The two textbook parameters of time-varying root mean square (RMS) delay spread and of RMS Doppler spread are then analyzed based on the PDP and DSD. To obtain these quantities, Eqs. (10) – (13) from [146] are used in this study.

The measurements were conducted in a street that has a speed limit of $30\,\text{km/h}$. Although the average vehicle speed is in this order, some vehicles significantly deviate from the average speed. To compare vehicles at different speeds, the Doppler profile of each vehicle is first normalized with respect to its maximum Doppler shift

$$\nu_{\text{max}} = \frac{2\hat{v}}{\lambda} . \tag{4.17}$$

Next, the Doppler profile is rescaled to a common speed of $v = 30\,\text{km/h} \approx 8.33\,\text{m/s}$. Fig. 4.11 shows the data post-processing of the exemplary truck. Figure 4.11(a) shows the PDP as it evolves over distance. A bandwidth of $510\,\text{MHz}$ is not sufficient to distinguish the MPCs in the time domain. A small channel gain increase in the delay range $10\,\text{ns}$ to $30\,\text{ns}$ is visible after approximately $5\,\text{m}$. Meanwhile, Fig. 4.11(b) shows the respective RMS spread values. Lastly, Fig. 4.11(c) presents the corresponding DSD, in which the additional MPCs from the overtaking truck are clearly visible as negative Doppler shift traces. Note that these traces are already partially demonstrated in Fig. 4.5. The results for the whole data ensemble are illustrated in Fig. 4.12. The bottom panel shows again the number of samples used to evaluate at each individual position. Note that the histogram is slightly different from the previous ones. Previously, the evaluation was performed on 50λ in space, which equals to $30\,\text{ms}$ evaluation time only for a vehicle speed of $v \approx 8.25\,\text{m/s} = 29.7\,\text{km/h}$.

The RMS delay spread (top panel of Fig. 4.12) is only slightly affected by an overtaking vehicle. If a truck is close to the RX antenna (at approximately $1\,\text{m}$ to $2\,\text{m}$), then it shadows the background, boosts the already-dominating LOS delay, and gives the smallest σ_τ. Cars and SUVs barely alter σ_τ. Both

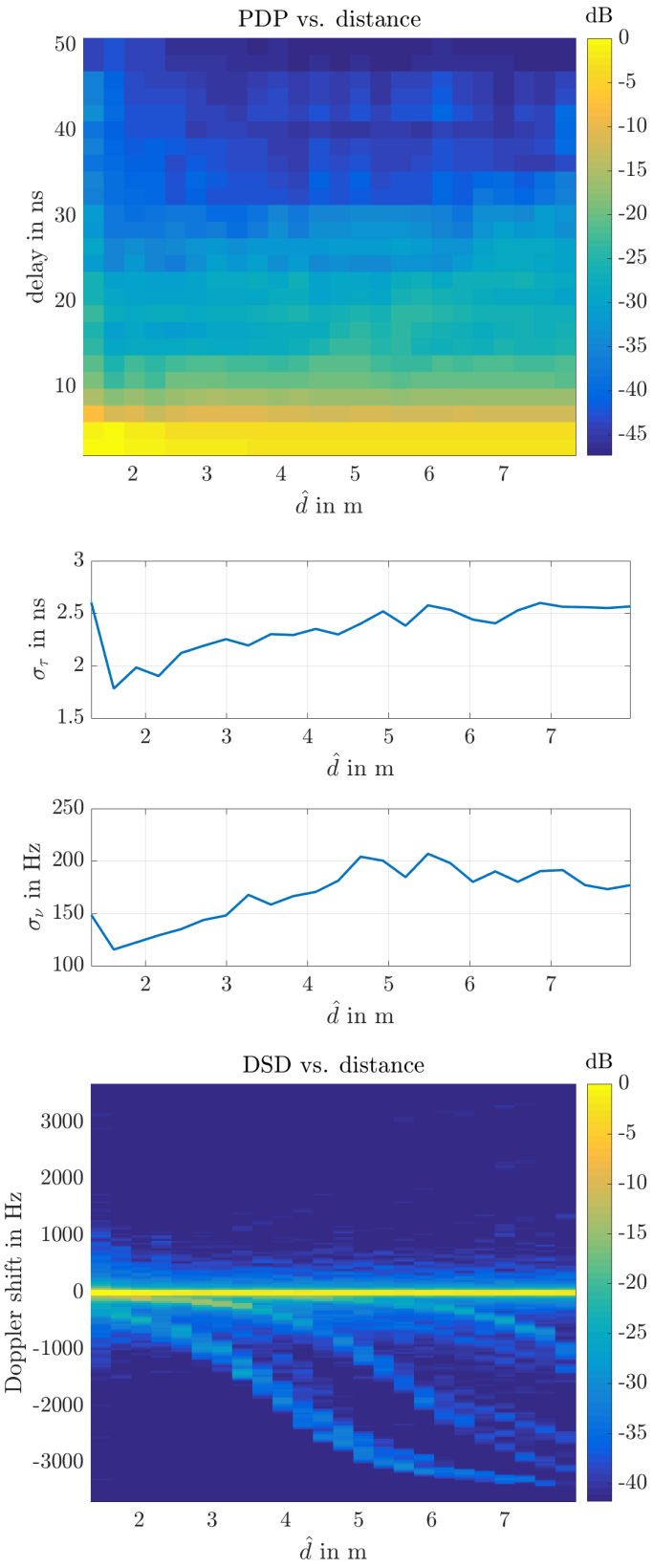

Figure 4.11: ***Post-processing steps to obtain the RMS delay spread and RMS Doppler spread.*** (Top) The panel shows the time-aligned PDP of the exemplary truck, in which the time resolution obtained with 510 MHz bandwidth is not sufficient to resolve strong MPCs. (Middle) This is the estimated RMS delay spread and estimated RMS Doppler spread calculated on a 30 ms time grid. (Bottom) The panel shows the DSD of the exemplary truck. The MPCs reflected on the truck are clearly visible via their Doppler shifts.

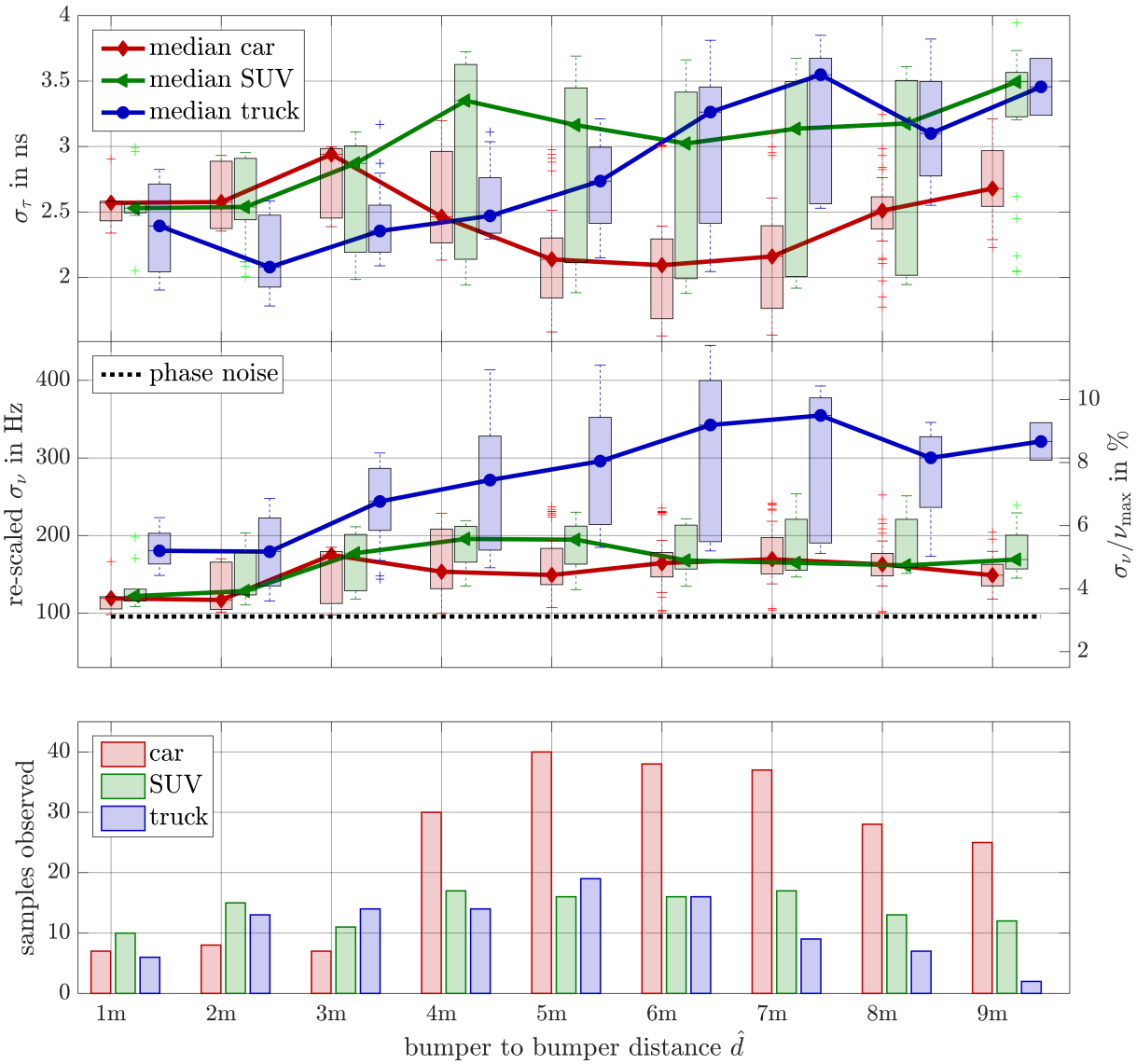

Figure 4.12: ***Data evaluation based on the LSF.*** (Top) The box plots shows the RMS delay spread as a function of the bumper-to-bumper distance. The position of the overtaking vehicle does not significantly affect the RMS delay spread. (Middle) This shows the RMS Doppler spread rescaled to a common vehicle speed of 30 $^{\text{km}}/_{\text{h}}$ on the left axis. The RMS Doppler spread, which is normalized to the maximum Doppler shift, is labeled on the right axis. The black dotted line shows the estimate for the RMS Doppler spread, which is obtained through the phase noise of the measurement system used in this thesis. The RMS Doppler spreads of cars and SUVs are only twice as much as the values obtained due to phase noise. In a system without "perfect" frequency synchronization or worse reference clocks, the increase might not be visible. (Bottom) The panel shows the number of samples used for the evaluation above based on 30 ms sample lengths.

vehicle types have the median swings of less than 1 ns. Generally, all of the RMS delay spread values of different vehicles are in the same order. The RMS Doppler spread of cars and SUVs at distances close to the antenna (< 3 m) is mainly due to phase noise of the equipment used in this study. The phase noise values are determined through applying the LSF on the positive Doppler frequencies. Accordingly, these Doppler frequencies do not occur at positive distances ($d > 0$ m), and only occurs due due to phase noise.

Cars show the strongest effect on σ_ν at approximately 3 m to 4 m, while SUVs show their maximum effect a bit later at around 4 m to 5 m. At larger distances, the MPC of the overtaking car (SUV) fades out. Note the similarity in the σ_ν of cars and that of SUVs after 6 m. In this region, only the rear parts of the vehicles are illuminated. Trucks produce an RMS Doppler spread that is twice as strong as those of cars and of SUVs. Again, due to trucks' larger extent, the maximum RMS Doppler spread occurs later at approximately 7 m.

Keep in mind, however, that due to the spatial filtering of the horn antenna combined with strong LOS, the RMS Doppler spread is less than 12% of the maximum Doppler shift ($\sigma_\nu \leq 0.12\,\nu_{\max}$). In the median case, σ_ν is even below one-tenth of the maximum Doppler shift $\nu_{\max}$. For comparison, a Doppler shift uniformly distributed in $(-\nu_{\max}, 0)$ yields

$$\sigma_\nu^2 = \int_{-\nu_{\max}}^{0} \frac{1}{\nu_{\max}} \nu^2 \mathrm{d}\nu - \bar{\nu}^2 = \frac{\nu_{\max}^2}{12} \quad \Rightarrow \quad \boxed{\frac{\sigma_\nu}{\nu_{\max}} = \frac{1}{\sqrt{12}} = \frac{1}{2\sqrt{3}} \approx 0.2887}\,, \tag{4.18}$$

A Doppler shifted according to a Jakes' spectrum ($P(\nu) = \frac{1}{\pi\sqrt{\nu_{\max}^2 - \nu^2}}$) yields as much as

$$\sigma_\nu^2 = \frac{1}{\pi\nu_{\max}} \int_{-\nu_{\max}}^{\nu_{\max}} \frac{1}{\sqrt{1 - \left(\frac{\nu}{\nu_{\max}}\right)^2}} \nu^2 \mathrm{d}\nu = \frac{\nu_{\max}^2}{2} \quad \Rightarrow \quad \boxed{\frac{\sigma_\nu}{\nu_{\max}} = \frac{1}{\sqrt{2}} \approx 0.7071}\,. \tag{4.19}$$

Even setting the positive Jakes' frequencies to zero (half-Jakes) still yields

$$\sigma_\nu^2 = \frac{\nu_{\max}^2}{4} - \bar{\nu}^2 = \nu_{\max}^2 \frac{\pi^2 - 2^2}{(2\pi)^2} \quad \Rightarrow \quad \boxed{\frac{\sigma_\nu}{\nu_{\max}} = \sqrt{\frac{\pi^2 - 2^2}{(2\pi)^2}} \approx 0.3856}\,. \tag{4.20}$$

The mean shift $\bar{\nu}$ is then given by

$$\bar{\nu} = \frac{1}{\pi\nu_{\max}} \int_{-\nu_{\max}}^{\nu_{\max}} \frac{1}{\sqrt{1 - \left(\frac{\nu}{\nu_{\max}}\right)^2}} \nu \mathrm{d}\nu = -\frac{\nu_{\max}}{\pi}\,. \tag{4.21}$$

Hence, modeling σ_ν with the above mentioned models is not appropriate.

5 Simulation Studies

The first study on the two-ray model using the ray-tracing data has been published in

- Erich Zöchmann, Ke Guan, and Markus Rupp. "Two-Ray Models in mmWave Communications". In: *Proc. of IEEE 18th International Workshop on Signal Processing Advances in Wireless Communications (SPAWC)*. 2017

A more detailed analysis has been published in

- Erich Zöchmann et al. "Parsimonious Channel Models for Millimeter Wave Railway Communications". In: *Proc. of IEEE Wireless Communications and Networking Conference*. 2019

The link-level simulations are based on a framework developed in

- Erich Zöchmann et al. "Exploring the Physical Layer Frontiers of Cellular Uplink". In: *EURASIP Journal on Wireless Communications and Networking* 2016.1 (2016)

Up to this point, the focus of this study has been measurement data. This chapter then focuses on a ray-tracing study such that the findings of this thesis will not be limited to measurement data. The ray-tracing data are obtained from an independent, third source [96]. The presented methodology in Chapter 2 is then applied on the ray-tracing data set. The ray-tracing study discussed in this chapter deals with railway communications, and beamforming is essentially limited to the elevation domain. This restriction allows for a model that is solely based on the geometry and for the antenna patterns to be presented. Lastly, link-level simulations assess the impact of TWDP fading on the transmission quality.

5.1 Railway Communications Ray-Tracing Study

The two-ray (ground reflection) model has been widely used in wireless communications systems as a model for the path loss coefficient. Nevertheless, the two-ray model is a small-scale fading model since it describes an interference pattern of two waves. Analogous to [10], the description in the delay domain supports the author's arguments. The analyzed scenario, leading to a two-ray model, is depicted in Fig. 5.1.

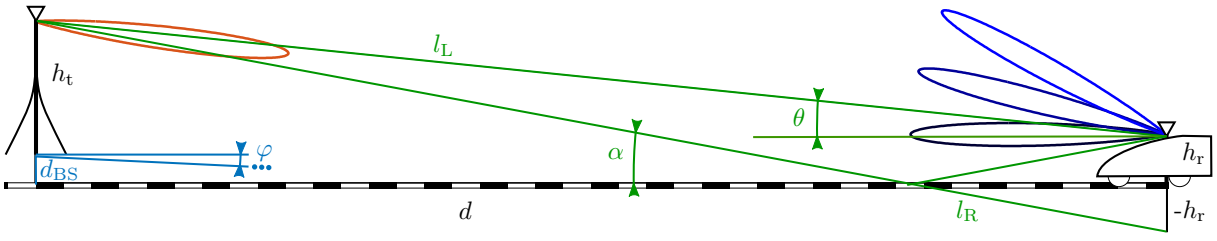

Figure 5.1: ***A sketch of the analyzed scenario.*** The analysis focuses on train-to-infrastructure communications, in which the base station uses a directive antenna with static alignment. Only the approaching train adapts the beam direction in elevation θ and azimuth φ. The base station is $d_\mathrm{BS} = 10\,\mathrm{m}$ away from the train tracks, and points its beam to the tracks at $d = 500\,\mathrm{m}$. All throughout the paper, it will be approximated that $l_\mathrm{L} \approx l_\mathrm{R} \approx d$. The base station height is $h_\mathrm{t} = 10\,\mathrm{m}$ and the antenna on the train is mounted at a height of $h_\mathrm{r} = 3\,\mathrm{m}$. The antennas have $25\,\mathrm{dBi}$ gain. The setup is detailed further in [96].

5.1.1 Time-Domain Description of the Two-Ray Model

The channel impulse response of the two-ray model reads

$$h(d,\tau) = a(d)\big(\delta(\tau) + g(d)e^{\mathrm{j}\phi(d)}\delta(\tau - \tau_0(d))\big)\,, \tag{5.1}$$

where a subsumes the free space attenuation of the LOS path of length l_{L} and the distance-dependent antenna gains of the transmitter $G_{\mathrm{L}}^{\mathrm{TX}}$ and receiver $G_{\mathrm{L}}^{\mathrm{RX}}$, respectively. With the notation $G_{\mathrm{L}}^{\mathrm{TX}}(d)$, it is stressed that the antenna gains for a given geometry and beamforming strategy (fixed beamforming or dynamic beamforming) depend only on the distance d. In other words, given the alignments and the height of the antennas, the elevation and the azimuth angle of the transmitted and received waves are implicitly given. Subscript L or R reflects whether the focus is set on the LOS component or on the reflected one. For distances $d \gg h_{\mathrm{t}}, h_{\mathrm{r}}$ that is much longer than the transmitter and receiver height, factor a is commonly approximated to

$$a(d,f) \approx \frac{{}^{c_0}\!/_{f}\sqrt{G_{\mathrm{L}}^{\mathrm{TX}}(d)G_{\mathrm{L}}^{\mathrm{RX}}(d)}}{4\pi d}\,. \tag{5.2}$$

Despite the large bandwidths of mmWave systems, the relative bandwidth is mostly below 5%, and thus allows the frequency dependency of a to be dropped through fixing the wavelength λ to the center frequency. The second, reflected, and delayed component has an analogous (complex) path attenuation of

$$a_{\mathrm{R}}(d) \approx \frac{\lambda\sqrt{G_{\mathrm{R}}^{\mathrm{TX}}(d)G_{\mathrm{R}}^{\mathrm{RX}}(d)}}{4\pi d}e^{\mathrm{j}\phi(d)} = a(d)g(d)e^{\mathrm{j}\phi(d)}\,, \tag{5.3}$$

where ϕ is the phase change due to reflection. The gain of the LOS component is factored out and the reflected component is described by the relative loss function

$$g(d) = \sqrt{\frac{G_{\mathrm{R}}^{\mathrm{TX}}(d)G_{\mathrm{R}}^{\mathrm{RX}}(d)}{G_{\mathrm{L}}^{\mathrm{TX}}(d)G_{\mathrm{L}}^{\mathrm{RX}}(d)}}\,. \tag{5.4}$$

Again, assuming a relatively long ground distance d, the delay of the reflected component is approximated to [149]

$$\tau_0(d) = \frac{\Delta l}{c} = \frac{2h_{\mathrm{t}}h_{\mathrm{r}}}{d}\frac{1}{c}\,. \tag{5.5}$$

If a system bandwidth that can resolve the delay τ_0 in Eq. (5.5) is used, then the system could collect the energy of both rays through a multipath receiver, for example, a rake receiver. As such, the receive power falls off exponentially with distance. A narrowband receiver cannot resolve both rays and simply add them up. Depending on the delay (phase) of both paths, the receive filter convolution would cause an interference pattern.

5.1.2 Frequency-Domain Description of the Two-Ray Model

The previous subsection has mentioned that depending on the bandwidth, a system (1) is capable of resolving both paths, and thus no fading will occur; or (2) does not have enough time resolution, and thus fading will occur. To analyze the strength of the fading process, the mean power (*large-scale fading*) and envelope formulas for constructive interference and for destructive interference (*small-scale fading*) are derived from the frequency domain description. In the following derivations, the function arguments (braces) are dropped to achieve compact equations.

The Fourier transform $\mathcal{F}\{\cdot\}$ of Eq. (5.1) reads

$$\mathcal{F}\{h(d,\tau)\} = H(d,f) = ae^{-\mathrm{j}\pi f\tau_0+\frac{\phi}{2}}\left(2g\cos\left(\pi f\tau_0+\frac{\phi}{2}\right)+(1-g)e^{-\mathrm{j}\left(\pi f\tau_0+\frac{\phi}{2}\right)}\right). \tag{5.6}$$

The power spectrum is hence given by

$$\left|H(d,f)\right|^2 = a^2\Big(1+g^2+2g\cos\left(2\pi f\tau_0+\phi\right)\Big) = a^2\left(1+g^2+2g\cos\left(\frac{4\pi}{\lambda}\frac{h_\mathrm{t}h_\mathrm{r}}{d}+\phi\right)\right). \tag{5.7}$$

To calculate the large-scale fading, the power spectrum is averaged on a confined area. The functions a and g change relatively slow as the distance changes, but the term $\cos(\frac{4\pi}{\lambda}\frac{h_\mathrm{t}h_\mathrm{r}}{d}+\phi)$ in Eq. (5.7) has a spatial fading period [10] of

$$\Delta d|_{2\pi} = \frac{\lambda d^2}{2h_\mathrm{t}h_\mathrm{r}} = \frac{\lambda d}{\Delta l}\,. \tag{5.8}$$

Spatial averaging over a length of $\Delta d|_{2\pi}$ removes the small-scale fluctuations and leaves only the large-scale fading

$$\overline{\left|H(d)\right|^2} = a(d)^2\big(1+g(d)^2\big)\,. \tag{5.9}$$

The constructive and destructive envelopes of the two-ray model are then calculated. The effect of the RF bandwidth B is modeled through uniformly distributing the baseband transmit power in $P_x \sim \mathcal{U}(f_0 - {}^{B}\!/_{2}, f_0 + {}^{B}\!/_{2})$. The average receive power is then given by

$$\begin{aligned}\mathbb{E}_{P_x}\{|H|^2\} &= a^2(1+g^2)+2a^2g\int_{f'=f_0-{}^{B}\!/_{2}}^{f_0+{}^{B}\!/_{2}}\frac{1}{B}\cos\big(2\pi f'\tau_0+\phi\big)\mathrm{d}f'\\ &= a^2\big(1+g^2\big)+2a^2g\cos\big(\pi\tau_0 f_0+\phi\big)\operatorname{sinc}\big(\tau_0 B\big)\,.\end{aligned} \tag{5.10}$$

The sinc function is defined as $\operatorname{sinc}(x) = \frac{\sin(\pi x)}{\pi x}$. By moving along d, the phase ϕ varies over 2π. Because $-1 \le \cos\big(2\pi\tau_0 f_0+\phi\big) \le 1$, the following receive power envelopes are achieved:

$$\mathbb{E}_{P_x}\{|H|^2\} \le a^2\big(1+g^2\big)+2a^2g\big|\operatorname{sinc}\big(\tau_0 B\big)\big| \tag{5.11a}$$

$$\mathbb{E}_{P_x}\{|H|^2\} \ge a^2\big(1+g^2\big)-2a^2g\big|\operatorname{sinc}\big(\tau_0 B\big)\big|\,. \tag{5.11b}$$

5.1.3 Simplistic Modeling of Directive Antennas

To calculate the envelopes given above, one needs to know the antenna pattern to compute Eq. (5.4). Sometimes, only the gain values or half-power beam width values at elevation $\theta_{3\mathrm{dB}}$ and azimuth $\varphi_{3\mathrm{dB}}$ of the directive antennas are the known variables. To keep the model applicable, a simplified antenna model is used at this point, in which the pattern is based on a cosine function taken to a higher power. By doing this, all values except for the extrema $-1, 1$ will progressively decrease. The exponent n is derived to fulfill the half-power beam width. For example, the exponent of the elevation pattern (E-plane) is chosen to ensure that

$$\cos\left(\frac{\theta_{3\mathrm{dB}}}{2}\right)^n \overset{!}{=} \frac{1}{2} \quad\Rightarrow\quad n = \frac{-1}{\mathrm{ld}\left(\cos\left(\frac{\theta_{3\mathrm{dB}}}{2}\right)\right)}\,, \tag{5.12}$$

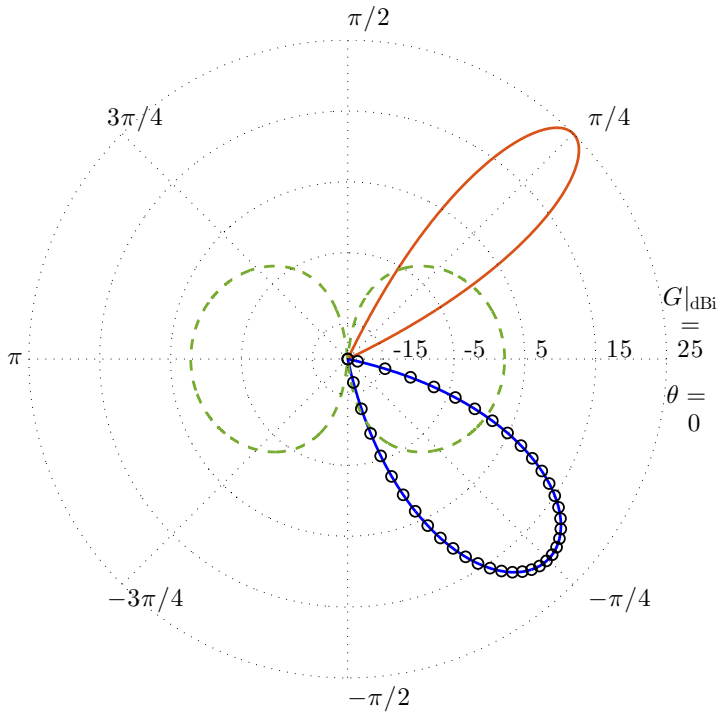

Figure 5.2: ***Different antenna pattern in the E-plane.*** The red directive pattern pointing toward $\pi/4$ is the antenna pattern used in this chapter ($\theta_{3\text{dB}} = 10°$ and $G = 25\,\text{dBi}$). The blue directive pattern pointing toward $-\pi/4$ is an example of a less directive antenna similar to that used for the measurements ($\theta_{3\text{dB}} = 18°$ and $G = 20\,\text{dBi}$). The superimposed black circular markers are the result of the Gaussian beam model. The pattern of a $\lambda/2$ dipol is sketched in green dashed lines for comparison.

where ld is the binary logarithm. The final gain pattern, including the mechanical alignments at elevation θ_a and azimuth φ_a, is given by

$$G(\theta, \theta_\text{a}, \theta_{3\text{dB}}, \varphi, \varphi_\text{a}, \varphi_{3\text{dB}}) = G_\text{max} \cos\left(\frac{\theta - \theta_\text{a}}{2}\right)^{\frac{-1}{\text{ld}\left(\cos\left(\frac{\theta_{3\text{dB}}}{2}\right)\right)}} \cos\left(\frac{\varphi - \varphi_\text{a}}{2}\right)^{\frac{-1}{\text{ld}\left(\cos\left(\frac{\varphi_{3\text{dB}}}{2}\right)\right)}} . \tag{5.13}$$

The example patterns generated by Eq. (5.13) are illustrated in Fig. 5.2. To the best of the author's knowledge, this practical approach of obtaining equations for the antenna patterns has not yet been proposed, yet this approach is of course very related to the Gaussian beam model [151, 152]

$$G_\text{Gauß}(\theta, \theta_\text{a}, \theta_{3\text{dB}}, \varphi, \varphi_\text{a}, \varphi_{3\text{dB}}) = G_\text{max} \exp\left\{-4\ln(2)\left(\frac{\theta - \theta_\text{a}}{\theta_{3\text{dB}}}\right)^2\right\} \exp\left\{-4\ln(2)\left(\frac{\varphi - \varphi_\text{a}}{\varphi_{3\text{dB}}}\right)^2\right\} , \tag{5.14}$$

where ln is the natural logarithm. However, there are drawbacks in using these methods: the missing side lobes and the inflexibility of the exact pattern since only half-power bandwidths are factored in.

Now the two-ray model, including the simplified antenna pattern in Eq. (5.13) and to the derived Eq. (5.9) and Eq. (5.11), is compared with the ray-tracing data from [96] (see Fig. 5.3). In [96], the SNR data were studied. To obtain the SNR values from the proposed model, the transmit power is then set to $P_\text{T} = 20\,\text{dBm}$, and the noise figure is selected to be $N_\text{F} = 10\,\text{dB}$ (see [96]). This is expressed as

$$\text{SNR}\big|_\text{dB} = P_\text{T}\big|_\text{dBm} + \mathbb{E}_{P_x}\{|H|^2\}\big|_\text{dB} - \big(-174\,\text{dBm/Hz} + 10\log_{10}(B)\big|_\text{dBHz} + N_\text{F}\big|_\text{dB}\big). \tag{5.15}$$

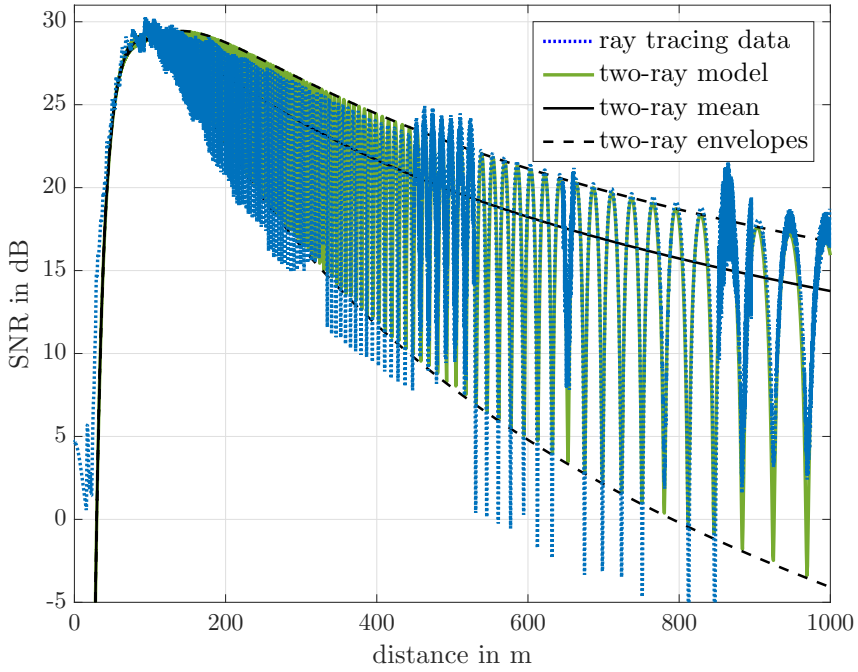

Figure 5.3: ***Two-ray model developed to provide a good description of the observed SNR in the ray-tracing study [96].*** Modeling the antenna patterns allows the SNR drop, caused by the misaligned antenna, to be captured well. The envelopes of the fading amplitude are relatively well approximated. The deviations are caused by the mismatches in the antenna pattern and by the superposition of more than just two propagation paths.

5.1.4 Two-Wave with Diffuse Power Model Parametrization

Although it is possible to conduct deterministic modeling as a two-ray ground reflection model, a statistical model captures uncertainties and variations, for example, about the phase change of the reflection. The envelopes (5.11) are normalized by the mean power (5.9) to achieve $\Omega \equiv 1$. The sum voltage V_Σ and the difference voltages V_Δ of both waves are then given by

$$V_{\Sigma|\Delta} = \sqrt{1 \pm \frac{2g\left|\operatorname{sinc}\left(\tau_0 B\right)\right|}{1+g^2}}\,. \tag{5.16}$$

The individual voltages V_1, V_2 are then obtained by solving the following system of equations:

$$V_1 + V_2 = V_\Sigma \tag{5.17a}$$
$$V_1 - V_2 = V_\Delta \tag{5.17b}$$

Plugging the solution of Eq.(5.17a) and Eq. (5.17b) into the definition of Δ leads to

$$\Delta(d) = \frac{2g\left|\operatorname{sinc}\left(\tau_0 B\right)\right|}{1+g^2} = \frac{2g(d)\left|\operatorname{sinc}\left(\frac{2h_\mathrm{t}h_\mathrm{r}}{d}\frac{B}{c}\right)\right|}{1+g(d)^2}\,. \tag{5.18}$$

It is not possible to derive the K-factor from the two-ray model since it assumes an LOS component and one specular reflection without modeling the other smaller components. Consequently, $\sigma \to 0$ and $K \to \infty$.

Fig. 5.4 compares the obtained parameter fits with the predicted values of the proposed model (black dashed lines). The second moment from the ray-tracing data is calculated using Eq. (2.11), while the filter length L_f is chosen adaptively according to Eq. (5.8). The ML fitted K-factor shows a negative trend as

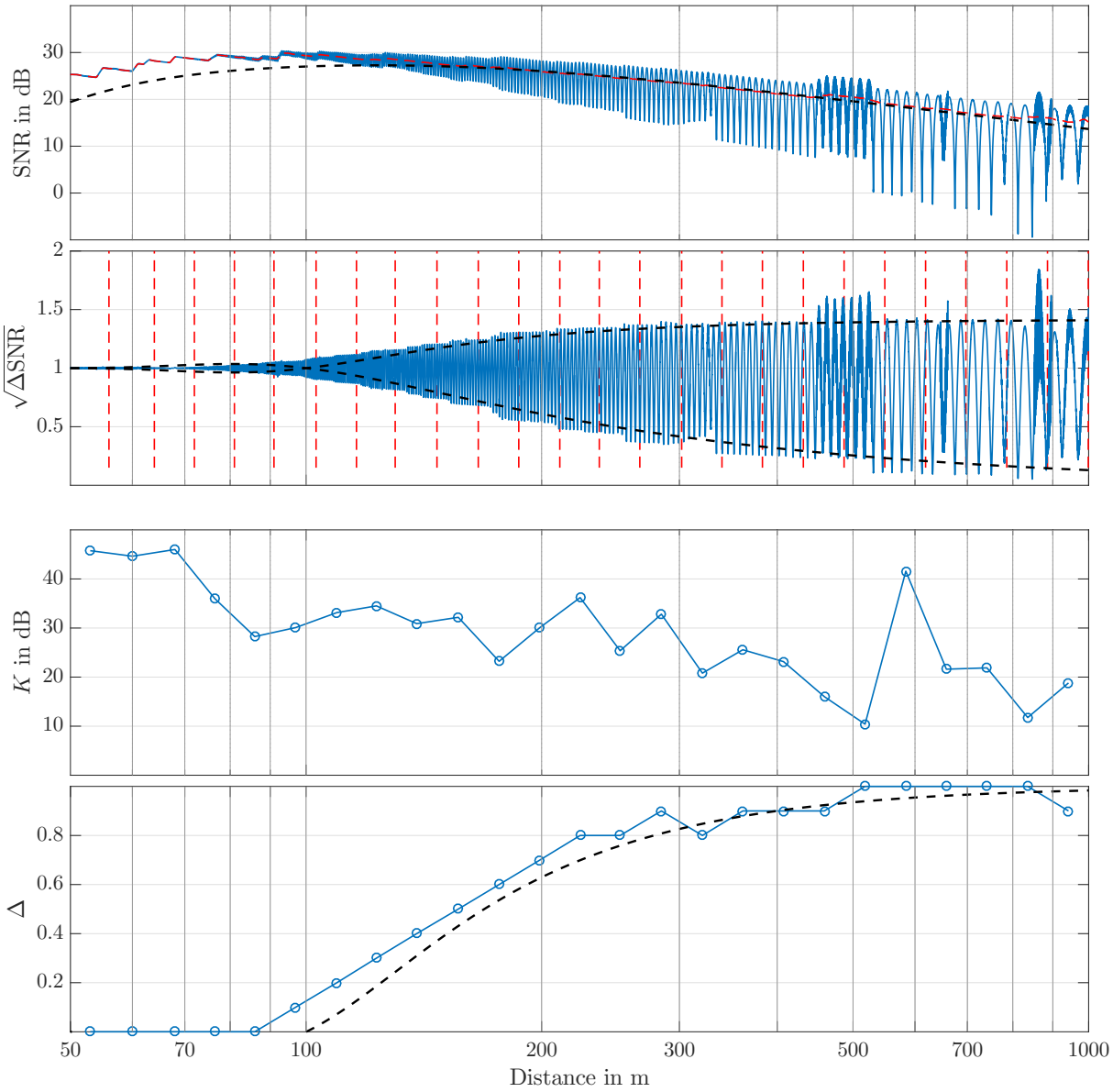

Figure 5.4: ***Fitted large-scale fading, fading envelopes, and Δ-parameters.*** (Panel 1) The SNR from Fig. 5.3 is shown with logarithmic abscissa scaling. The black dashed line shows the predicted large-scale power from Eq. (5.9). The red dashed line shows the estimated large-scale power, which is computed through the sliding average approach. (Panel 2) The SNR fluctuations are shown by removing the large-scale trend. The envelopes given in Eq. (5.16) are plotted in black dashed lines. The red, dashed, vertical lines show the evaluation regions for the ML parameter estimation. (Panel 3) This shows the ML fitted K-parameter of the TWDP model. The K-factor decreases with increasing distance as the directive antenna illuminates more surrounding buildings; hence, more multipath components are generated. (Panel 4) This panel presents the ML fitted Δ-parameter of the TWDP model. The theoretical prediction generated from the proposed model is again plotted as a black dashed line. The prediction and observation agree well.

the distance increases. Remember that directive antennas are used in this study, and they illuminate a bigger area at larger distances; hence, they allow more and more (smaller) reflections as the number of visible surrounding buildings increases. The predicted Δ-parameters from Eq. (5.18) agree well with the ML estimated parameters.

5.2 Link-Level Performance Study

Figure 5.4 shows that the SNR is within the range of $15\,\text{dB}$ to $25\,\text{dB}$ at almost all distances. However, the average receive SNR says little about the link-level performance of the transmission system. Although the trend shows that K-factors decrease with distance, the K-factor is assumed to be constant at this stage, and $K = 30\,\text{dB}$ will be assumed in the subsequent simulations. Three different values of $\Delta = (0.0, 0.7, 1.0)$ will be simulated to obtain representative results for very close distances, mid-range distances ($\approx 300\,\text{m}$), and far distances. A simulation that provides a corresponding Rice distribution (with Rician K-factor calculated according to Eq. (2.23)) is likewise given. Rayleigh fading ($K \equiv 0$) and Rician fading ($K = 30\,\text{dB}$, $\Delta \equiv 0$) is also simulated for reference.

The simulations assume single-carrier transmissions over frequency flat channels, and the one and only channel tap fades according to a TWDP model. All of the simulations assume that the channel is perfectly known to the receiver, and that the receiver employs a zero-forcing equalizer. Given that $K = 30\,\text{dB}$ and a specific Δ, a fading channel tap is thus simulated as described by Eq. (2.1). A transmission packet consists of 256 transmitted symbols, in which each transmitted symbol experiences an independent fading realization.

5.2.1 Uncoded BER

First, the bit error ratio (BER) performance of 4-quadrature amplitude modulation (QAM) is shown in Fig. 5.5. As Δ increases, the BER-performance gets increasingly worse, conferring with the violet line at $\Delta = 0.7$. The uncoded BER performance of TWDP fading at $\Delta \approx 1$ has led to the name "worse-than-Rayleigh" fading [67–71]. It can be seen in Fig. 5.5 that for high SNR, the BER of a TWDP fading channel decreases slower than the BER of a Rayleigh fading channel. At approximately $14\,\text{dB}$ SNR, the orange curve (TWDP) and the black curve (Rayleigh) cross. Likewise, the BER of the TWDP fading channel, starting at an SNR of approximately $5\,\text{dB}$, is significantly above the BER of the corresponding Rice channel. This behavior is explained by the fact that two specular components can perfectly cancel themselves. The signal then disappears and errors would still occur even with good average SNR transmission. At this point, note that the uncoded BER, of course, has little significance to a communication system performance.

5.2.2 Coded BER

For coding the block transmission, a turbo code is used similar to that standardized in 4G LTE [150]. The results in this subsection are obtained through a turbo coder with effective code rate (ECR) of 67%. Qualitatively, the TWDP fading channel (orange curve in Fig. 5.6) and the corresponding Rician fading channel (blue curve) show the same behavior. At a certain SNR value the orange curve crosses the blue curve, although the distance between both curves is much smaller now. However, the orange curve (TWDP fading) now becomes farther away from the black curve (Rayleigh fading), and the crossing point is at a very low BER. There is no "worse-than-Rayleigh" region visible after channel coding, because the channel coding can correct the bit errors caused by the deep fades of TWDP fading.

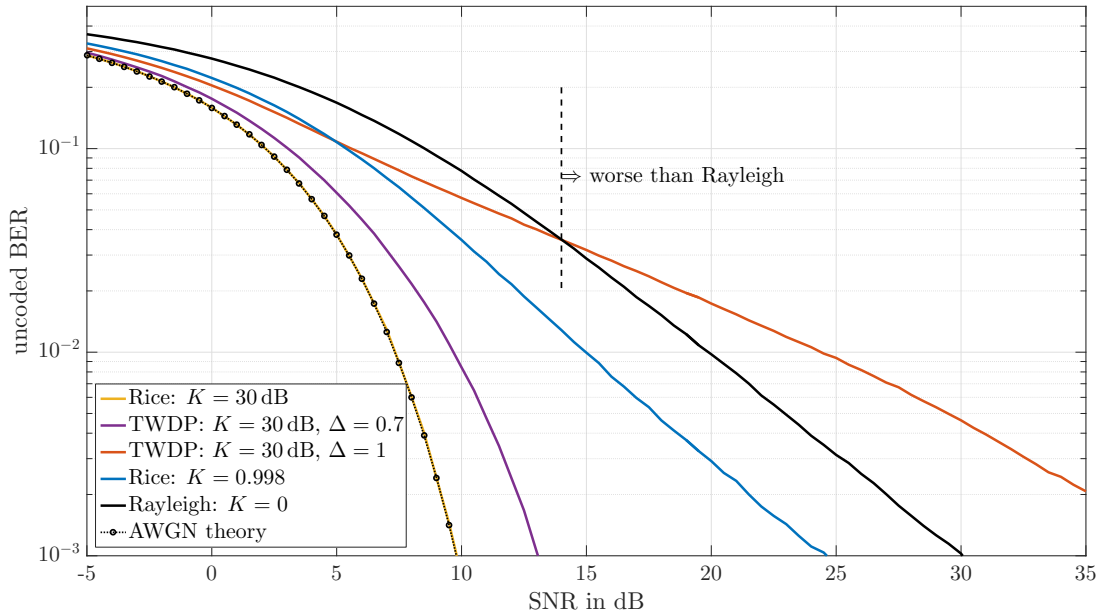

Figure 5.5: ***Simulation: Uncoded BER of 4-QAM with TWDP fading.*** At a K-factor of 30 dB, the BER of Rician fading already approaches AWGN bound. A Δ-parameter of $\Delta = 0.7$ shifts away the BER performance by serveral decibels, albeit it still shows a BER performance that is much better than the BER performance of Rayleigh. At $\Delta = 1$, the "worse-than-Rayleigh" BER performance is visible above 14 dB SNR.

Recall that in Fig. 2.1, in addition to the high probability of deep fades, it is also highly probable that the two specular paths would add constructively. Thus, many symbols experience a high instantaneous SNR, thereby supporting the channel coding.

5.2.3 Throughput

To estimate the system throughput, the packet transmission is tested on the same channel through many possible modulation and coding schemes (MCSs) (see Table 5.1). The resulting estimate will be discarded if there is any bit error in the packet. Hence, the packet that has the highest product of spectral efficiency of the modulation alphabet and highest ECR is chosen among all the error-free packets. This is illustrated in Fig. 5.7 through the individual throughput curves of all MCS (for TWDP fading with $\Delta = 1$ and Rician fading). The envelope of the maximum among all MCS lies above the throughput curve of all individual

Table 5.1: Modulation and Coding Schemes

Modulation	**ECR**				
4-QAM	21%	16-QAM	43%	64-QAM	54%
4-QAM	25%	16-QAM	46%	64-QAM	58%
4-QAM	30%	16-QAM	50%	64-QAM	62%
4-QAM	36%	16-QAM	54%	64-QAM	67%
4-QAM	42%	16-QAM	58%	64-QAM	70%
4-QAM	50%	16-QAM	61%	64-QAM	74%
4-QAM	54%	16-QAM	67%	64-QAM	80%
4-QAM	58%	16-QAM	73%	64-QAM	85%
4-QAM	63%	16-QAM	80%	64-QAM	90%
4-QAM	67%				
4-QAM	73%				

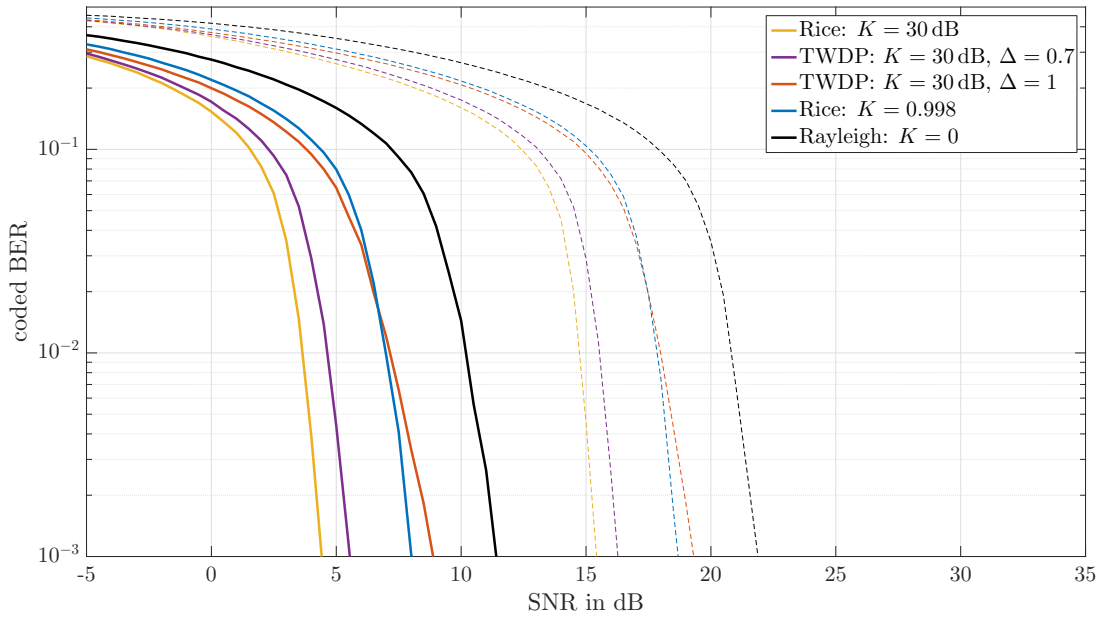

Figure 5.6: ***Simulation: Coded BER of 4-QAM and 64-QAM with TWDP fading.*** The thick solid lines show the BER performance of 4-QAM, while the dashed lines show the 64-QAM performance. In the coded BER plot, there is hardly a difference between TWDP fading and the corresponding Rician fading. Nevertheless, TWDP fading significantly differs from Rayleigh fading, and there is no "worse-than-Rayleigh" region visible.

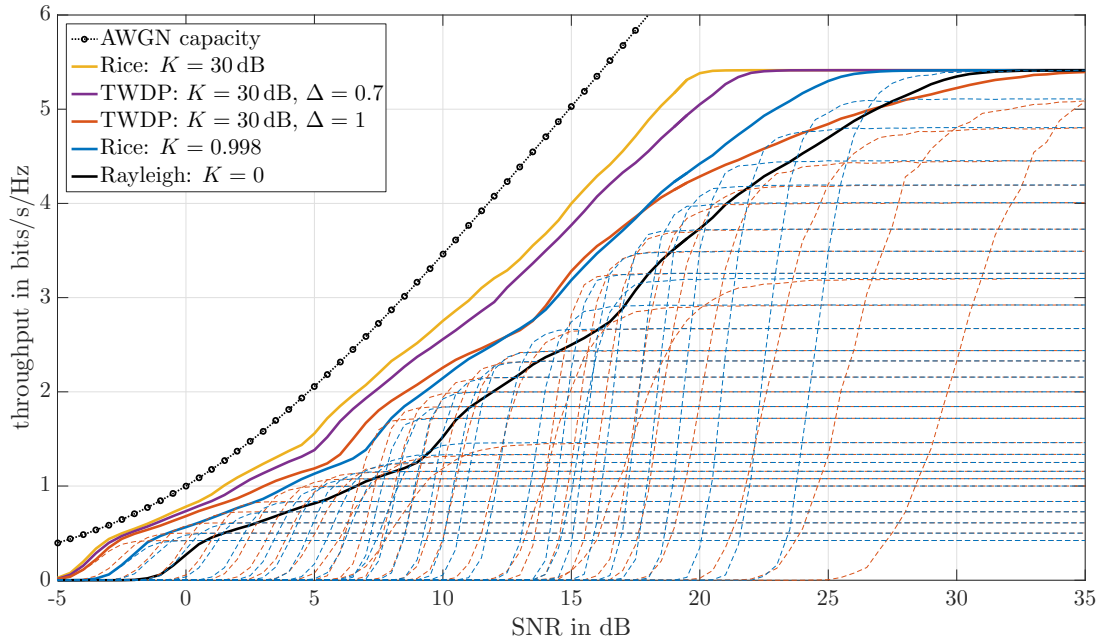

Figure 5.7: ***Simulation: Throughput comparison of different parameters tuples of TWDP fading.*** Rician fading (yellow curve) with $K = 30\,\mathrm{dB}$, comes close to the AWGN capacity, while there is a significant gap in Rayleigh fading (black curve). All other parameter configurations lie in between. For TWDP fading with $\Delta \ll 1$, the gap to Rician fading is in the order of 1 dB. There is a gap of approximately 3 dB at $\Delta = 1$. In terms of throughput performance, TWDP fading (with $\Delta = 1$) and the corresponding Rician fading ($K = 0.998$) are very close. The only remarkable difference between the two curves is the throughput gap at high SNR. TWDP fading needs a higher SNR to get to the maximum throughput of an MCS. The gap becomes visible due to limited MCS and due to a missing 256-QAM constellation in the simulations. The performance of the individual MCS is plotted with dashed lines.

MCS curves due to Jensen's inequality. To obtain statistically meaningful results, the mean value from 2000 Monte Carlo simulation is calculated.

One key insight from the throughput simulations conducted is that it does not matter if a Rice or TWDP model is simulated, as long as the "correct" Rician K-factor is applied. This correct Rician K-factor, as provided in (2.23), is very counterintuitive. In the presented simulations, the Rician K-factor is $K_{\text{Rice}} = 0.998 \approx 0\,\text{dB}$. This low K-factor leads to a fading distribution where deep fades are present (as for TWDP fading). Simulating naively millimeter wave transmissions with high Rician K-factors will lead to performance overestimations in many cases. This performance overestimation can be seen in Fig. 5.7 as the gap between the yellow and the blue (or orange) curve.

6 Conclusions and Possible Future Directions

This thesis demonstrates, by means of model selection and hypothesis testing, that TWDP fading can explain measured indoor millimeter wave channels, measured outdoor vehicular channels, and simulated railway communication channels.

The Rician fits of reported studies must be considered carefully. This dissertation has shown extensively that Rician K-factors tend to be much smaller than their TWDP companions. There is much more power in the specular components than in those predicted by the Rician fit. Likewise, the TWDP fading fit considers that the two specular waves can possibly cancel out each other. In other words, with the same K-factor, TWDP fading has deeper fades than the fades predicted using a Rice distribution.

The results of this study have been verified through independent data sources. Moreover, for the first indoor measurement campaign, the second indoor measurement campaign, and the outdoor measurement campaign, even a different RF-hardware was used. The scalar-valued results of the first indoor measurement campaign were limited to the results in the frequency-domain, whereas the vector-valued results allowed analysis in the spatial-domain and in the time-domain. Having this strong evidence at hand, it is thus claimed in this thesis that the TWDP fading model occurs both in mmWave indoor channels and in outdoor channels. The flexibility of this model further allows Rician fading ($\Delta \equiv 0$) and Rayleigh fading ($K \equiv 0$) results to be obtained using the same channel model.

Another key finding is that the size of interacting objects, such as overtaking vehicles, plays a crucial role in the statistics of millimeter wave vehicular channels. The statistical evaluation of an overtaking process has shown that only very large objects (trucks and buses) influence large-scale fading. Large vehicles potentially increase the receive power by several decibels through the reflections on their side wall. For smaller vehicles, the large-scale fading did not change. Rician fading is a good model for small-scale fading, unless a vehicle is in the "bandwidth ellipse" in which case the TWDP distribution provides a better fit. The larger the vehicle is, the larger the Δ-parameter would be.

The analysis of Doppler dispersion has shown that the increased Doppler effect in the millimeter waves is not directly translated to the RMS Doppler spread. The RMS Doppler spread is extremely low due to the spatial filtering of the horn antenna and the very strong LOS component. Only for large vehicles does this value increase significantly during overtaking. Note that the observed maximum value is a lot smaller than the maximum value that standard models (uniform, Jakes) would predict. The maximum observed RMS Doppler spread is approximately four times larger than the phase noise of the measurement system. It is highly unlikely that a commercial system without "perfect" frequency synchronization, or worse reference clocks, would experience this relatively small increase of the RMS Doppler spread at all.

The last chapter has shown that both the two-ray and TWDP models can be easily parametrized by geometry, bandwidth, and antenna directivity in order to accurately reproduce the ray-tracing data. This is the first attempt to use geometry to model a TWDP channel.

Finally, this thesis presented a link-level study, in which TWDP fading was analyzed through uncoded BER, coded BER, and throughput. The results show that TWDP fading at $\Delta = 1$ has a significantly worse uncoded BER than the uncoded BER of Rayleigh fading at high SNR; however, the opposite is true after coding. The term "worse-than-Rayleigh fading" [67–71] is therefore very ambiguous. Accordingly, the throughput is higher in TWDP fading than in Rayleigh fading. The comparision of the throughput results of TWDP fading and its closest fitting Rice distribution shows that their performances are very close.

Criticism and Open Issues This thesis has focused on channel charaterization, and thus has only shown the occurrence of TWDP fading. The biggest open issue then is the modeling and prediction of model parameters based on the shape of the interacting objects. Building on the channel models, the parameters must be validated based on further measurements or ray-tracing studies. After modeling the interacting objects, their occurrence in the delay domain has to be modeled. Fig. 3.12 in Chapter 2 has demonstrated that different delay taps fade with different statistics. Furthermore, the actual number of channel taps to consider is not treated in this thesis, albeit a framework for such analysis can be found in [153–155].

In non-static environments, mainly in the case of vehicular channels, the channel needs to be modeled as a stochastic process, where the parameter tuple evolves according to some correlation function. This modeling approach needs to take into account that the channel statistic can only be considered stationary in a small spatial area [87, 146, 156]. The non-stationarity during the overtaking process was shown in Fig. 4.12 in Chapter 4; but again, its modeling is beyond the scope of this thesis. Once such channel models are at hand and validated, link-level performance studies [65, 150, 157–159] and large-scale system-level performance studies [160] will provide meaningful results.

A topic that was not treated at all in this thesis is the beam alignment (signal processing) challenge. Beam alignment approaches based on the estimation of the instantaneous channel coefficients [19, 21, 23, 26, 161–168] will suffer from performance degradation due to TWDP fading. This performance degradation was initially studied in the recent work of [169]; however, they assumed Rayleigh fading. A simplified analysis of beam alignment under TWDP fading has been submitted to [170]. As such, the behavior of the beam alignment algorithms under TWDP fading still needs to be carefully studied.

An important missing element is the issue on the effects of polarization. In the indoor measurements conducted in this study, the polarization is only clearly defined at LOS (vertical polarization was used) due to the rotation in azimuth and elevation. On the other hand, an omnidirectional antenna ($\lambda/4$ vertical monopol) was installed on the car in the vehicular measurement campaign. This antenna is again vertically polarized. Future measurements should measure dual – polarimetric as in the study of [171].

Table of Abbreviations

AIC	Akaike's information criterion
AWG	arbitrary waveform generator
AWGN	additive white Gaussian noise
BER	bit error ratio
CDF	cumulative distribution function
CIR	channel impulse response
DFT	discrete Fourier transform
DPS	discrete prolate spheroidal
DSD	Doppler spectral density
ECR	effective code rate
IF	intermediate frequency
IQ	in-phase and quadrature-phase
LO	local oscillator
LOS	line-of-sight
LSF	local scattering function
MCS	modulation and coding scheme
MLE	maximum likelihood estimation
mmWave	millimeter wave
MPC	multipath component
NLOS	non-line-of-sight
PDF	probability density function
PDP	power delay profile
PLL	phase-locked loop
QAM	quadrature amplitude modulation
RF	radio frequency
RMS	root mean square
RX	receiver
SA	signal analyzer
SNR	signal-to-noise ratio
SUV	sport utility vehicle
TWDP	two-wave with diffuse power
TX	transmitter
VNA	vector network analyzer
V2V	vehicle-to-vehicle

List of Figures

1.1 Total, dry, air and water-vapor zenith attenuation from sea level. 2
1.2 Directive communications through adaptive beamforming. 2

2.1 Comparison of Rayleigh, Rician, and TWDP fading. 9
2.2 CDF: Distribution fitting for exemplary frequency domain measurement data. 12
2.3 Transition to Rician Fading. 12
2.4 Relationship of the Rician and TWDP K-factor. 14
2.5 RF setup of the frequency-domain channel sounder. 15
2.6 RF setup for the time-domain channel sounder. 17
2.7 Extended time-domain channel sounder with synchronization unit. 18

3.1 Floor plan of the measured environment. 22
3.2 Photograph of the mechanical setup for the scalar-valued wideband measurements from the receiver's point of view. 23
3.3 Estimated directional receive power of the scalar-valued wideband measurements. . . . 24
3.4 Estimated K-factor and Δ-parameter obtained through scalar wideband data. 25
3.5 Photograph of the improved mechanical setup for the vector-valued measurements from the receiver's point of view. 26
3.6 Estimated directional receive power of vector-valued measurements. 27
3.7 Spatial sampling grid. 27
3.8 Estimated K-factor and Δ-parameter of the vector-valued measurements. 28
3.9 Laboratory desk surface reflection. 28
3.10 Estimated (K, Δ) parameter tuple of the TWDP fading model. 29
3.11 Spatial correlation plot at $\varphi = 160°, 340°$ and at $\theta = 110°$. 30
3.12 Scatter-plot of the CIRs. 32
3.13 Violin-plot of the CIR time-gated for the wall reflection. 33

4.1 Bird's-eye view of the measurement site as scaled sketch. 36
4.2 Measurement site. 36
4.3 Statistical evaluation of the LOS power variations. 38
4.4 Webcam snapshot of the exemplary overtaking truck. 40
4.5 Result of the post-processing of the LOS tap for the exemplary truck shown in Fig. 4.4. . . 40
4.6 Scaled sketch of the bandwidth ellipse. 41
4.7 CDF evolution over distance. 42
4.8 MLE fitted parameter tuple $(\hat{K}, \hat{D})$ for the exemplary truck channel from Fig. 4.5 42
4.9 ML fitted (K, Δ) parameters and model statistic. 44
4.10 Effective vehicle length estimation through exponential modeling of the parameter tuple. 45
4.11 Post-processing steps to obtain the RMS delay spread and RMS Doppler spread. 48
4.12 Data evaluation based on the LSF. 49

5.1 A sketch of the analyzed scenario. 51
5.2 Different antenna pattern in the E-plane. 54

5.3 Two-ray model developed to provide a good description of the observed SNR in the ray-tracing study [96]. 55
5.4 Fitted large-scale fading, fading envelopes, and Δ-parameters. 56
5.5 Simulation: Uncoded BER of 4-QAM with TWDP fading. 58
5.6 Simulation: Coded BER of 4-QAM and 64-QAM with TWDP fading. 59
5.7 Simulation: Throughput comparison of different parameters tuples of TWDP fading. . . 59

List of Tables

2.1 Frequency-Domain Channel Sounder Parameters Used in Chapter 3 16
2.2 Time-Domain Channel Sounder Parameters Used in Chapter 3 16
2.3 Time-Domain Channel Sounder Parameters Used in Chapter 4 19

5.1 Modulation and Coding Schemes 58

Bibliography

[1] ETSI. "LTE; Evolved Universal Terrestrial Radio Access (E-UTRA); User Equipment (UE) radio transmission and reception". In: *3GPP TS 36.101 version 14.5.0 Release 14* (2017).

[2] T. S. Rappaport, W. Roh, and K. Cheun. "Mobile's millimeter-wave makeover". In: *IEEE Spectrum* 51.9 (2014).

[3] J. G. Andrews et al. "What Will 5G Be?" In: *IEEE Journal on Selected Areas in Communications* 32.6 (2014).

[4] Theodore S Rappaport, James N Murdock, and Felix Gutierrez. "State of the art in 60-GHz integrated circuits and systems for wireless communications". In: *Proceedings of the IEEE* 99.8 (2011).

[5] Martin Steinbauer, Andreas F Molisch, and Ernst Bonek. "The double-directional radio channel". In: *IEEE Antennas and Propagation Magazine* 43.4 (2001).

[6] Christopher R Anderson and Theodore S Rappaport. "In-building wideband partition loss measurements at 2.5 and 60 GHz". In: *IEEE Transactions on Wireless Communications* 3.3 (2004).

[7] Nektarios Moraitis and Philip Constantinou. "Measurements and characterization of wideband indoor radio channel at 60 GHz". In: *IEEE Transactions on Wireless Communications* 5.4 (2006).

[8] Suiyan Geng et al. "Millimeter-wave propagation channel characterization for short-range wireless communications". In: *IEEE Transactions on Vehicular Technology* 58.1 (2009).

[9] Karma Wangchuk et al. "Double Directional Millimeter Wave Propagation Channel Measurement and Polarimetric Cluster Properties in Outdoor Urban Pico-cell Environment". In: *IEICE Transactions on Communications* 100.7 (2017).

[10] Michael Peter, Wilhelm Keusgen, and Richard J Weiler. "On path loss measurement and modeling for millimeter-wave 5G". In: *Proc. of 9th European Conference on Antennas and Propagation (EuCAP)*. 2015.

[11] Michael Peter et al. "Channel measurement and modeling for 5G urban microcellular scenarios". In: *Sensors* 16.8 (2016).

[12] Mathew K Samimi, Theodore S Rappaport, and George R MacCartney. "Probabilistic omnidirectional path loss models for millimeter-wave outdoor communications". In: *IEEE Wireless Communications Letters* 4.4 (2015).

[13] Sijia Deng, Mathew K Samimi, and Theodore S Rappaport. "28 GHz and 73 GHz millimeter-wave indoor propagation measurements and path loss models". In: *Proc. of IEEE International Conference on Communication Workshop (ICCW)*. 2015.

[14] George R MacCartney et al. “Millimeter-wave omnidirectional path loss data for small cell 5G channel modeling”. In: *IEEE Access* 3 (2015).

[15] Wonil Roh et al. “Millimeter-wave beamforming as an enabling technology for 5G cellular communications: Theoretical feasibility and prototype results”. In: *IEEE Communications Magazine* 52.2 (2014).

[16] Sooyoung Hur et al. “Millimeter wave beamforming for wireless backhaul and access in small cell networks”. In: *IEEE Transactions on Communications* 61.10 (2013).

[17] Shu Sun et al. “MIMO for millimeter-wave wireless communications: Beamforming, spatial multiplexing, or both?” In: *IEEE Communications Magazine* 52.12 (2014).

[18] Zhouyue Pi and Farooq Khan. “An introduction to millimeter-wave mobile broadband systems”. In: *IEEE Communications Magazine* 49.6 (2011).

[19] Robert W Heath et al. “An overview of signal processing techniques for millimeter wave MIMO systems”. In: *IEEE Journal of Selected Topics in Signal Processing* 10.3 (2016).

[20] Jeffrey G Andrews et al. “Modeling and analyzing millimeter wave cellular systems”. In: *IEEE Transactions on Communications* 65.1 (2017).

[21] Ahmed Alkhateeb et al. “Channel estimation and hybrid precoding for millimeter wave cellular systems”. In: *IEEE Journal of Selected Topics in Signal Processing* 8.5 (2014).

[22] Mandar N Kulkarni, Amitava Ghosh, and Jeffrey G Andrews. “A comparison of MIMO techniques in downlink millimeter wave cellular networks with hybrid beamforming”. In: *IEEE Transactions on Communications* 64.5 (2016).

[23] Erich Zöchmann, Stefan Schwarz, and Markus Rupp. “Comparing antenna selection and hybrid precoding for millimeter wave wireless communications”. In: *Proc. of IEEE Sensor Array and Multichannel Signal Processing Workshop (SAM)*. 2016.

[24] Stefan Pratschner et al. “A mutual coupling model for massive MIMO applied to the 3GPP 3D channel model”. In: *Proc. of 25th European Signal Processing Conference (EUSIPCO)*. 2017.

[25] John Brady, Nader Behdad, and Akbar M Sayeed. “Beamspace MIMO for millimeter-wave communications: System architecture, modeling, analysis, and measurements”. In: *IEEE Transactions on Antennas and Propagation* 61.7 (2013).

[26] Yong Zeng and Rui Zhang. “Millimeter wave MIMO with lens antenna array: A new path division multiplexing paradigm”. In: *IEEE Transactions on Communications* 64.4 (2016).

[27] Yong Zeng and Rui Zhang. “Cost-effective millimeter-wave communications with lens antenna array”. In: *IEEE Wireless Communications* 24.4 (2017).

[28] Harry L Van Trees. *Optimum array processing: Part IV of detection, estimation, and modulation theory*. John Wiley & Sons, 2004.

[29] Diego Dupleich et al. “Influence of System Aspects in Propagation Based Evaluation of Beam-forming at mm-Waves”. In: *Proc. of the 12th European Conference on Antennas and Propagation (EuCAP)*. 2018.

[30] PL Chin Cheong. "Multipath component estimation for indoor radio channels". In: *Proc. of IEEE Global Telecommunications Conference (GLOBECOM)*. Vol. 2. 1996.

[31] Andreas G Siamarou. "Wideband propagation measurements and channel implications for indoor broadband wireless local area networks at the 60 GHz band". In: *Wireless Personal Communications* 27.1 (2003).

[32] Fernando J Velez, Luis M Correia, and José M Brázio. "Frequency reuse and system capacity in mobile broadband systems: comparison between the 40 and 60 GHz bands". In: *Wireless Personal Communications* 19.1 (2001).

[33] FJ Velez, M Dinis, and J Fernandes. "Mobile broadband systems: Research and visions". In: *IEEE Vehicular Technology Society News* 52.2 (2005).

[34] Sylvain Ranvier, Jarmo Kivinen, and Pertti Vainikainen. "Millimeter-wave MIMO radio channel sounder". In: *IEEE Transactions on Instrumentation and Measurement* 56.3 (2007).

[35] Peter FM Smulders. "Statistical characterization of 60-GHz indoor radio channels". In: *IEEE Transactions on Antennas and Propagation* 57.10 (2009).

[36] Katsuyuki Haneda, Carl Gustafson, and Shurjeel Wyne. "60 GHz spatial radio transmission: Multiplexing or beamforming?" In: *IEEE Transactions on Antennas and Propagation* 61.11 (2013).

[37] Sana Salous et al. "Wideband MIMO channel sounder for radio measurements in the 60 GHz band". In: *IEEE Transactions on Wireless Communications* 15.4 (2016).

[38] Juyul Lee et al. "Measurement-Based Propagation Channel Characteristics for Millimeter-Wave 5G Giga Communication Systems". In: *ETRI Journal* 38.6 (2016).

[39] Joni Vehmas et al. "Millimeter-Wave Channel Characterization at Helsinki Airport in the 15, 28, and 60 GHz Bands". In: *Proc. of IEEE Vehicular Technology Conference (VTC-Fall)*. 2016.

[40] Erich Zöchmann et al. "Directional Evaluation of Receive Power, Rician K-factor and RMS Delay Spread Obtained from Power Measurements of 60 GHz Indoor Channels". In: *Proc. of IEEE-APS Topical Conf. on Antennas and Propagation in Wireless Communications (APWC)*. 2016.

[41] George R MacCartney and Theodore S Rappaport. "A flexible millimeter-wave channel sounder with absolute timing". In: *IEEE Journal on Selected Areas in Communications* 35.6 (2017).

[42] Junghoon Ko et al. "Millimeter-wave channel measurements and analysis for statistical spatial channel model in in-building and urban environments at 28 GHz". In: *IEEE Transactions on Wireless Communications* 16.9 (2017).

[43] Diego Dupleich et al. "Influence of system aspects on fading at mm-waves". In: *IET Microwaves, Antennas & Propagation* 12.4 (2017).

[44] F. Fuschini et al. "Analysis of In-Room mm-Wave Propagation: Directional Channel Measurements and Ray Tracing Simulations". In: *Journal of Infrared, Millimeter, and Terahertz Waves* 38.6 (2017).

[45] Xianyue Wu et al. “60-GHz millimeter-wave channel measurements and modeling for indoor office environments”. In: *IEEE Transactions on Antennas and Propagation* 65.4 (2017).

[46] Bo Ai et al. “On indoor millimeter wave massive MIMO channels: Measurement and simulation”. In: *IEEE Journal on Selected Areas in Communications* 35.7 (2017).

[47] Erich Zöchmann et al. “Associating Spatial Information to Directional Millimeter Wave Channel Measurements”. In: *Proc. of IEEE Vehicular Technology Conference (VTC-Fall)*. 2017.

[48] Jiri Blumenstein et al. “In-Vehicle Channel Measurement, Characterization, and Spatial Consistency Comparison of 3–11 GHz and 55–65 GHz Frequency Bands”. In: *IEEE Transactions on Vehicular Technology* 66.5 (2017).

[49] Theodore S Rappaport et al. “Millimeter wave mobile communications for 5G cellular: It will work!” In: *IEEE Access* 1.1 (2013).

[50] Diego Dupleich et al. “Investigations on fading scaling with bandwidth and directivity at 60 GHz”. In: *Proc. of 11th European Conference on Antennas and Propagation (EUCAP)*. 2017.

[51] Naveed Iqbal et al. “On the stochastic and deterministic behavior of mmWave channels”. In: *Proc. of 11th European Conference on Antennas and Propagation (EUCAP)*. 2017.

[52] Naveed Iqbal et al. “Modeling of Intra-Cluster Multipaths for 60 GHz Fading Channels”. In: *Proc. of the 12th European Conference on Antennas and Propagation (EuCAP)*. 2018.

[53] Mathew K Samimi et al. “28 GHz millimeter-wave ultrawideband small-scale fading models in wireless channels”. In: *Proc. of IEEE 83rd Vehicular Technology Conference (VTC-Spring)*. 2016.

[54] Shu Sun et al. “Millimeter wave small-scale spatial statistics in an urban microcell scenario”. In: *Proc. of IEEE International Conference on Communications (ICC)*. 2017.

[55] Theodore S Rappaport et al. “Small-Scale, Local Area, and Transitional Millimeter Wave Propagation for 5G Communications”. In: *IEEE Transactions on Antennas and Propagation* (2017).

[56] Gregory D Durgin. *Space-time wireless channels*. Upper Saddle River: Prentice Hall Professional, 2003.

[57] Theodoros Mavridis et al. “Near-body shadowing analysis at 60 GHz”. In: *IEEE Transactions on Antennas and Propagation* 63.10 (2015).

[58] Juan M Romero-Jerez et al. “The Fluctuating Two-Ray Fading Model: Statistical Characterization and Performance Analysis”. In: *IEEE Transactions on Wireless Communications* (2017).

[59] Jiayi Zhang et al. “New results on the fluctuating two-ray model with arbitrary fading parameters and its applications”. In: *IEEE Transactions on Vehicular Technology* 67.3 (2018).

[60] Wen Zeng et al. “Physical Layer Security over Fluctuating Two-Ray Fading Channels”. In: *IEEE Transactions on Vehicular Technology* (2018).

[61] Raffaele Esposito and L Wilson. “Statistical properties of two sine waves in Gaussian noise”. In: *IEEE Transactions on Information Theory* 19.2 (1973).

[62] Soon H Oh and Kwok H Li. "BER performance of BPSK receivers over two-wave with diffuse power fading channels". In: *IEEE Transactions on Wireless Communications* 4.4 (2005).

[63] Seyed Ali Saberali and Norman C Beaulieu. "New expressions for TWDP fading statistics". In: *IEEE Wireless Communications Letters* 2.6 (2013).

[64] Milind Rao et al. "MGF approach to the analysis of generalized two-ray fading models". In: *IEEE Transactions on Wireless Communications* 14.5 (2015).

[65] Stefan Schwarz. "Outage Investigation of Beamforming over Random-Phase Finite-Scatterer MISO Channels". In: *IEEE Signal Processing Letters* (2017).

[66] S. Schwarz. "Outage-Based Multi-User Admission Control for Random-Phase Finite-Scatterer MISO Channels". In: *Proc. of IEEE Vehicular Technology Conference (VTC-Fall)*. Toronto, Canada, 2017.

[67] Jeff Frolik. "A case for considering hyper-Rayleigh fading channels". In: *IEEE Transactions on Wireless Communications* 6.4 (2007).

[68] Jeff Frolik. "On appropriate models for characterizing hyper-Rayleigh fading". In: *IEEE Transactions on Wireless Communications* 7.12 (2008).

[69] Jeff Frolik et al. "A compact reverberation chamber for hyper-Rayleigh channel emulation". In: *IEEE Transactions on Antennas and Propagation* 57.12 (2009).

[70] David W Matolak and Jeff Frolik. "Worse-than-Rayleigh fading: Experimental results and theoretical models". In: *IEEE Communications Magazine* 49.4 (2011).

[71] Lu'ay Bakir and Jeff Frolik. "Diversity gains in two-ray fading channels". In: *IEEE Transactions on Wireless Communications* 8.2 (2009).

[72] Erich Zöchmann et al. "Associating Spatial Information to Directional Millimeter Wave Channel Measurements". In: *Proc. of IEEE 86th Vehicular Technology Conference (VTC-Fall)*. 2017.

[73] Kenneth P Burnham and David R Anderson. *Model selection and multimodel inference: a practical information-theoretic approach*. New York: Springer Science & Business Media, 2003.

[74] Robert W Frick. "The appropriate use of null hypothesis testing." In: *Psychological Methods* 1.4 (1996).

[75] Junil Choi et al. "Millimeter-wave vehicular communication to support massive automotive sensing". In: *IEEE Communications Magazine* 54.12 (2016).

[76] Tsuneo Tokumitsu et al. "Application of GaAs device technology to millimeter-waves". In: *SEI Technical Review* 79 (2014).

[77] Preeti Kumari et al. "IEEE 802.11 ad-based Radar: An Approach to Joint Vehicular Communication-Radar System". In: *IEEE Transactions on Vehicular Technology* 67.4 (2018).

[78] Holger Meinel and A Plattner. "Millimetre-wave propagation along railway lines". In: *IEE Proceedings F (Communications, Radar and Signal Processing)* 130.7 (1983).

[79] Akihito Kato et al. “Propagation characteristics of 60-GHz millimeter waves for ITS inter-vehicle communications”. In: *IEICE Transactions on Communications* 84.9 (2001).

[80] Satoshi Takahashi et al. “Distance Dependence of Path Loss for Millimeter Wave Inter-Vehicle Communications”. In: *Radioengineering* 13.4 (2004).

[81] Atsushi Yamamoto et al. “Path-loss prediction models for intervehicle communication at 60 GHz”. In: *IEEE Transactions on Vehicular Technology* 57.1 (2008).

[82] Manuel García Sánchez, Mónica Portela Táboas, and Edgar Lemos Cid. “Millimeter wave radio channel characterization for 5G vehicle-to-vehicle communications”. In: *Measurement* 95 (2017).

[83] Hui Wang et al. “Fading Characterization of 73 GHz Millimeter-Wave V2V Channel Based on Real Measurements”. In: *Communication Technologies for Vehicles* (2018).

[84] A. Prokes et al. “Time-domain nonstationary intra-car channel measurement in 60 GHz band”. In: *Proc. of International Conference on Advanced Technologies for Communications (ATC)*. 2016.

[85] Jiri Blumenstein et al. “Time-varying K factor of the mm-Wave vehicular channel: Velocity, vibrations and the road quality influence”. In: *Proc. of IEEE 28th Annual International Symposium on Personal, Indoor, and Mobile Radio Communications (PIMRC)*. 2017.

[86] A. Loch et al. “Mm-Wave on wheels: Practical 60 GHz vehicular communication without beam training”. In: *Proc. of 9th International Conference on Communication Systems and Networks (COMSNETS)*. 2017.

[87] Laura Bernadó et al. “Time-and Frequency-Varying K-Factor of Non-Stationary Vehicular Channels for Safety-Relevant Scenarios”. In: *IEEE Transactions on Intelligent Transportation Systems* 16.2 (2015).

[88] Vutha Va, Junil Choi, and Robert W Heath Jr. “The impact of beamwidth on temporal channel variation in vehicular channels and its implications”. In: *IEEE Transactions on Vehicular Technology* 66.6 (2017).

[89] Javier Lorca, Mythri Hunukumbure, and Yue Wang. “On Overcoming the Impact of Doppler Spectrum in Millimeter-Wave V2I Communications”. In: *Proc. of IEEE Globecom Workshops (GC Wkshps)*. 2017.

[90] Howard Xia et al. “Radio propagation characteristics for line-of-sight microcellular and personal communications”. In: *IEEE Transactions on Antennas and Propagation* 41.10 (1993).

[91] Martin J Feuerstein et al. “Path loss, delay spread, and outage models as functions of antenna height for microcellular system design”. In: *IEEE Transactions on Vehicular Technology* 43.3 (1994).

[92] Jürgen Kunisch and Jörg Pamp. “Wideband car-to-car radio channel measurements and model at 5.9 GHz”. In: *Proc. of IEEE Vehicular Technology Conference (VTC-Fall)*. 2008.

[93] Johan Karedal et al. “Path loss modeling for vehicle-to-vehicle communications”. In: *IEEE Transactions on Vehicular Technology* 60.1 (2011).

[94] Christoph Sommer, Stefan Joerer, and Falko Dressler. "On the applicability of two-ray path loss models for vehicular network simulation". In: *Proc. of IEEE Vehicular Networking Conference (VNC)*. 2012.

[95] Atsushi Yamamoto et al. "Effect of road undulation on the propagation characteristics of inter-vehicle communications in the 60 GHz band". In: *Proc. of IEEE/ACES International Conference on Wireless Communications and Applied Computational Electromagnetics*. 2005.

[96] K. Guan et al. "On Millimeter Wave and THz Mobile Radio Channel for Smart Rail Mobility". In: *IEEE Transactions on Vehicular Technology* 66.7 (2017).

[97] Erich Zöchmann et al. "Better than Rician: Modelling Millimetre Wave Channels as Two-Wave with Diffuse Power". In: *EURASIP Journal on Wireless Communications and Networking* 2019.1-17 (2019).

[98] Erich Zöchmann et al. "Position-Specific Statistics of 60 GHz Vehicular Channels During Overtaking". In: *IEEE Access* 7 (2019).

[99] Erich Zöchmann et al. "Parsimonious Channel Models for Millimeter Wave Railway Communications". In: *Proc. of IEEE Wireless Communications and Networking Conference*. 2019.

[100] Erich Zöchmann et al. "Measured Delay and Doppler Profiles of Overtaking Vehicles at 60 GHz". In: *Proc. of the 12th European Conference on Antennas and Propagation (EuCAP)*. 2018.

[101] Gregory D Durgin, Theodore S Rappaport, and David A De Wolf. "New analytical models and probability density functions for fading in wireless communications". In: *IEEE Transactions on Communications* 50.6 (2002).

[102] James O Berger and William H Jefferys. "The application of robust Bayesian analysis to hypothesis testing and Occam's razor". In: *Journal of the Italian Statistical Society* 1.1 (1992).

[103] Alberto Maydeu-Olivares and C Garcia-Forero. "Goodness-of-fit testing". In: *International encyclopedia of education* 7.1 (2010).

[104] Ulrich G Schuster and Helmut Bolcskei. "Ultrawideband channel modeling on the basis of information-theoretic criteria". In: *IEEE Transactions on Wireless Communications* 6.7 (2007).

[105] Hirotugu Akaike. "A new look at the statistical model identification". In: *IEEE Transactions on Automatic Control* 19.6 (1974).

[106] Thomas M Ludden, Stuart L Beal, and Lewis B Sheiner. "Comparison of the Akaike Information Criterion, the Schwarz criterion and the F test as guides to model selection". In: *Journal of Pharmacokinetics and Biopharmaceutics* 22.5 (1994).

[107] Kenneth P Burnham and David R Anderson. "Multimodel inference: understanding AIC and BIC in model selection". In: *Sociological Methods & Research* 33.2 (2004).

[108] Ruisi He et al. "Vehicle-to-vehicle propagation models with large vehicle obstructions". In: *IEEE Transactions on Intelligent Transportation Systems* 15.5 (2014).

[109] Telmo Santos, Fredrik Tufvesson, and Andreas F Molisch. "Modeling the ultra-wideband outdoor channel: Model specification and validation". In: *IEEE Transactions on Wireless Communications* 9.6 (2010).

[110] Ruisi He et al. "Measurements and analysis of propagation channels in high-speed railway viaducts". In: *IEEE Transactions on Wireless Communications* 12.2 (2013).

[111] Ke Guan et al. "Propagation measurements and modeling of crossing bridges on high-speed railway at 930 MHz". In: *IEEE Transactions on Vehicular Technology* 63.2 (2014).

[112] Ruisi He et al. "Short-term fading behavior in high-speed railway cutting scenario: Measurements, analysis, and statistical models". In: *IEEE Transactions on Antennas and Propagation* 61.4 (2013).

[113] Donggu Kim, Hoojin Lee, and Joonhyuk Kang. "Comments on "Near-Body Shadowing Analysis at 60 GHz"". In: *IEEE Transactions on Antennas and Propagation* 65.6 (2017).

[114] Jesús Lopez-Fernandez et al. "Joint Parameter Estimation for the Two-Wave with Diffuse Power Fading Model". In: *Sensors* 16.7 (2016).

[115] Jesús Lopez-Fernandez et al. "Moment-Based Parameter Estimation for the Two-Wave with Diffuse Power Fading Model". In: *Proc. of the 84th IEEE Vehicular Technology Conference (VTC-Fall)*. 2016.

[116] Arthur Stanley Goldberger. *Econometric Theory*. New York: John Wiley & Sons, 1964.

[117] John H McDonald. *Handbook of biological statistics*. Vol. 2. Baltimore: Sparky House Publishing Baltimore, MD, 2009.

[118] Barnet Woolf. "The log likelihood ratio test (the g-test): Methods and Tables for tests of heterogeneity in contingency tables". In: *Annals of Human Genetics* 21.4 (1957).

[119] Jesse Hoey. "The Two-Way Likelihood Ratio (G) Test and Comparison to Two-Way Chi Squared Test". In: *arXiv preprint arXiv:1206.4881* (2012).

[120] *Pasternack 60 GHz Transmitter and 60 GHz Receiver Modules*. URL: `https://www.pasternack.com/60-ghz-modules-category.aspx`.

[121] Per Zetterberg and Ramin Fardi. "Open source SDR frontend and measurements for 60-GHz wireless experimentation". In: *IEEE Access* 3 (2015).

[122] Thomas Zwick, Troy J Beukema, and Haewoon Nam. "Wideband channel sounder with measurements and model for the 60 GHz indoor radio channel". In: *IEEE Transactions on Vehicular Technology* 54.4 (2005).

[123] Ronald Nissel et al. "Low latency MISO FBMC-OQAM: It works for millimeter waves!" In: *Proc. of IEEE International Microwave Symposium (IMS)*. 2017.

[124] Martin Lerch et al. "The Vienna MIMO testbed: Evaluation of future mobile communications techniques". In: *Intel Technology Journal* 18.3 (2014).

[125] Sebastian Caban et al. "Synchronization of wireless radio testbed measurements". In: *Proc. of IEEE Instrumentation and Measurement Technology Conference (I2MTC)*. 2011.

[126] Markus Laner et al. "Time synchronization performance of desktop computers". In: *Proc. of IEEE Symposium on Precision Clock Synchronization for Measurement Control and Communication (ISPCS)*. 2011.

[127] Seun Sangodoyin et al. "Real-time ultrawideband MIMO channel sounding". In: *Proc. of 6th European Conference on Antennas and Propagation Conference (EUCAP)*. 2012.

[128] Minseok Kim et al. "Development of Low-Cost 60-GHz Millimeter-Wave Channel Sounding System". In: *Proc. of Global Symposium on Millimeter Wave (GSMM)*. 2013.

[129] Erich Zöchmann et al. "Measured Delay and Doppler Profiles of Overtaking Vehicles at 60 GHz". In: *Proc. of the 12th European Conference on Antennas and Propagation (EuCAP)*. 2018.

[130] Martin Lerch et al. "Noise Bounds in Multicarrier mmWave Doppler Measurements". In: *Proc. of European Wireless*. 2017.

[131] Constantine A Balanis. *Antenna theory: analysis and design*. Hoboken: John Wiley & Sons, 2005.

[132] Quentin H Spencer et al. "Modeling the statistical time and angle of arrival characteristics of an indoor multipath channel". In: *IEEE Journal on Selected Areas in Communications* 18.3 (2000).

[133] Gregory D Durgin, Vikas Kukshya, and Theodore S Rappaport. "Wideband measurements of angle and delay dispersion for outdoor and indoor peer-to-peer radio channels at 1920 MHz". In: *IEEE Transactions on Antennas and Propagation* 51.5 (2003).

[134] Andreas F Molisch. *Wireless communications*. Vol. 34. Chichester: John Wiley & Sons, 2012.

[135] Robert Haining. *Spatial data analysis in the social and environmental sciences*. Cambridge: Cambridge University Press, 1993.

[136] Alexander Khintchine. "Korrelationstheorie der stationären stochastischen Prozesse". In: *Mathematische Annalen* 109.1 (1934).

[137] Todd A Ell and Stephen J Sangwine. "Hypercomplex Wiener-Khintchine theorem with application to color image correlation". In: *Proc. of IEEE International Conference on Image Processing*. Vol. 2. 2000.

[138] C Eddie Moxey, Stephen J Sangwine, and Todd A Ell. "Hypercomplex correlation techniques for vector images". In: *IEEE Transactions on Signal Processing* 51.7 (2003).

[139] Stefan Schwarz et al. "Dependable Wireless Connectivity: Insights and Methods for 5G and Beyond". In: *Elektrotechnik und Informationstechnik (e&i)* 135.7 (2018).

[140] Jerry L Hintze and Ray D Nelson. "Violin plots: a box plot-density trace synergism". In: *The American Statistician* 52.2 (1998).

[141] Erich Zöchmann et al. "Statistical Evaluation of Delay and Doppler Spread in 60 GHz Vehicle-to-Vehicle Channels During Overtaking". In: *Proc. of IEEE-APS Topical Conference on Antennas and Propagation in Wireless Communications (APWC)*. 2018.

[142] Erich Zöchmann, Herbert Groll, and Stefan Pratschner. "A Small-Scale Fading Model for Overtaking Vehicles in a Millimeter Wave Communication Link". In: *Proc. of IEEE 20th International Workshop on Signal Processing Advances in Wireless Communications (SPAWC)*. submitted. 2019.

[143] Ram Ramanathan et al. "Ad hoc networking with directional antennas: a complete system solution". In: *IEEE Journal on Selected Areas in Communications* 23.3 (2005).

[144] Elvino S Sousa, Vladan M Jovanovic, and Christian Daigneault. "Delay spread measurements for the digital cellular channel in Toronto". In: *IEEE Transactions on Vehicular Technology* 43.4 (1994).

[145] Franklin F Kuo and James F Kaiser. *System analysis by digital computer*. New York: Wiley, 1966.

[146] Laura Bernadó et al. "Delay and Doppler spreads of nonstationary vehicular channels for safety-relevant scenarios". In: *IEEE Transactions on Vehicular Technology* 63.1 (2014).

[147] D. J. Thomson. "Spectrum estimation and harmonic analysis". In: *Proceedings of the IEEE* 70.9 (1982).

[148] D. Slepian. "Prolate Spheroidal Wave Functions, Fourier Analysis, and Uncertainty-V: The Discrete Case". In: *Bell System Technical Journal* 57.5 (1978).

[149] Erich Zöchmann, Ke Guan, and Markus Rupp. "Two-Ray Models in mmWave Communications". In: *Proc. of IEEE 18th International Workshop on Signal Processing Advances in Wireless Communications (SPAWC)*. 2017.

[150] Erich Zöchmann et al. "Exploring the Physical Layer Frontiers of Cellular Uplink". In: *EURASIP Journal on Wireless Communications and Networking* 2016.1 (2016).

[151] Rodney Vaughan and Jørgen Andersen Bach. *Channels, propagation and antennas for mobile communications*. IET, 2003.

[152] Sebastian Priebe, Martin Jacob, and Thomas Kürner. "The impact of antenna directivities on THz indoor channel characteristics". In: *Proc. of 6th European Conference on Antennas and Propagation (EUCAP)*. 2012.

[153] Thomas Blazek, Erich Zöchmann, and C. F. Mecklenbräuker. "Model Order Selection for LASSO Fitted Millimeter Wave Vehicular Channel Data". In: *Proc. of the IEEE 29th Annual International Symposium on Personal, Indoor, and Mobile Radio Communications (PIMRC)*. 2018.

[154] Thomas Blazek, Erich Zöchmann, and C Mecklenbräuker. "Approximating Clustered Millimeter Wave Vehicular Channels by Sparse Subband Fitting". In: *Proc. of the IEEE 29th Annual International Symposium on Personal, Indoor, and Mobile Radio Communications (PIMRC)*. 2018.

[155] Thomas Blazek, Erich Zöchmann, and Christoph Mecklenbräuker. "Millimeter Wave Vehicular Channel Emulation: A Framework for Balancing Complexity and Accuracy". In: *Sensors* 18.11 (2018).

[156] Christoph F Mecklenbräuker et al. "Vehicular channel characterization and its implications for wireless system design and performance". In: *Proceedings of the IEEE* 99.7 (2011).

[157] Lifeng Wang et al. "Physical Layer Security of Maximal Ratio Combining in Two-Wave With Diffuse Power Fading Channels." In: *IEEE Trans. Information Forensics and Security* 9.2 (2014).

[158] Stefan Schwarz. "Robust full-dimension MIMO transmission based on limited feedback angular-domain CSIT". In: *EURASIP Journal on Wireless Communications and Networking* 2018.1 (2018).

[159] Stefan Pratschner et al. "Versatile mobile communications simulation: the Vienna 5G Link Level Simulator". In: *EURASIP Journal on Wireless Communications and Networking* 2018.1 (2018).

[160] Martin Klaus Müller et al. "Flexible multi-node simulation of cellular mobile communications: the Vienna 5G System Level Simulator". In: *EURASIP Journal on Wireless Communications and Networking* 2018.1 (2018).

[161] Jiho Song et al. "Adaptive millimeter wave beam alignment for dual-polarized MIMO systems". In: *IEEE Transactions on Wireless Communications* 14.11 (2015).

[162] Jaspreet Singh and Sudhir Ramakrishna. "On the feasibility of codebook-based beamforming in millimeter wave systems with multiple antenna arrays". In: *IEEE Transactions on Wireless Communications* 14.5 (2015).

[163] Junho Lee, Gye-Tae Gil, and Yong H Lee. "Channel estimation via orthogonal matching pursuit for hybrid MIMO systems in millimeter wave communications". In: *IEEE Transactions on Communications* 64.6 (2016).

[164] Roi Méndez-Rial et al. "Hybrid MIMO architectures for millimeter wave communications: Phase shifters or switches?" In: *IEEE Access* 4.8 (2016).

[165] Shajahan Kutty and Debarati Sen. "Beamforming for millimeter wave communications: An inclusive survey". In: *IEEE Communications Surveys & Tutorials* 18.2 (2016).

[166] Zhinus Marzi, Dinesh Ramasamy, and Upamanyu Madhow. "Compressive channel estimation and tracking for large arrays in mm-wave picocells". In: *IEEE Journal of Selected Topics in Signal Processing* 10.3 (2016).

[167] Vasanthan Raghavan et al. "Beamforming tradeoffs for initial UE discovery in millimeter-wave MIMO systems". In: *IEEE Journal of Selected Topics in Signal Processing* 10.3 (2016).

[168] Erich Zöchmann et al. "Geometric Tracking of Vehicular mmWave Channels to Enable Machine Learning of Onboard Sensors". In: *Proc. of IEEE Globecom Workshops (GC Wkshps)*. 2018.

[169] Xiaoshen Song, Saeid Haghighatshoar, and Giuseppe Caire. "A scalable and statistically robust beam alignment technique for mm-wave systems". In: *IEEE Transactions on Wireless Communications* 17.7 (2018).

[170] Stefan Schwarz and Erich Zöchmann. "Robust Beam-Alignment for TWDP Fading Millimeter Wave Channels". In: *Proc. of IEEE 20th International Workshop on Signal Processing Advances in Wireless Communications (SPAWC)*. submitted. 2019.

[171] Cen Ling et al. "Double-Directional Dual-Polarimetric Cluster-Based Characterization of 70–77 GHz Indoor Channels". In: *IEEE Transactions on Antennas and Propagation* 66.2 (2018).

Statement on Academic Integrity

I hereby declare and confirm with my signature that the doctoral dissertation is exclusively the result of my own autonomous work, based on my research and literature published, which is seen in the notes and bibliography used. I also declare that no part submitted has been made in an inappropriate way, whether by plagiarizing or infringing on any third person's copyright. Finally, I declare that no part submitted has been plagiarized for any other paper in another higher education institution, research institution or educational institution.

Vienna, March 13, 2019

Author's signature

Advisor's signature

Dipl.-Ing. Erich Zöchmann

Personal data

Citizenship	Austria
Birth date	2. May 1989
Address	Nestroygasse 4/2, A-1020 Wien, Austria
Contact	ezoechma@gmail.com, Tel: +43 664 89 18 537

Education

2015 – **Dr.techn.**, TU Wien, degree anticipated March 2019
On the Occurrence of Two-Wave with Diffuse Power Fading in Millimeter Wave Communications, Adivsor: Prof. Markus Rupp

2013 – 2015 **Dipl.-Ing.** (MSc equivalent), *Telecommunications* at TU Wien
Master thesis, *Generalized LASSO in Array Signal Processing*, Advisors: Prof. C. F. Mecklenbräuker and Prof. P. Gerstoft

2009 – 2013 **BSc**, TU Wien, *Electrical Engineering and Information Technology*

2003 – 2008 **Reife- und Diplomprüfung**, Höhere Technische Lehranstalt Hollabrunn
Technical High School on *Power Engineering and Industrial Electronics*

Languages

German	**native**	*mother tongue*
English	**fluent**	*oral and written*
Swedish	**basic**	*oral and written*
Czech	**basic**	*oral and written*

Experience

Professional

2015 – **University Assistant (Pre-Doc)**, TU Wien
Researcher at the Institute of Telecommunications
Scope: Experimental investigation of millimetre wave wireless communications

2018 – **Research Scientist**, Brno University of Technology
Technical consultation for the millimetre wave setup
Scope: FBMC signal transmission experiments

2017 – 2018 **Visiting Scholar**, The University of Texas at Austin
Short-time (3 months) researcher at the Wireless Networking & Communications Group
Scope: Channel tracking for millimetre wave communications in vehicular scenarios

2013 – 2015 **Project Assistant (Pre-Doc)**, TU Wien
Researcher at the Institute of Telecommunications
Scope: Link-level simulation of LTE-A uplink

Teaching

2016 – **Lecturer**, TU Wien, Institute of Telecommunications
Shared responsibility on *Wireless Communications*

2013 **Tutor**, TU Wien, Institute of Computer Engineering
Tutor of laboratory exercises on *Electrical Engineering*

2010 – 2011 **Tutor**, TU Wien, Institute of Analysis and Scientific Computing
Tutor of exercises on *Preparatory Course Mathematics*

International

2013, 2012 **ATHENS programme** blocked exchange courses:
at Telecom ParisTech on "Quantum entanglement for communications: from theory to experiments"
at IST Lisbon on "Elab - Remotely controlled physics laboratories"

2012 **Erasmus Semester**, Chalmers University of Technology, Sweden

Internships and Military Service

2013 **Omicron Electronics**, 6833 Klaus, summer intern
Scope: Verification of VHDL code and development of a signal analyser

2010 **Egston Gmbh**, 3730 Eggenburg, summer intern
Scope: Testing of switched-mode power supplies

2008 – 2009 **Military Service**, Guards Music - representative band of the Austrian Armed Forces, Vienna

Awards and Scholarships

2016 Award for the scientific quality of the Master thesis by the Ernst Blickle foundation.

2010 – 2013 Scholarship of the Faculty of Electrical Engineering for outstanding students.

2010 – 2013 Scholarship of the University's foundation (Stiftungsstipendium)

2010 – 2013 Scholarship of the Johann Wilhelm Ritter von Mannagetta foundation.

2008, 2006 Löffler-Müller scholarship for outstanding pupils

List of Publications

Journals

Zöchmann, E.; et al. "Position-Specific Statistics of 60 GHz Vehicular Channels During Overtaking" in IEEE Access, vol. 7, 2019

Zöchmann, E.; et al. "Better than Rician: Modelling millimetre wave channels as Two-Wave with Diffuse Power" in EURASIP Journal on Wireless Communications and Networking, Springer Nature, vol. 2019, no. 21, 2019

Caban, S.; Lerch, M.; Pratschner, S.; **Zöchmann, E.**; et al. "Design of Experiments to Compare Base Station Antenna Configurations" , in IEEE Transactions on Instrumentation and Measurement, to appear, 2019

Blazek, T.; **Zöchmann, E.**; Mecklenbräuker, C.F., "Millimeter Wave Vehicular Channel Emulation: A Framework for Balancing Complexity and Accuracy," in Sensors, MDPI, vol. 18, 2018

Schwarz, S.; Ramos Elbal, B.; **Zöchmann, E.**; et al. "Dependable Wireless Connectivity: Insights and Methods for 5G and Beyond," in Elektrotechnik und Informationstechnik (e&i), Springer, vol. 135, no. 7, 2018

Mecklenbräuker, C.F.; Gerstoft, P.; **Zöchmann, E.** "Generalized c–LASSO and its Dual for Sparse Signal Estimation from Array Data," in Elsevier Signal Processing, vol. 130, 2017

Zöchmann, E.; et al. "Exploring the Physical Layer Frontiers of Cellular Uplink-The Vienna LTE-A Uplink Simulator," in EURASIP Journal on Wireless Communications and Networking, Springer, vol. 2016, no. 118, 2016

Letters

Zöchmann, E.; et al. "Carbon Fiber Reinforced Polymer with Isotropic 60 GHz Reflectivity" in Progress In Electromagnetics Research M, vol. 67, 2018

Artner, M.; **Zöchmann, E.**; et al. "Angle-dependent reflectivity of twill-weave carbon fibre reinforced polymer for millimetre waves" in Electronics Letters, 2018

Pratschner, S.; **Zöchmann, E.**; Rupp, M., "Low Complexity Estimation of Frequency Selective Channels for the LTE-A Uplink," in IEEE Wireless Communications Letters, vol.4, no.6, 2015

Conferences

more than 20 papers at peer-reviewed international conferences

Book Chapters

Pratschner, S.; **Zöchmann, E.**, "LTE-Advanced Uplink Transmissions" in The Vienna LTE-Advanced Simulators: Up and Downlink, Link and System Level Simulation, Springer Singapore, 2016